University of Alberta

True Amplitude Processing in VSPs

by

Michael Grech ©

A thesis submitted to the Faculty of Graduate Studies and Research in partial fulfillment of the requirements for the degree of **Master of Science**.

in

Geophysics

Department of Physics

Edmonton, Alberta
Fall 1998

National Library of Canada
Acquisitions and Bibliographic Services
395 Wellington Street
Ottawa ON K1A 0N4
Canada

Bibliothèque nationale du Canada
Acquisitions et services bibliographiques
395, rue Wellington
Ottawa ON K1A 0N4
Canada

Your file Votre référence

Our file Notre référence

The author has granted a non-exclusive licence allowing the National Library of Canada to reproduce, loan, distribute or sell copies of this thesis in microform, paper or electronic formats.

The author retains ownership of the copyright in this thesis. Neither the thesis nor substantial extracts from it may be printed or otherwise reproduced without the author's permission.

L'auteur a accordé une licence non exclusive permettant à la Bibliothèque nationale du Canada de reproduire, prêter, distribuer ou vendre des copies de cette thèse sous la forme de microfiche/film, de reproduction sur papier ou sur format électronique.

L'auteur conserve la propriété du droit d'auteur qui protège cette thèse. Ni la thèse ni des extraits substantiels de celle-ci ne doivent être imprimés ou autrement reproduits sans son autorisation.

0-612-34368-5

Canada

University of Alberta

Library Release Form

Name of Author: Michael Grech

Title of Thesis: True Amplitude Processing in VSPs

Degree: Master of Science

Year this Degree Granted: 1998

Permission is hereby granted to the University of Alberta Library to reproduce single copies of this thesis and to lend or sell such copies for private, scholarly or scientific research purposes only.

The author reserves all other publication and other rights in association with the copyright in the thesis, and except as hereinbefore provided, neither the thesis nor any substantial portion thereof may be printed or otherwise reproduced in any material form whatever without the author's prior written permission.

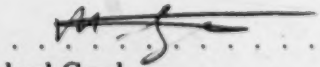

Michael Grech
306 S. 3520 - 31 St N.W
CALGARY T2L 2A4

Date: 18/9/98

University of Alberta

Faculty of Graduate Studies and Research

The undersigned certify that they have read, and recommend to the Faculty of Graduate Studies and Research for acceptance, a thesis entitled **True Amplitude Processing in VSPs** submitted by Michael Grech in partial fulfillment of the requirements for the degree of **Master of Science** in *Geophysics*.

Dr. D.R. Schmitt (Supervisor)

Dr. T.J.T Spanos

Dr. M Freeman

Dr. R.J. Chalaturnyk

Date: 11/9/98

Abstract

The amplitudes of reflected seismic waves contain substantial petrophysical information on changes in the properties of materials in the earth. To extract this information correct amplitude processing is required, especially in the analysis of the variation of reflection strength with angle of incidence as measured in well bore seismic experiments. However, current VSP amplitude gain techniques involve T^n scaling down the trace. This practice originates in the need to improve the visibility of weaker events diminished by geometrical spreading of a wavefront. This method is crude and does not properly take into account for geometry and geology in amplitude decay. As an alternative we propose a model based amplitude correction. Amplitude correction curves are derived on the basis of ray tracing through a reasonable geologic model; the resulting correction curves can then be applied to the VSP data to restore the amplitudes. Tests on synthetic VSP arrival curves demonstrate the superiority over the empirical based correction. Six different amplitude attributes are calculated for the down-going primary wavelet of a shallow zero offset VSP and the application of the method to this data set is attempted.

Contents

1 Introduction 3

2 Theoretical Background 6
- 2.1 The wave equation . . . 6
  - 2.1.1 What is Seismic Amplitude ? . . . 9
- 2.2 Factors influencing seismic amplitudes . . . 10
  - 2.2.1 Geometrical effects . . . 10
  - 2.2.2 Geometrical effects for an arbitrary vertically inhomogeneous medium . . . 13
  - 2.2.3 The Gel'chinsky method . . . 15
  - 2.2.4 Transmission effects . . . 17
  - 2.2.5 Energy flux . . . 19
  - 2.2.6 Attenuation . . . 21
  - 2.2.7 Directivity Effects . . . 22

3 A model based amplitude correction 26
- 3.1 The VSP . . . 26
  - 3.1.1 Introduction . . . 26
  - 3.1.2 VSP setups . . . 28
  - 3.1.3 The ray tracing program . . . 28
  - 3.1.4 Illustrative examples . . . 30
- 3.2 Amplitude restoration . . . 41
  - 3.2.1 VSP processing . . . 41
  - 3.2.2 The multiplicative model of seismic amplitudes . . . 46
  - 3.2.3 Traditional amplitude restoration curves . . . 47
  - 3.2.4 The Acoustic Impedance Effect . . . 49
- 3.3 Summary . . . 56

4 Amplitude correction of a real data set 57
- 4.1 Data Characteristics . . . 57
  - 4.1.1 Geological Background . . . 57
  - 4.1.2 Acquisition Parameters . . . 59
- 4.2 Restoring the Primary Amplitude . . . 63
  - 4.2.1 Generating the model . . . 63
  - 4.2.2 Calculating the correction curves . . . 64

4.2.3 The direct arrival amplitude 67
4.2.4 Applying the correction curves 70
4.3 Summary 77

5 Conclusions **79**

A Model for the UTF site **87**

B The Ray Tracing Program **89**
B.1 MASTER.M 89
B.2 DGRM.M 93
B.3 PRIM.M 94
B.4 REFLECT.M 97

List of Figures

2.1 Small parallelpiped in a continuum. Stress components acting on the front face do not balance those on the back face. 7

2.2 The ray coordinates $[\alpha_1, \alpha_2, t_p]$ and their relation to the geometric quantities in the vicinity of P on the ray and wavefront τ at time $t = \tau_p$. [29] 11

2.3 Part of the ray tube between two wavefronts τ_o and τ located at a distance Δs apart. The corresponding cross-sections of the ray tube are denoted by $d\sigma(\tau_o)$ and $d\sigma(\tau)$ respectively. The coordinate lines due to two angular coordinates α_1 and α_2 are also shown on the wavefront τ_o [29]. 12

2.4 Evaluation of the discontinuity in geometrical spreading across the boundary during the transmission of the ray. [29] 14

2.5 Notation for the sixteen possible reflection and transmision coefficients arising from problems of P-SV waves at the welded interface between two different solid half-spaces. [30] 19

2.6 Energy Reflection Coefficients vs Angle of incidence for an incident P wave. α_2 / $\alpha_1 = 0.5$, ρ_2 / ρ_1 =0.8 and $\sigma_1 = 0.3, \sigma_2 = 0.25$. 21

2.7 Geometry for calculation of amplitude as a function of the vertical angle θ for a source below a free surface (From [32]). 23

2.8 Directivity patterns of a monochromatic P wave point source below a free surface for different ratios of h/λ. From [32]. 24

2.9 Directivity functions for a disk vibrating in a direction perpendicular to the ground surface for different values of Poisson's ratio Υ. The dashed line is just a reference line for comparison purposes. u_R denotes the P wave and u_θ denotes the S wave. From [33]. 25

3.1 Field setup for an offset VSP. Several geophones in a borehole measure waves generated by a surface source. 27
3.2 Field setup for a walkaway VSP 27
3.3 Ray diagram for a layer over halfspace and a source at 300m offset for illustrative Model 1 32
3.4 Ray diagram for a layer over halfspace and a source at 600m offset for illustrative Model 1 32
3.5 VSP plot for geometry in Figure 3.3. Increasing receiver number corresponds to increasing depth. Receivers from 800m to 320m at 20m depth increments. 33
3.6 VSP plot for geometry in Figure 3.4. Increasing receiver number corresponds to increasing depth. Receivers from 800m to 320m at 20m depth increments. 33
3.7 Ray diagram for slow model described in Table 3.3. Source offset 300m. 36
3.8 Ray diagram for fast model described in Table 3.4. Source offset 300m. 36
3.9 VSP plot for geometry in Figure 3.7 37
3.10 VSP plot for geometry in Figure 3.8 37
3.11 Ray diagram for model described in Table 3.5 39
3.12 VSP plot for geometry in Figure 3.11 40
3.13 A real VSP plot including multiples, converted energy and noise. . . . 41
3.14 Cartoon showing rays constituting the upgoing and downgoing wavefields. Rays marked by a U form the upgoing wavefield and the rays marked by a D form the downgoing wavefield 42
3.15 Downgoing wavefield for illustrative model 4 (Table 3.5). 43
3.16 Upgoing wavefield for illustrative model 4 (Table 3.5). 43
3.17 Cartoon showing multiples in the upgoing wavefield and their relationship with the downgoing multiples. 45
3.18 Ray diagram for zero offset reflections from interface No. 8 as defined in Table 3.5. 50
3.19 Observed particle velocity amplitudes for the upward travelling reflection from the 3000 m deep interface of Table 3.5. The source offset is 30 m. 50

3.20 Geometrical spreading effects for the reflection from the interface at 3000 m as given in Table 3.5. The source offset is 30 m. 51
3.21 Cumulative transmission loss effects for a reflection from the interface at 3000 m as given in Table 3.5. This also retains the amplitude versus angle of incidence variations (AVA effect) and the acoustic impedance effect. The source offset is 30 m. 51
3.22 Expected amplitude due to anlge of incidence variations only from the interface at 3000 m for an offset of 30 m. 52
3.23 Observed particle velocity amplitudes from Figure 3.19 after application of the conventional 'empirical' t^n correction to each trace with n = 1.7 52
3.24 Observed particle velocity amplitudes from Figure 3.19 after application of a conventional t^n correction down each trace with n = 0.6. . . 53
3.25 Observed particle velocity amplitudes for the upward travelling reflection from the 3000m deep interface of Table 3.5. The source offset is 1500m. 53
3.26 Geometrical spreading effects for the reflection from the interface at 3000m as given in Table 3.5. The source offset is 1500m. 54
3.27 Cumulative transmission loss effects for a reflection from the interface at 3000m as given in Table 3.5. This also includes the AVA effect and the acoustic impedance effect. The source offset is 1500m. 54
3.28 Observed particle velocity amplitudes from Figure 3.25 after application of a conventional t^n correction down each trace for n=0.6. 55
3.29 Expected amplitude of reflection from the interface at 3000m for a source offset of 1500m. 55

4.1 Location of the Underground Test Facility (From Chalturnyk [53]). . 58
4.2 Stratigraphy at the UTF site (From Chalturnyk [53]). 58
4.3 Sonic Log for the observation well. The thin line represents the complete log whereas the thick line is a blocked version of the complete log. 60
4.4 Raw data set. Colorbar denotes amplitude. 61

4.5 Wiggle plot or raw data set after the application of AGC (Automatic Gain Control) to boost later energy 62
4.6 Blocked compressional, shear and density logs corresponding to the model in Table A.1 65
4.7 Transit times from the surfaec for the downgoing primary energy as determined for the synthetics as they compared to the picked times from the real data. Note that the transit time curves are nearly identical for both the complete and blocked log models. 66
4.8 Geometrical effect amplitude decay relative to amplitude at 30m as obtained by ray tracing through the models. Green curve corresponds to blocked log, blue curve corresponds to complete sonic log (10 cm). 68
4.9 Transmission effect coefficients as obtained by ray tracing through the model. Green curve corresponds to blocked log, blue curve corresponds to complete log. 68
4.10 Amplitude for the downgoing primary energy as determined by ray-tracing through the models. Red curve shows the amplitude as picked from the real data. 69
4.11 Amplitude attributes against receiver number. 71
4.12 Amplitude attributes against receiver number on a semilog graph. . . 72
4.13 First order amplitude change on the vertical component due to variation in the geometry between the source and receivers on increasing depth. 73
4.14 Amplitude attributes against geophone depth on a semilog graph after correcting for source directivity. Hardly any difference can be observed from Figure 4.12. 74
4.15 Amplitude attributes after applying model based amplitude correction. 76
4.16 Amplitude attributes from Figure 4.15 after appyling a moving average filter. 76
4.17 Relative amplitude loss for different values of Q for a frequency of 45Hz. 77

List of Tables

3.1 Input and output parameters for MASTER.M 29

3.2 Illustrative Model 1 - Layer over half space 30

3.3 Illustrative model 2 - Thick fast layer in halfspace 34

3.4 Illustrative model 3 - Thick slow layer in halfspace 34

3.5 Illustrative model 4 - Multilayer model 38

A.1 Geological Model for UTF site 88

Acknowledgements

To my supervisor, Dr. Doug Schmitt, I express my thanks for his guidance and assistance during this work.

I would like to show my appreciation towards Schlumberger of Canada for providing me with the opportunity and financial support for doing this work. My gratitude goes towards Mike Jones for suggesting the project and for the many constructive discussions.

I would like to thank my colleagues Jo and Rog for making my stay in 613 a happy one.

My family and friends for their support.

Last but not least I would like to thank Dr. Franta Hron for granting me permission to reproduce some of his figures.

'The True Theory of Elasticity or Springiness' (1676)

CEIINOSSITTUV.

[Anagram of UT TENSIO, SIC VIS - as the extension, so the force. This was one of the ways of establishing priority in a discovery.]

Robert Hooke 1635 - 1703

Chapter 1

Introduction

Seismic reflection profiling is the principle method used in the exploration for hydrocarbons. Aside from traveltime information, seismic reflection data also contains substantial petrophysical information in the amplitudes of the reflected events. One way to extract this information is to observe the variation in strength of a given reflection with angle of incidence. In industrial surface reflection studies, such analysis is referred to as "Amplitude Versus Offset" or AVO. This nomenclature recognizes that the angle of incidence of a wave reflected from an interface at depth increases as the source to receiver 'offset' distance increases. A considerable literature now exists as regards the application of this method in conventional seismic surface profiling. Ostrander [1] [2], Gassaway [4], Chiburis [3], Coulombe [5] also discuss the importance of proper amplitude restoration needed for AVO analysis. Despite this importance the problem of correct amplitude restoration, i.e. that of removing variations due to seismic source variability and directionality, geometrical divergence, attenuation, and energy loss on transmission, has not been as carefully examined as required. Indeed, most AVO analyses are done in a rather ad hoc fashion and although they may reveal some variation of reflected amplitudes, much of the interpretive potential of the technique is lost. The situation is ever worse for well bore seismic studies which are complicated by an asymmetry of upward and downward ray segments.

Extracting this information from recorded amplitudes is not an easy task. The amplitudes of reflected events arriving at the geophone are influenced by various factors as discussed by O'Doherty and Anstey [6] and Allen and Peddy [7]. These factors modulate the reflectivity of an interface and include variations in the seismic source

strength and directivity, multiples, geophone coupling, attenuation and transmission losses, scattered energy, wavefield divergence and noise. In order to be able to extract the relevant geological information, the contribution to the amplitude arising only from the reflectivity of an acoustic boundary must be isolated.

Yu [8], Dey-Sakar [9] and Lee [10] describe the importance of correct amplitude processing in AVO analysis on surface seismic data. Current amplitude restoration techniques are varied and can be grouped into noise filtering techniques and amplitude compensation techniques. In the former, unwanted energy such as multiples, incoherent and coherent noise is removed with familiar seismic processing techniques such as stacking, deconvolution, F-K filtering, and band pass filtering. Amplitude compensation techniques attempt to restore amplitude that is modified through geometrical spreading, transmission, attenuation and diffraction.

Seismic energy sources may usually be thought of as point sources. For the simplest case of a homogeneous isotropic medium, a point source generates a spherical wavefront. The input energy spreads over an increasing wavefront area as the wave propagates. Particularly in shorter offsets, these geometrical spreading effects play a major role causing rapid amplitude loss down the trace. Compensating for this amplitude decay thus becomes a very important step in data processing and various approaches have been proposed. Newman [11] applied ray theory to derive an expression for amplitude correction in an environment consisting of horizontal isotropic layers. Fazzari [12] showed that Newman's correction over amplifies reflections from dipping beds at late times and developed a post stack dip-dependent divergence correction as a solution. Two years later, Arnsten and Sollid [13] showed how this dip-dependent correction can be included as part of prestack migration or inversion. Wang and Cowan [14] suggested the use of slant stacks and Schleicher et. al [15] used a dual diffraction stack.

The transmission of energy across boundaries is another factor influencing amplitude. Each time a traveling wavefront encounters the boundary in the acoustic properties part of the energy is transmitted across the boundary and part is reflected. Moreover, whenever the impinging wavefront is at an oblique angle of incidence conversion between transverse and shear modes of vibration can occur. The energy partitioning and mode conversion depends on the change in acoustic properties across

the boundary, the mode of vibration of the incident wave and the incidence angle. The theory for the transmission and reflection of plane elastic waves in homogeneous isotropic media was described by Zoeppritz in 1919. Tooley and Sagoci [16] worked out several numerical examples for different acoustic boundaries. De la Cruz and Spanos [17, 18] developed a complete theory to describe motion in porous media and some numerical examples were given in [19].

The net effect of transmission through boundaries is that less energy is successively available for reflection from deeper interfaces. This effect is increased for larger changes in the elastic material properties and intensified by the number of interfaces. Harlan [20] uses tomographic methods to correct for such transmission anomalies and Gonzales and Chambers [21] deal with lateral lithologic variations in the overburden.

Furthermore, the interference of multiple reflections with the directly arriving energy complicates the problem. Interbed multiples generated by cyclic layers can have the effect of a transmission filter as described by O'Doherty and Anstey [6] and Shapiro and Zien [22], discriminating against energy of higher frequency. These effects can be a considerable obstacle to amplitude studies as illustrated by Schoenberger and Levin [23] with synthetic seismograms, by De Souza [24] for the Brazilian Parana basin layered basalt stack and by Coulombe and Bird [26] for a layered coal stack.

The objective of this work is to study amplitude loss in well bore seismic experiments referred to in the geophysical literature as vertical seismic profiles (VSP). In the daily processing of VSPs amplitude restoration is achieved through an empirical correction in which the applied gain is proportional to an exponent of time. This crude method ignores completely any geological and geometrical effects. Even though a pleasing structural image of the geology is achieved, the amplitudes so corrected may fail to provide correct information for stratigraphic studies. In Chapter 2 an outline of the theoretical background of the seismic method and amplitude loss mechanisms is given. Chapter 3 develops the idea of a model based amplitude correction and provides a progression of several illustrations on synthetic data sets. Then in Chapter 4 the method is applied to the downgoing energy in a VSP to investigate its feasibility and the limitations.

Chapter 2

Theoretical Background

2.1 The wave equation

Seismic energy introduced into the ground will propagate in the form of a wave. Consider a small parallelpiped in a continuum with sides $\partial x, \partial y, \partial z$ (Figure 2.1).

Assume that the stresses on opposite faces are not balanced. Then following the derivation of Fowler [25], if the stresses on the rear face are $-\sigma_{xx}, -\sigma_{xy}, -\sigma_{xz}$, the stresses on the front shaded face are given by

$$\sigma_{xx} + \delta\sigma_{xx}, \sigma_{xy} + \delta\sigma_{xy}, \sigma_{xz} + \delta\sigma_{xz}$$

The additional stresses $(\delta\sigma_{xx}, \delta\sigma_{xy}, \delta\sigma_{xz})$ can be written as :

$$\frac{\partial\sigma_{xx}}{\partial x}\delta x, \frac{\partial\sigma_{xy}}{\partial x}\delta x, \frac{\partial\sigma_{xz}}{\partial x}\delta x \tag{2.1}$$

Thus, the net force acting on the two faces perpendicular to the x axis is:

$$\begin{aligned}(-\sigma_{xx} + \sigma_{xx} + \frac{\partial\sigma_{xx}}{\delta x}\delta x, -\sigma_{xy} + \sigma_{xy} + \frac{\partial\sigma_{xy}}{\partial x}\delta x,\\ -\sigma_{xz} + \sigma_{xz} + \frac{\partial\sigma_{xz}}{\partial x}\delta x)\delta y\delta z = \left(\frac{\partial\sigma_{xx}}{\partial x}, \frac{\partial\sigma_{xy}}{\partial x}, \frac{\partial\sigma_{xz}}{\partial x}\right)\delta x\delta y\delta z\end{aligned} \tag{2.2}$$

Similar expressions can be obtained for the other two pairs of faces. It follows that the net force acting on the parallelpiped in the x direction is given by:

$$\left(\frac{\partial\sigma_{xx}}{\partial x} + \frac{\partial\sigma_{xy}}{\partial y} + \frac{\partial\sigma_{xz}}{\partial z}\right)\delta x\delta y\delta z \tag{2.3}$$

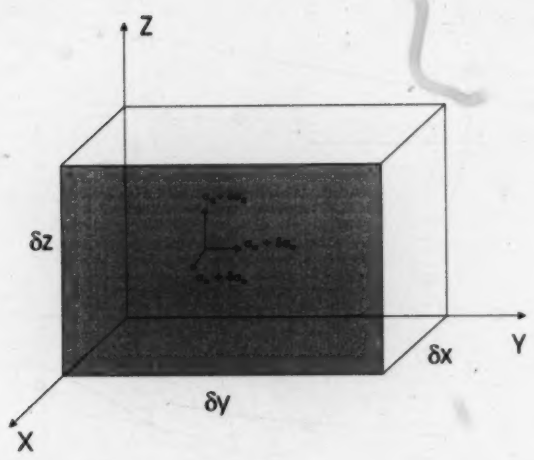

Figure 2.1: Small parallelpiped in a continuum. Stress components acting on the front face do not balance those on the back face.

Similar expressions can be obtained for the net forces in the x and y directions respectively. From Newton's second law of motion, we get

$$\left(\frac{\partial \sigma_{xx}}{\partial x} + \frac{\partial \sigma_{xy}}{\partial y} + \frac{\partial \sigma_{xz}}{\partial z}\right) \delta x \delta y \delta z = \rho \delta x \delta y \delta z \frac{\partial^2 u}{\partial t^2} \tag{2.4}$$

where ρ is the density of the parallelpiped and u is the x component of the displacement. Now from the expressions relating stress to strain we get:

$$\rho \frac{\partial^2 u}{\partial t^2} = \frac{\partial}{\partial x}(\lambda \Delta + 2\mu e_{xx}) + \frac{\partial}{\partial y}(2\mu e_{xy}) + \frac{\partial}{\partial z}(2\mu e_{xz}) \tag{2.5}$$

where λ and μ are Lamè 's elastic constants, Δ is the fractional increase in volume caused by a deformation and e_{ij} denotes the strain components. By expressing the strain components in terms of displacement, we get :

$$\rho \frac{\partial^2 u}{\partial t^2} = \frac{\partial}{\partial x}\left(\lambda \Delta + 2\mu \frac{\partial u}{\partial x}\right) + \frac{\partial}{\partial y}\left(\mu\left(\frac{\partial v}{\partial x} + \frac{\partial u}{\partial y}\right)\right) + \frac{\partial}{\partial z}\left(\mu\left(\frac{\partial w}{\partial x} + \frac{\partial u}{\partial z}\right)\right) \tag{2.6}$$

Assuming λ and μ to be constants we can write :

$$\rho \frac{\partial^2 u}{\partial t^2} = \lambda \frac{\partial \Delta}{\partial x} + \mu \frac{\partial \Delta}{\partial x} + \mu(\nabla^2 u) \tag{2.7}$$

Similarly from the y and z components of the forces we get equations for v and w:

$$\rho\frac{\partial^2 v}{\sigma t^2} = (\lambda+\mu)\frac{\partial \Delta}{\partial y} + \mu(\nabla^2 v) \tag{2.8}$$

$$\rho\frac{\partial^2 w}{\sigma t^2} = (\lambda+\mu)\frac{\partial \Delta}{\partial z} + \mu(\nabla^2 w) \tag{2.9}$$

These three equations are the equations of motion for a general disturbance transmitted through a homogeneous, isotropic, perfectly elastic medium, assuming infinitesimal strain and no body forces. If we differentiate these equations with respect to x, y and z respectively and add up the results, we get

$$\rho\frac{\partial^2 \Delta}{\partial t^2} = (\lambda+2\mu)\nabla^2\Delta \tag{2.10}$$

This is the wave equation for a dilational disturbance traveling with speed

$$\alpha = \sqrt{\frac{\lambda+2\mu}{\rho}} \tag{2.11}$$

On the other hand, differentiating Eqn. 2.7 with respect to y and Eqn. 2.8 with respect to x we get:

$$\rho\frac{\partial^2}{\partial t^2}\left(\frac{\partial u}{\partial y}\right) = (\lambda+\mu)\frac{\partial^2 \Delta}{\partial x \partial y} + \mu\nabla^2\left(\frac{\partial u}{\partial y}\right) \tag{2.12}$$

and

$$\rho\frac{\partial^2}{\partial t^2}\left(\frac{\partial v}{\partial x}\right) = (\lambda+\mu)\frac{\partial^2 \Delta}{\partial x \partial y} + \mu\nabla^2\left(\frac{\partial v}{\partial x}\right) \tag{2.13}$$

Subtracting Eqn. 2.13 from 2.12 gives

$$\rho\frac{\partial^2}{\partial t^2}\left(\frac{\partial u}{\partial y} - \frac{\partial v}{\partial x}\right) = \mu\nabla^2\left(\frac{\partial u}{\partial y} - \frac{\partial v}{\partial x}\right) \tag{2.14}$$

By differentiating and subtracting derivatives, the two other equations can be obtained :

$$\rho\frac{\partial^2}{\partial t^2}\left(\frac{\partial u}{\partial z} - \frac{\partial w}{\partial x}\right) = \mu\nabla^2\left(\frac{\partial u}{\partial z} - \frac{\partial w}{\partial x}\right) \tag{2.15}$$

$$\rho\frac{\partial^2}{\partial t^2}\left(\frac{\partial v}{\partial z} - \frac{\partial w}{\partial y}\right) = \mu\nabla^2\left(\frac{\partial v}{\partial z} - \frac{\partial w}{\partial y}\right) \tag{2.16}$$

However, since $\left(\frac{\partial u}{\partial y} - \frac{\partial v}{\partial x}\right)$ and so on are the components of Curl **u**, these three equations can be written as

$$\rho \frac{\partial^2}{\partial t^2}(Curl\mathbf{u}) = \mu \nabla^2(\text{Curl}\mathbf{u}) \tag{2.17}$$

which is a vector wave equation for a rotational disturbance transmitted through the material at speed

$$\beta = \sqrt{\frac{\mu}{\rho}} \tag{2.18}$$

Equations 2.10 and 2.17 have solutions of the form $y(x,t) = F(x \pm ct)$ where c is the speed of propagation of the wave as given by 2.11 and 2.18 respectively. From [28], all plane waves in an isotropic elastic solid propagate with one or the other of the two speeds as given by Equations 2.11 or 2.18.

2.1.1 What is Seismic Amplitude ?

From the basic definitions of physics, work or energy is the product of force and distance where force is in the direction of displacement, and power is the rate of doing work. Following Clay [34], for a continuous medium we use the energy passing through a surface normal to the direction of propagation of the propagating waves. Since in a continuous medium, force per unit area is pressure, the power per unit area is given by

$$J = pv$$

where v is the particle velocity and p is the pressure of the wave.

From Equation 2.4, for the x direction we get

$$\frac{\partial \sigma_{xx}}{\partial x} = \rho \frac{\partial^2 u}{\partial t^2} \tag{2.19}$$

and if v_x is the particle velocity in the x direction, we get

$$\frac{\partial \sigma_{xx}}{\partial x} = \rho \frac{\partial v_x}{\partial t} \tag{2.20}$$

Now consider the solution for the waves traveling in the positive x direction. From the previous section, these are of the form $y(x,t) = y(t - x/c)$. Then if $\tau = t - x/c$ by taking partial derivatives Equation 2.20 can be written as

$$-\frac{1}{c}\frac{\partial \sigma_{xx}}{\partial \tau} = \rho \frac{\partial v_x}{\partial \tau} \tag{2.21}$$

for waves traveling in the -x direction. Integrating on both sides, for wave traveling in the $\pm x$ direction,

$$\sigma_{xx} = \pm \rho c v_x.$$

Hence in general, since $J = pv$, then

$$J = \rho c v^2$$

where $\rho c = I$ which is the acoustic impedance of the medium. Hereafter, the particle velocity v will be taken as the amplitude in such a way that

$$J = IA^2 \tag{2.22}$$

where A denotes amplitude. This is important as the geophone is sensitive to particle velocity.

2.2 Factors influencing seismic amplitudes

2.2.1 Geometrical effects

Consider a point source of elastic waves in a homogeneous elastic medium. The wavefronts will be spherical and concentric about the source. Assume that the total wave field can be decomposed into an infinite number of contributions each of which can be attributed to a single ray. After Hron [29], the position of any point P on a given ray can be uniquely specified using a system of ray coordinates as illustrated in Figure 2.2.

Hence $P = [\alpha_1, \alpha_2, \tau_p]$ where

$\left.\begin{array}{ll} \alpha_1 & \text{(longitude)} \\ \alpha_2 & \text{(latitude)} \end{array}\right\}$ are the taking off angles of the ray at the source

τ_p is the arrival time at P taken as a parameter on the ray

Define the ray tube as a narrow pencil of rays radiated from the source into a small body angle $d\Omega = cos\alpha_2 d\alpha_1 d\alpha_2$ centered about the central ray whose taking off angles are α_1 and α_2. The body angle $d\Omega$ is that part of the subsurface of the sphere

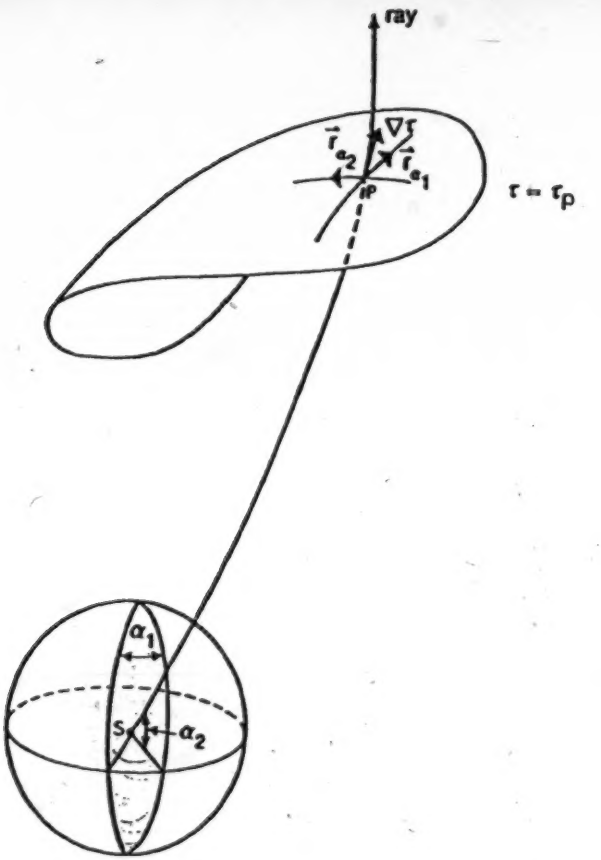

Figure 2.2: The ray coordinates $[\alpha_1, \alpha_2, t_p]$ and their relation to the geometric quantities in the vicinity of P on the ray and wavefront τ at time $t = \tau_p$. [28]

sufficiently small values of $d\alpha_1$ and $d\alpha_2$ the solid angle $d\Omega$ is equal to the crossection $d\sigma$ at a unit distance $s = \mid \vec{r} \mid = 1$ from the source. As the energy of wave propagation in any isotropic medium is carried by the wave along the ray paths, there is no energy escaping through the walls of the elementary tube. Therefore, provided the medium is perfectly elastic, the energy flux dE/dt through any cross-section $d\sigma$ of the ray tube remains constant.

Denoting ΔE as the energy transferred across the cross-section $\Delta\sigma$ in time δt, c as the wave speed and ϵ as the volume density of energy due to the wave motion , we have

$$\Delta E = \epsilon c \Delta\sigma \Delta t,$$

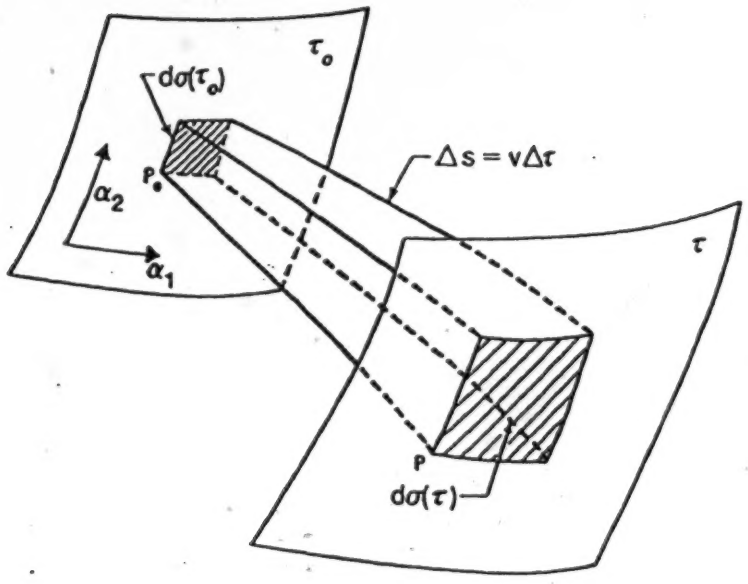

Figure 2.3: Part of the ray tube between two wavefronts τ_o and τ located at a distance Δs apart. The corresponding cross-sections of the ray tube are denoted by $d\sigma(\tau_o)$ and $d\sigma(\tau)$ respectively. The coordinate lines due to two angular coordinates α_1 and α_2 are also shown on the wavefront τ_o [28].

or

$$\frac{dE}{dt} = \varepsilon c \Delta\sigma.$$

The volume energy density ε is equal to the total mechanical energy of a unit volume of mass $\Delta m = \rho$ undergoing the wave motion. Consider a harmonic motion of the form

$$U(t, s_o) = A sin(k s_o - \omega t)$$

of frequency ν and where A is the amplitude of the displacement due to the wave particle motion at a fixed location on the ray at distance s_o from the source. Then the volume energy density ε is given by

$$\varepsilon = K_{max} = \frac{1}{2}\rho \left|\frac{\partial U}{\partial t}\right|^2_{max} = \frac{1}{2}\rho(2\pi\nu A)^2 \qquad (2.23)$$

By conservation of energy flux(equal to the power input from the source into the ray tube) we get

$$\frac{1}{2}4\pi^2\nu^2\rho c\Delta\sigma A^2|_{t=\tau_o} = \frac{1}{2}4\pi^2\nu^2\rho c\Delta\sigma A^2|_{t=\tau}$$

or

$$A(\tau) = \sqrt{\frac{\rho(\tau_o)v(\tau_o)}{\rho(\tau)v(\tau)}}\,\frac{A(\tau_o)}{\sqrt{\frac{\Delta\sigma(\tau)}{\Delta\sigma(\tau_o)}}} \tag{2.24}$$

Here two different values of the arrival time $\tau_o = \tau(s_o)$ and $\tau_o = \tau(s)$ are used to specify the locations of two points P_o and P on the ray at the distances s_o and s from the source, respectively.

The quantity

$$L = \sqrt{\frac{\Delta\sigma(\tau)}{\Delta\sigma(\tau_o)}}$$

is known as the geometrical spreading or divergence of the ray tube between points P_o and P on the ray. L depends on the distance between P and P_o. For a point source radiating a spherical wave, we have $\Delta\sigma(\tau) = r^2 d\Omega$, $\Delta\sigma(\tau_o) = {r_o}^2 d\Omega$ where $r = \nu\tau$ and $r_o = \nu\tau_o$ are the radii of curvature of the wavefronts passing through P and P_o respectively with $d\Omega$ being the solid angle due to the ray tube. Then the geometrical spreading between P_o and P becomes

$$L = \sqrt{\frac{r^2 d\Omega}{{r_o}^2 d\Omega}} = \frac{r}{r_o} = \frac{\tau}{\tau_o} \tag{2.25}$$

In such a manner the geometric spreading of the ray tube is related to the arrival time τ.

2.2.2 Geometrical effects for an arbitrary vertically inhomogeneous medium

Whenever the ray encounters a discontinuity such as an interface between two layers with different acoustic impedances, the ray tube will also experience a discontinuity and this will manifest itself in the computation of the geometrical spreading. Following the derivation of Hron [29], assume that the elastic parameters of the medium, i.e. both wave speeds $v_p = v_p(z)$,$v_s = v_s(z)$ and the density $\rho = \rho(z)$ are known functions of the depth z. Note, in this thesis the earth materials are assumed isotropic. Our

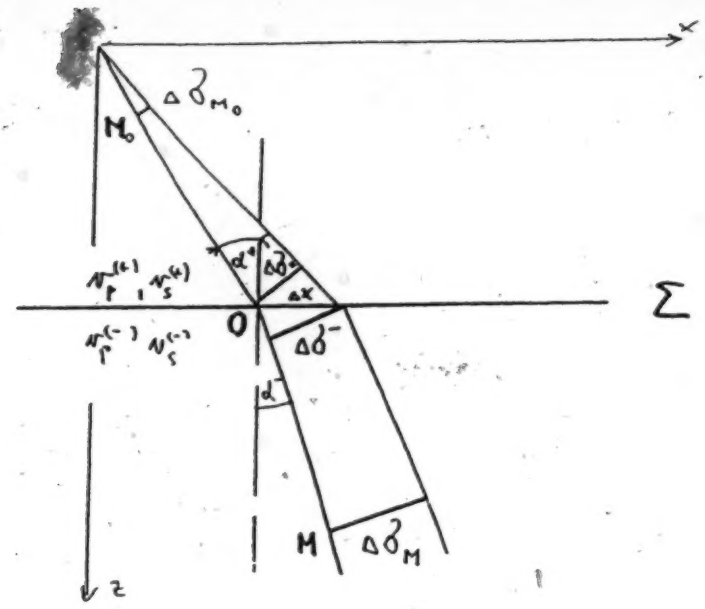

Figure 2.4: Evaluation of the discontinuity in geometrical spreading across the boundary during the transmission of the ray. [28]

objective is to determine the amplitude at point M on the transmitted ray assuming that the ray amplitude at M_o on the incident ray is known (Figure 2.4)

We will distinguish two different values at the point of incidence O by marking all quantities related to the incident wave by "+" and by labeling with "-" sign all quantities pertinent to the wave leaving the point of incidence (being either reflected from, or transmitted across, the boundary).

The cross section of the ray tube is given by $\Delta\Sigma = \Delta l_I \Delta l_{II}$, where Δl_1 and Δl_{II} are the linear dimensions of the ray tube in the direction parallel and perpendicular to the plane of incidence respectively. By using the concept of conservation of energy flux as described in Section 2.2.1, the change of amplitude between M_o and O and also O and M can be obtained. At point O,

$$\Delta\sigma^+ = \Delta l_I{}^+ \Delta l_{II}{}^+, \ \Delta\sigma^- = \Delta l_I{}^- \Delta l_{II}{}^- \tag{2.26}$$

But $\Delta l_{II}{}^- = \Delta l_{II}{}^+$ as both are taken at the same point O in the direction perpendicular to the plane of incidence and it is $\Delta l_{II}{}^- = \Delta l_{II}{}^+ = X(O)\Delta\phi_o$ where X(O) is the offset of the point of incidence O and $\Delta\phi_o$ is the angle between two vertical planes representing an angular horizontal dimension of the ray tube which is constant

for the entire ray. Hence

$$\frac{\Delta\sigma^-(O)}{\Delta\sigma^+(O)} = \frac{\Delta l_I^-(O)}{\Delta l_I^+(O)} = \frac{cos\alpha^-(O)\Delta x}{cos\alpha^+(O)\Delta x}, \tag{2.27}$$

where Δ is the horizontal dimension of that part of the plane interface Σ that is intersected by the incident and transmitted ray tubes, respectively and α^+, α^- are the angles of incidence and transmission at O. Thus we finally have

$$\tilde{L} = \sqrt{\frac{\cos\alpha^+(O)}{\cos\alpha^-(O)}}\sqrt{\frac{\Delta\sigma(M)}{\Delta\sigma(M_o)}} = \sqrt{\frac{\cos\alpha^+(O)}{\cos\alpha^-(O)}}\, L \tag{2.28}$$

where $\tilde{L}$ is the so called relative geometrical spreading of the ray tube between M_o and M and L denotes the absolute geometrical spreading.

2.2.3 The Gel'chinsky method

An exact derivation of equations describing the effect of curved interfaces on the curvature of incident spherical wavefronts can be obtained using the differential geometry of surfaces. This was done by Gel'chinsky [35] and the final formulas will now be given. Let

$r_1^{(0)}, r_2^{(o)}$	be the principal radii of curvature of the incident wavefront at the point of incidence (known values)
R_1, R_2	be the principal radii of curvature of the curved boundary at the point of incidence (known values)
$r_1^{(\nu)}, r_2^{(\nu)}$	be the principal radii of curvature of the wavefront leaving the boundary after reflection($\nu = 1,3$) or transmission($\nu = 2,4$) at the point of incidence O (unknown values)
ϕ_o	be the angle between the plane of incidence and the first principal normal section of the incident wavefront at O (known)
ψ	be the angle between the plane of incidence and the first principal normal section of the interface at O (known)
ϕ_ν	be the angle between the plane of incidence and the first principal normal section of reflected($\nu = 1,3$) or transmitted ($\nu = 2,4$) wavefronts (unknown)
v_o	phase speed of incident wave
v_ν	phase speed of the reflected ($\nu = 1,3$) or transmitted ($\nu = 2,4$) wave
θ_o	angle of incidence
θ_ν	angle of reflection($\nu = 1,3$)or transmission ($\nu = 2,4$)
n	v_ν/v_o

Then the unknown radii of curvature $r_1^{(\nu)}, r_2^{(\nu)}$ of the wavefront leaving the boundary after reflection ($\nu = 1, 3$) or transmission ($\nu = 2, 4$) are given by :

$$\frac{1}{r_{1,2}^{(\nu)}} = 1/2 \left\{ A + B \pm \frac{[(A-B)^2 \cos^2\theta_\nu + 4C^2]^{1/2}}{\cos_\nu} \right\} \tag{2.29}$$

$$\phi_\nu = 1/2 \arctan \left[\frac{2C}{(A-b)\cos\theta_\nu} \right] \tag{2.30}$$

where

$$A = \frac{1}{\cos^2\theta_\nu} \left[\frac{n\cos^2\theta_o}{r_{\|}^{(o)}} + \frac{n\cos\theta_o \pm \cos\theta_\nu}{R_{\|}} \right] + \frac{1}{\cos\theta_\nu} \left[\frac{\sin\theta_\nu}{v_\nu} \frac{\partial v_n u}{\partial l_{\|}^{(\nu)}} \right]$$
$$= \frac{1}{\cos\theta_\nu} \left(\sin\theta_o \frac{\partial n}{\partial x_{\|}} - \frac{n sin 2\theta_o}{2v_o} \frac{\partial v_o}{\partial l_{\|}^{(o)}} \right) \tag{2.31}$$

$$B = \frac{n}{r_{\|}^{(o)}} + \frac{n\cos\theta_o \pm \cos\theta_\nu}{R_\perp} \tag{2.32}$$

$$C = -n\cos\theta_o sin 2\phi 1/2 \left(\frac{1}{r_1^{(o)}} - \frac{1}{r_2^{(o)}} \right) - 1/2 \sin 2\psi \left(\frac{1}{R_1} - \frac{1}{R_2} \right)$$
$$(n\cos\theta_o \pm \cos\theta_\nu) + \sin\theta_o \frac{\partial n}{\partial x_\perp} \tag{2.33}$$

and

$$\frac{1}{r_{\|}^{(o)}} = \frac{\cos^2\phi_o}{r_1^{(o)}} + \frac{\sin^2\phi_o}{r_2^{(o)}}, \frac{1}{r_\perp^{(o)}} = \frac{\sin^2\phi_o}{r_1^{(o)}} + \frac{\cos^2\phi_o}{r_2^{(o)}} \tag{2.34}$$

$$\frac{1}{R_{\|}} = \frac{\cos^2\psi}{R_1} + \frac{\sin^2\psi}{R_2}, \frac{1}{r_\perp} = \frac{\sin^2\psi}{R_1} + \frac{\cos^2\psi}{R_2} \tag{2.35}$$

In Equations 2.31, 2.32 and 2.33, the upper sign applies to the reflected waves and the lower sign to the transmitted waves. The directional derivatives $\frac{\partial}{\partial l_{\|}^{(\nu)}}$ and $\frac{\partial}{\partial l_{\|}^{(o)}}$ stand for the directional derivatives in the direction parallel to the plane of incidence in the plane tangent to the wavefronts at the point of incidence. Similarly $\frac{\partial}{\partial x_{\|}}$ and $\frac{\partial}{\partial x_\perp}$ denote derivatives taken at the tangent plane to the surface at the point of incidence in the direction parallel and perpendicular to the plane of incidence. The

radii R_1 and R_2 are positive or negative depending on whether the corresponding normal sections are seen as convex or concave by an observer situated in the medium containing the incident wave.

In the case of homogeneous layers separated by flat interfaces perpendicular to the plane of the ray we get, $R_{\|} = R_{\perp} = \infty, \phi_o = 0, \psi = 0$ and $r_1^{(o)} = r_{\|}^{(o)}, r_2^{(o)} = r_{\perp}^{(o)}, R_1 = R_{\|}$ and $R_2 = R_{\perp}$. Therefore Equation 2.31 can be rewritten as :

$$r_1^{(\nu)} = r_{\|}^{(\nu)} = \frac{r_{\|}^{(o)}}{\Delta_{\|}}$$

$$r_2^{(\nu)} = r_{\perp}^{(\nu)} = \frac{r_{\perp}^{(o)}}{\Delta_{\perp}}$$

where

$$\Delta_{\|} = \frac{v_\nu}{v_o} \frac{\cos^2 \theta_o}{\cos^2 \theta_\nu}$$

$$\Delta_{\perp} = \frac{v_\nu}{v_o}$$

By generalizing Equation 2.28 to several interfaces, substituting for the radii of curvature, and making use of the above relationships, the relative geometrical spreading of the ray tube is then given by :

$$L^{\|} L^{\perp}$$

where

$$L^{\|} = \sqrt{\sum_{k=2}^{n} l_k \prod_{j=1}^{k-1} \Delta_j^{\|} + l_1} \tag{2.36}$$

$$L^{\perp} = \sqrt{\sum_{k=2}^{n} l_k \prod_{j=1}^{k-1} \Delta_j^{\perp} + l_1} \tag{2.37}$$

where n is the total number of ray segments and l_j is the length of the j-th ray segment.

2.2.4 Transmission effects

In Section 2.1 we derived equations for the propagation of seismic energy in a homogeneous isotropic continuum. However the earth is not this simple. A step forward

in complexity is made by considering the earth to be made of isotropic homogeneous layers. It then becomes necessary to consider what happens to the waves at the boundary between two such layers. Boundary conditions can be of two types and they concern displacement and stress components respectively. The former are referred to as kinematic boundary conditions whereas the latter are dynamic boundary conditions. The kinematic boundary condition states that for two solids in welded contact or a solid and a viscous fluid, all three components of displacement must be continuous at the boundary. The dynamic boundary condition states that the three components of stress must be continuous at a boundary.

These boundary conditions lead to the scattering matrix 2.38 when applied to the reflection and transmission of a P or S wave across a solid-solid interface, given here in the notation of Aki and Richards [30]:

$$\begin{pmatrix} \grave{P}\acute{P} & \grave{S}\acute{P} & \acute{P}\acute{P} & \acute{S}\acute{P} \\ \grave{P}\acute{S} & \grave{S}\acute{S} & \acute{P}\acute{S} & \acute{S}\acute{S} \\ \grave{P}\grave{P} & \grave{S}\grave{P} & \acute{P}\grave{P} & \acute{S}\grave{P} \\ \grave{P}\grave{S} & \grave{S}\grave{S} & \acute{P}\grave{S} & \acute{S}\grave{S} \end{pmatrix} \tag{2.38}$$

Each column of 2.38 represents the four waves scattered from the interface by a particular type of incident wave. The notation for the sixteen possible reflection and transmission coefficients is given in Figure 2.5. Following [30] the columns of this scattering matrix can be evaluated by setting up four systems of four equations in four unknowns.

Now if 1 denotes the incident medium and 2 the second medium, i and j denote the angle submitted with the normal by the P and S rays respectively, α and β denote the P wave and S wave velocities and ρ denotes density, for the case of an incident P wave in the upper medium the reflected waves are given by

$$\grave{P}\acute{P} = \left[\left(b\frac{\cos i_1}{\alpha_1} - c\frac{\cos i_2}{\alpha_2}\right)F - \left(a + d\frac{\cos i_1}{\alpha_1}\frac{\cos j_2}{\beta_2}\right)Hp^2\right] / D \tag{2.39}$$

$$\grave{P}\acute{S} = -2\frac{\cos i_1}{\alpha_1}\left(ab + cd\frac{\cos i_2}{\alpha_2}\frac{\cos j_2}{\beta_2}\right)p\alpha_1/(\beta_1 D) \tag{2.40}$$

and the transmitted waves are given by :

$$\grave{P}\grave{P} = 2\rho_1\frac{\cos i_1 F}{\alpha_2 D}$$

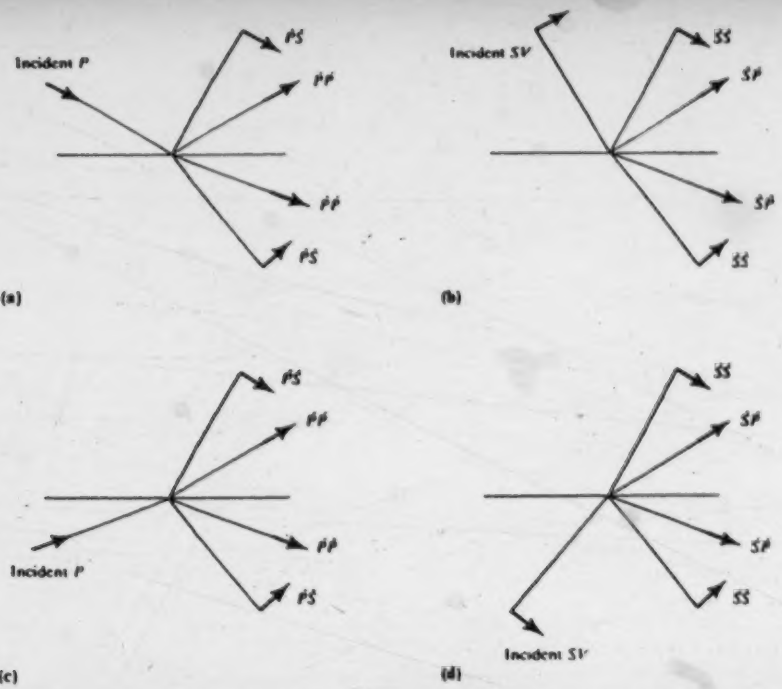

Figure 2.5: Notation for the sixteen possible reflection and transmision coefficients arising from problems of P-SV waves at the welded interface between two different solid half-spaces. [29]

$$\dot{P}\dot{S} = 2\rho_1 \frac{\cos i_1 Hp}{\beta_2 D}$$

where

$$a = \rho_2(1 - 2\beta_2{}^2p^2) - \rho_1(1 - 2\beta_1{}^2p^2) \qquad b = \rho_2(1 - 2\beta_2{}^2p^2) + 2\rho_1\beta_2{}^2p^2$$
$$c = \rho_1(1 - 2\beta_1{}^2p^2) + 2\rho_2\beta_2{}^2p^2 \qquad d = 2(\rho_2\beta_2{}^2 - \rho_1\beta_1{}^2)$$

and

$$E = b\frac{\cos i_1}{\alpha_1} + c\frac{\cos i_2}{\alpha_2} \qquad F = b\frac{\cos j_1}{\beta_1} + c\frac{\cos j_2}{\beta_2}$$
$$G = a - d\frac{\cos i_1}{\alpha_1}\frac{\cos j_2}{\beta_2} \qquad H = a - d\frac{\cos i_2}{\alpha_2}\frac{\cos j_1}{\beta_1}$$
$$D = EF + GHp^2$$

2.2.5 Energy flux

From Section 2.2.1 the energy flux is given by

$$\frac{dE}{dt} = \varepsilon c \Delta \sigma$$

where $\Delta\sigma$ denotes the cross-sectional area of the ray tube, c is the wave speed and ε is the volume energy density due to the wave motion. Hence for a harmonic disturbance traveling in a homogeneous isotropic medium, $\rho\alpha A^2\omega^2$ gives the maximum rate of energy flux transmitted across the unit area of a wavefront. This expression is then multiplied by $\cos i$ to obtain the flux rate across unit area of a horizontal boundary upon the wave is incident at angle i. By equating the incoming and outgoing energy flux across a boundary, we get

$$\begin{aligned}\rho_1\alpha_1\cos i_1 = \quad & \rho_1\alpha_1\cos i_1(\grave{P}\acute{P})^2 \quad +\rho_1\beta_1\cos j_1(\grave{P}\acute{S})^2 \\ & +\rho_2\alpha_2\cos i_2(\grave{P}\grave{P})^2 \quad +\rho_2\beta_2\cos j_2(\grave{P}\grave{S})^2 \end{aligned} \tag{2.41}$$

for the scattered wave system shown in Figure 2.5a. This equation places a constraint on the first column of the scattering matrix. The displacement amplitude corresponding to the $\grave{P}\grave{S}$ is the given by

$$\grave{P}\grave{S}\left(\frac{\rho_2\beta_2\cos j_2}{\rho_1\alpha_1\cos i_1}\right)^2 \tag{2.42}$$

The scattering matrix thus becomes :

$$\begin{pmatrix} \grave{P}\acute{P} & \grave{S}\acute{P}\left(\frac{\alpha_1\cos i_1}{\beta_1\cos j_1}\right)^2 & \acute{P}\acute{P}\left(\frac{\rho_1\alpha_1\cos i_1}{\rho_2\alpha_2\cos i_2}\right)^2 & \acute{S}\acute{P}\left(\frac{\rho_1\alpha_1\cos i_1}{\rho_2\beta_2\cos j_2}\right)^2 \\ \grave{P}\acute{S}\left(\frac{\beta_1\cos j_1}{\alpha_1\cos i_1}\right)^2 & \grave{S}\acute{S} & \acute{P}\acute{S}\left(\frac{\rho_1\beta_1\cos j_1}{\rho_2\alpha_2\cos i_2}\right)^2 & \acute{S}\acute{S}\left(\frac{\rho_1\beta_1\cos j_1}{\rho_2\beta_2\cos j_2}\right)^2 \\ \grave{P}\grave{P}\left(\frac{\rho_2\alpha_2\cos i_2}{\rho_1\alpha_1\cos i_1}\right)^2 & \grave{S}\grave{P}\left(\frac{\rho_2\alpha_2\cos i_2}{\rho_1\beta_1\cos j_1}\right)^2 & \acute{P}\grave{P} & \acute{S}\grave{P}\left(\frac{\alpha_2\cos i_2}{\beta_2\cos j_2}\right)^2 \\ \grave{P}\grave{S}\left(\frac{\rho_2\beta_2\cos j_2}{\rho_1\alpha_1\cos i_1}\right)^2 & \grave{S}\grave{S}\left(\frac{\rho_2\beta_2\cos j_2}{\rho_1\beta_1\cos j_1}\right)^2 & \acute{P}\grave{S}\left(\frac{\beta_2\cos j_2}{\alpha_2\cos i_2}\right)^2 & \acute{S}\acute{S} \end{pmatrix} \tag{2.43}$$

From the above discussion it is apparent that the amplitudes of the reflected and transmitted waves are dependent on the incidence angle as well as on the acoustic properties of the two media defining the boundary. Figure 2.6 shows this behavior for the case where $\frac{\alpha_2}{\alpha_1} = 0.5$, $\frac{\rho_2}{\rho_1} = 0.8$ and $\Upsilon_1 = 0.3$ and $\Upsilon_2 = 0.25$. Here Υ denotes Poisson's ratio which for a homogeneous medium relates the P and S wave velocities through

$$\frac{V_p^2}{V_s^2} = \frac{2(1-\Upsilon)}{(1-\Upsilon)}.$$

[16] et al. have computed the energy ratios and phase angles for different choices of elastic parameters and densities. This variance of reflected amplitude with angle of

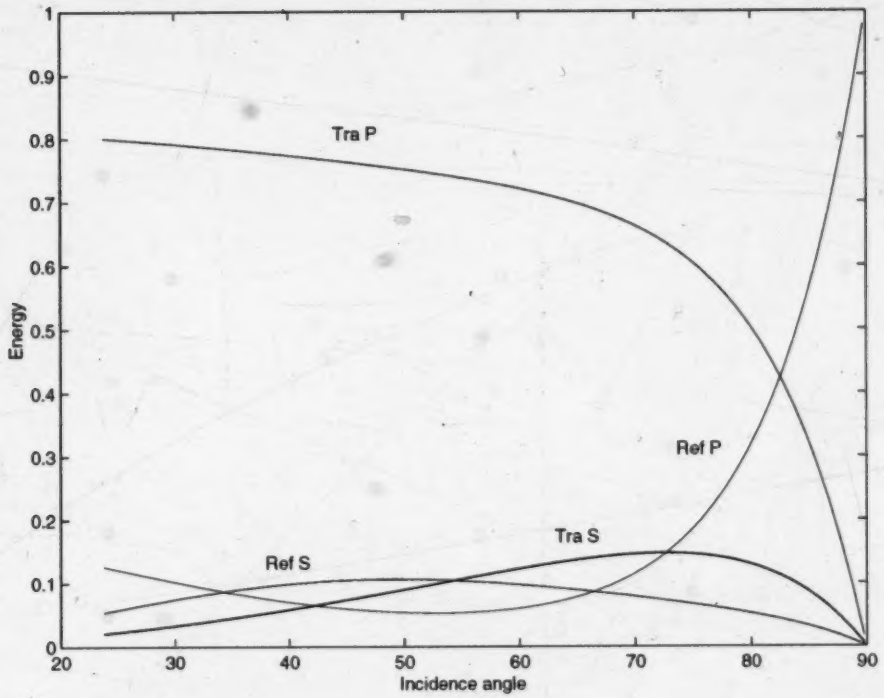

Figure 2.6: Energy Reflection Coefficients vs Angle of incidence for an incident P wave. α_2 / $\alpha_1 = 0.5$, ρ_2 / ρ_1 =0.8 and $\sigma_1 = 0.3, \sigma_2 = 0.25$.

incidence and elastic parameters (or Poisson's ratio) is the fundamental idea behind the "amplitude versus offset" studies we will be discussing later.

2.2.6 Attenuation

So far we have considered wave propgation through elastic media. However, real media exhibit various amounts of anelastic behaviour and thus a first order derivative term needs to be included in the wave equation. Hence the equation of motion for damped oscillations is

$$\ddot{u}(t) + D\dot{u}(t) + \omega_o^2 u(t) = 0$$

where ω_o is the natural frequency of the undamped system and D is the damping constant per unit mass [31]. This equation has solution of the form

$$x(t) = e^{-t/2\tau} \cos(w_1 t + \theta)$$

where $\tau = 1/D$ and $\omega_1^2 = \omega_o^2 - (D/2)^2$. for weakly damped systems, it can be assumed that $e^{-t/2\tau}$ remains constant during one oscillation. Then the time derivative of x can be written as

$$\dot{x}(t) = e^{-t/2\tau} \sin(w_1 t + \theta). \tag{2.44}$$

Since the total energy of the system is given by

$$E = \frac{1}{2} M \dot{x}^2 + \frac{1}{2} M \omega_o^2 x^2$$

we get

$$E = E_o e^{-Dt}$$

where $E_o = M(\omega_1^2 + \omega_o^2)/2$. If we let $D = \omega_1/Q$, then Equation 2.44 is a solution to

$$\frac{dE}{dt} = \frac{-\omega_1 E}{Q}.$$

This defines Q as

$$Q = \frac{\omega_1 E}{-dE/dt}.$$

Hence the quality factor Q is proportional to the ratio of the elastic energy stored in the wave to the energy lost in one cycle or wavelength. For a perfectly elastic material Q is infinite as opposed to 0 for a totally dissipative medium. On this basis a highly attenuative medium is said to have a low Q value and vice-versa.

2.2.7 Directivity Effects

In seismic exploration energy is introduced into the ground using impulsive sources, explosive sources or a continuous vibrating source. Usually these sources can be considered as points and geometric effects apply as described in section 2.2.1. However for many seismic sources, the energy is not only a function of distance but also of the direction of the initial ray leaving the source point. Following the discussions of [32], we will consider the directivity effects of a point source below the surface and a vibrator type of source at the surface.

Consider a point source buried in an isotropic homogeneous fluid medium at a finite distance h from the surface. Then a detector at a point P located at a distance R such that R >> h, will also see a virtual source located at a distance h above the surface (Figure 2.7).

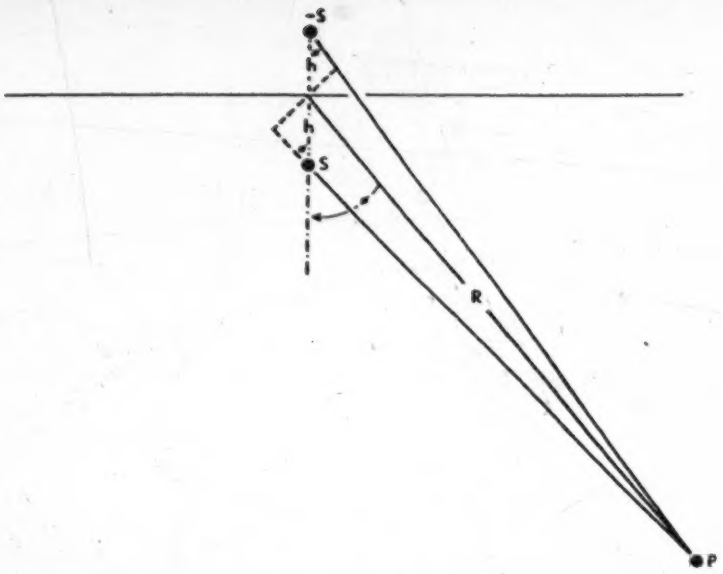

Figure 2.7: Geometry for calculation of amplitude as a function of the vertical angle θ for a source below a free surface (From [32]).

Since both the source and its mirror image are located on the vertical axis, the generated waves are independent of azimuth. For a harmonic disturbance, the wave amplitude at a distance R from a single source of frequency ω is then given by

$$\xi = \frac{A}{R}[\cos\omega(t-t') - \cos\omega(t+t')]$$

where t' is the time difference due to the path difference $h\cos\phi$. Now

$$\omega t' = \frac{\omega h\cos\phi}{c} = \frac{2\pi h}{\lambda}\cos\phi.$$

Therefore

$$\xi_R = \frac{A}{R}\sin\omega t\sin\left(\frac{2\pi h\cos\phi}{\lambda}\right) \tag{2.45}$$

Figure 2.2.7 shows the directivity patterns of a point source for different ratios of h/λ.

One of the most frequently used seismic energy sources on land is the vibrator where a vibrating metal plate is used to introduce a long train of waves of gradually changing frequency. [33] have provided the mathematical treatment for the directivity effects of the energy generated by a circular disk of finite radius vibrating normally to the surface of a medium. The upper part of Figure 2.2.7 shows the P wave motion for different values of Poisson's ratio and the lower two figures show the SV

motion (perpendicular to the direction of travel). Source radiation patterns remain problematic and will not be considered in this thesis which focuses more on the geologic and geometric effects. Later work will assume directivity may be ignored. This is a reasonable assumption for the VSP case studied here as the range of angles leaving the source to a reflected event is small.

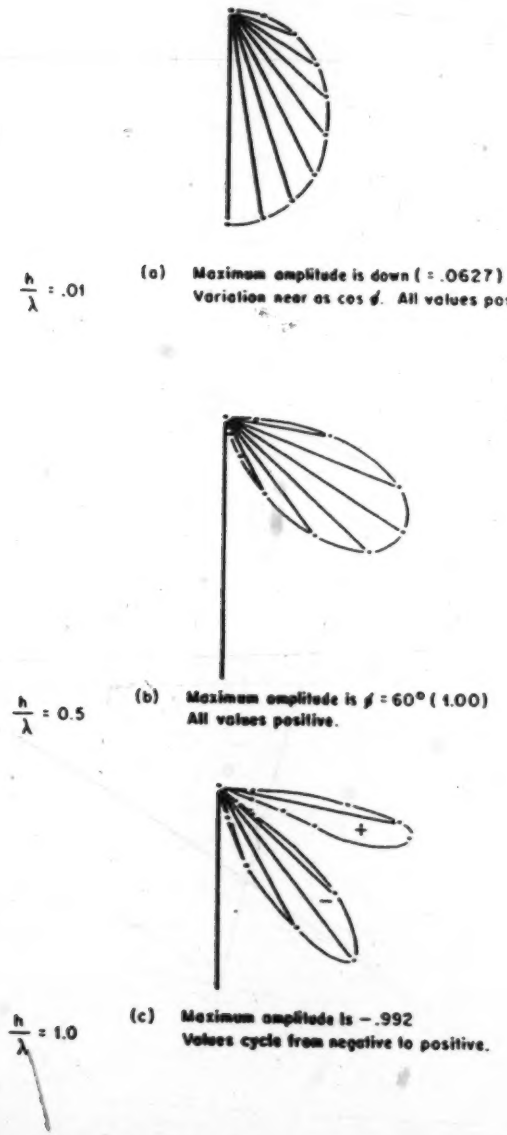
$\frac{h}{\lambda}$ = .01
(a) Maximum amplitude is down (= .0627)
Variation near as cos ϕ. All values positive.
$\frac{h}{\lambda}$ = 0.5
(b) Maximum amplitude is ϕ = 60° (1.00)
All values positive.
+
−
$\frac{h}{\lambda}$ = 1.0
(c) Maximum amplitude is −.992
Values cycle from negative to positive.

Figure 2.8: Directivity patterns of a monochromatic P wave point source below a free surface for different ratios of h/λ. From [32].

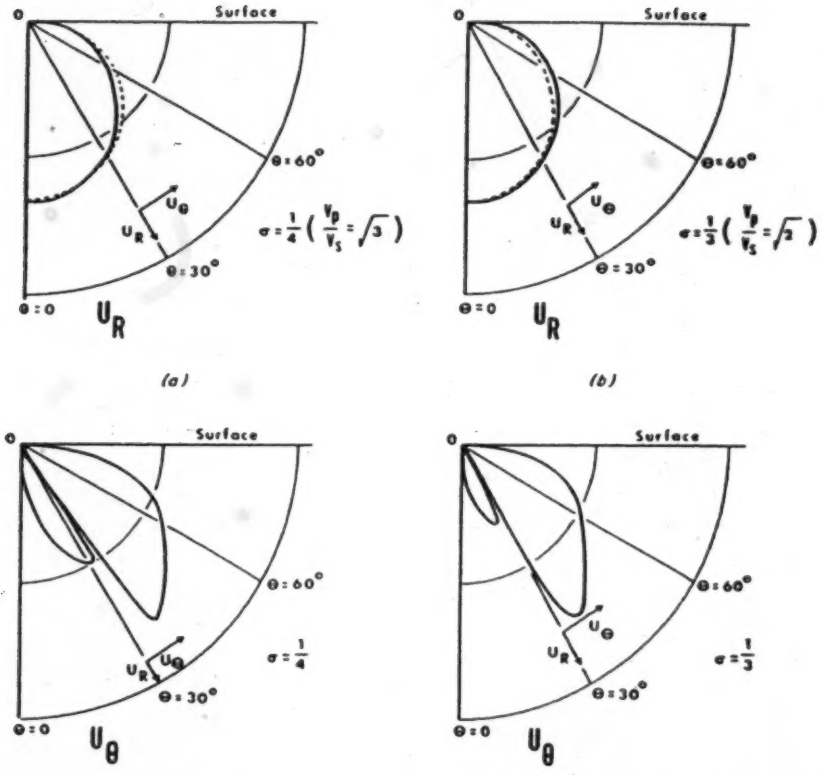

Figure 2.9: Directivity functions for a disk vibrating in a direction perpendicular to the ground surface for different values of Poisson's ratio Υ. The dashed line is just a reference line for comparison purposes. u_R denotes the P wave and u_θ denotes the S wave. From [33].

Chapter 3

A model based amplitude correction

3.1 The VSP

3.1.1 Introduction

Seismic methods play a major role in the exploration for hydrocarbons. Complications in seismic interpretations arise from complexities of the earth in which the wave is propagating. In simple geologic situations both dynamic and kinematic information may be derived from the analysis of seismic wavefield obtained in surface experiments. However the authenticity of the geological interpretation becomes doubtful when the model becomes complex. The degree of uncertainty could be minimized if one was able to directly make measurements of the seismic waves as they travel in the medium.

Vertical Seismic Profiles (VSP's) can provide us with information on the formation of the wavefield as it propagates in the medium. In the simplest case, a shot is fired close to the borehole head and the transit time at different depths down the borehole is measured providing both interval and average velocity estimate of the earth (Figure 3.1). Further information is obtained by recording both the reflected events and the direct arrivals.

The method of the VSP as we know it today was developed following field work by the Institute of Physics of the Earth of the Academy of Sciences of the USSR in 1959. Experimental investigations were carried out in different geological environments and the first instrument systems and experimental procedures were developed. These investigations clarified and established the basic capabilities of the method. They

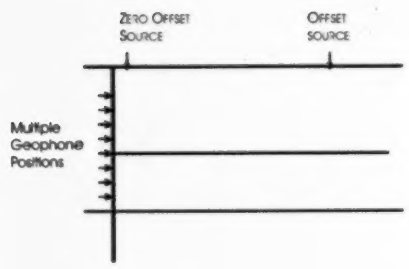

Figure 3.1: Field setup for an offset VSP. Several geophones in a borehole measure waves generated by a surface source.

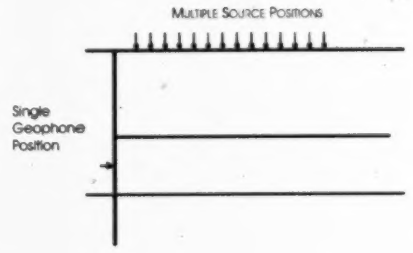

Figure 3.2: Field setup for a walkaway VSP

showed the complexity of seismic maps obtained from surface experiments and also their dependence on the shallow part of the section (Gal'perin [36]).

Since then, VSP's have been used routinely in the search for hydrocarbons and their usefulness more understood. As described by Hardage [37], VSPs provide invaluable information about structural, stratigraphic and lithological information of the subsurface and compliment data acquired only at the subsurface. They are an excellent tool for the identification of primaries and multiple reflections, estimation of reflector dip, correlation of shear and compressional wave reflections, location of fault planes, determination of lithological effects on propagating wavelets, measurement of both compressional and also shear wave velocities and estimation of mode conversion within the earth. Furthermore in a VSP, the different wave modes constituing the seismic wavefield can be identified with less ambiguity than in surface experiments and are easily correlated to the true geologic stratigraphy (Gal'perin [36]). Hence a VSP can aid enormously in the assessment of information derived from a surface seismic experiment.

3.1.2 VSP setups

VSP experiments can be divided into two categories. The first category involves a single source and a series of receivers in the borehole. The source can be located at an offset distance from the surface well head, this referred to as an offset VSP. A zero offset VSP with the source very close to the well head is a special case. Another definition requires an array of sources to be placed at different offsets from the well head with a single receiver down the borehole. This geometry is referred to as a Walkaway VSP. Figures 3.1 and 3.2 illustrate these different field setups.

As shown in the derivation of the wave equation in Section 2.1 seismic energy propagates in the ground in the form of a wave. Furthermore, all plane waves in an isotropic elastic medium propagate with one or the other of the two speeds as given in Equations 2.11 or 2.18. Unfortunately however, analytical solutions to the wave equations are known only for a few relatively simple media which generally do not closely resemble the real earth. An approximate solution is attempted by decomposing the total wavefield into an infinite number of contributions each of which can be attributed to a single ray. The ray or raypath is the path along which the energy travels from the source to the receiver. Hence synthetic seismic sections can be generated corresponding to different earth models of varying complexities. This approach was adopted in this work to generate synthetic VSP plots.

In the following sections several model examples of increasing sophistication are provided for illustrative purposes. In each the ray paths and resulting simple seismograms that would be observed are included. Before going on to this we will discuss the ray tracing program used to generate these synthetics.

3.1.3 The ray tracing program

The ray tracing program written in MATLAB, consists of a master program MASTER.M and several subprograms. The main function of MASTER.M is to generate synthetic seismograms for offset VSP geometries. Given the acquisition geometry and earth parameters which define the model, the transit times for direct and reflected energy are calculated together with the geometrical spreading coefficients, and transmission effects. In the case of reflected arrivals, amplitude variation with angle of

incidence is also calculated. The input and output parameters are enlisted in Table 3.1 and the program is included in Appendix B.

Input Parameters
Source Offset
Number of receivers
Receiver Separation
First receiver
Number of layers in model
P wave velocity for each layer
S wave velocity for each layer
Density for each layer
Depth of interfaces defining the model
Number of reflectors
Reflector number
Output Parameters
Direct arrival transit time
Reflected event transit time
Direct arrival relative amplitude
Reflected arrival relative amplitude
Geometrical spreading coefficients
Transmission effect coefficients
Amplitude variation with angle

Table 3.1: Input and output parameters for MASTER.M

After reading the model parameters and acquisition geometry a model diagram is generated by calling DGRM.M. The first part of MASTER.M deals with the primary event, or energy which travels directly from the source to the receivers without being reflected at any interface. The second part handles reflected events, or energy which is reflected once from an interface and travels upward after reflection. The ray tracing is similar for both primary and reflected energy and is done in the subprograms DIRECT.M and REFLECT.M which compute the kinematic and dynamic properties for the primary and the reflected energies respectively. A ray is shot out from the source position at an arbitrary set angle and is traced to the receiver using Snell's law.

The procedure is repeated until the traced ray is less than a specified distance from the receiver. Once this convergence criterion is met, the path length and hence the transit time are computed. Using the Gelchinsky method, the geometrical coefficients for that ray path are then computed. The transmission coefficients are calculated using Zoeppritz equations as implemented in the subprogram AMPS.M. The transmission and geometric effects are then multiplied to calculate the relative amplitude for that event. The dynamic and kinematic results obtained are all displayed as graphs.

3.1.4 Illustrative examples

The responses expected from a series of simple but progressively more sophisticated geologic models are presented in order to illustrate many of the competing factors which can influence observed amplitudes in VSP sections.

Layer over a halfspace

The first case to be considered is that of a thick layer over a halfspace. By thick layer one assumes that the thickness is substantially greater than the predominant wavelength of the propagating pulse.

Layer No.	Depth	P Wave Velocity
	0	
1		2000
	500	
2		3500
	1000	

Table 3.2: Illustrative Model 1 - Layer over half space

Table 3.2 gives the model parameters whereas Figures 3.3 and 3.4 illustrate the propagation paths of the rays through the model for geophones spaced of 20m along the wellbore at source offsets of 300m and 600m, respectively. This simple example illustrates the inhomogeneous distribution of the raypaths. Particularly in Figure 3.4, there is a 'shadow zone' in the upper layer through which no rays are present. This is due to the sharp bending at the interface of the rays traveling to the geophones in the deeper medium. This effect is also characteristic of the reflected rays. Furthermore

this effect is greater for the larger offset as seen by comparing Figure 3.4 with Figure 3.3.

Data acquired in a VSP is plotted in seismic traces according to geophone depth versus time. Figures 3.5 and 3.6 are the VSP plots corresponding to Figures 3.3 and 3.4, respectively. In this case, only the kinematic properties (ie. the raypaths) are examined and it is assumed that there are no amplitude losses. That is, the pulse arrival times indicate only the travel time from the source to the receiver.

The most basic features to note in comparison of Figures 3.5 and 3.6 is that they both have the same pattern of events, and that the events on Figure 3.6 are at a later time than those in Figure 3.5 due to a greater source offset. One also notes the jump in time observed at receiver No. 11 in Figure 3.6 for the case when the source offset is comparable to the interface depth. This is due to travel paths in the second medium which are close to the critical travel path and which are distinctively longer than those traveling only in the first medium. But since the second medium has a higher velocity than the first or top layer, the transit time is smaller for receiver No. 11 than it is for receiver No. 10. Again, it is worth noting that this effect is offset dependent. This explains the absence of discontinuities for the 300m offset (Figure 3.5).

Another characteristic of VSPs arising from these two figures is that the reflected event is only present at receivers Nos 1 through 9, ie. those receivers which lie above the reflectors. Though perhaps obvious, this feature is important in correlating seismic events with geologic reflectors. Furthermore by correlating the VSP with a surface seismic plot, one can also relate with more confidence events on the surface seismic map with geologic horizons.

One final feature to note is that even though the receivers are regularly spaced along the borehole, the two layers constituting the model are homogeneous and isotropic and the interface defining the two layers is flat the direct arrival event on the VSP plot is curved. This again is due to Snell's Law and simple geometry. The varying angle of incidence for the different receivers increases with source offset.

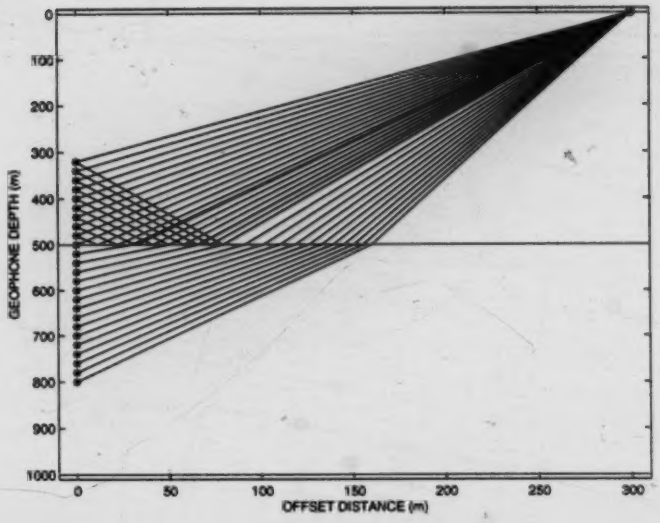

Figure 3.3: Ray diagram for a layer over halfspace and a source at 300m offset for illustrative Model 1

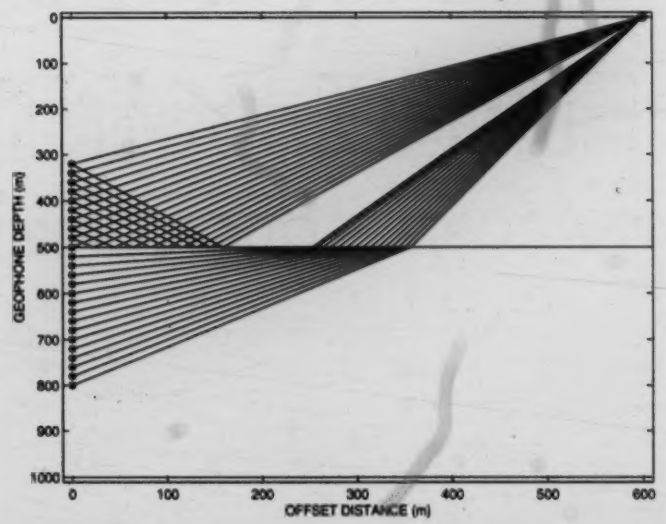

Figure 3.4: Ray diagram for a layer over halfspace and a source at 600m offset for illustrative Model 1

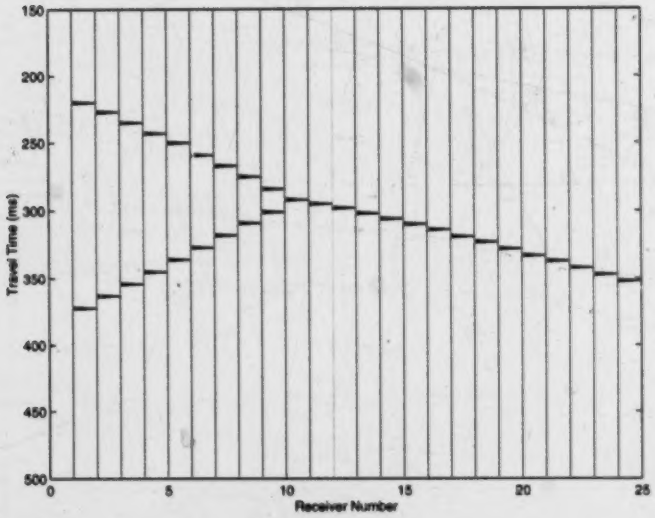

Figure 3.5: VSP plot for geometry in Figure 3.3. Increasing receiver number corresponds to increasing depth. Receivers from 800m to 320m at 20m depth increments.

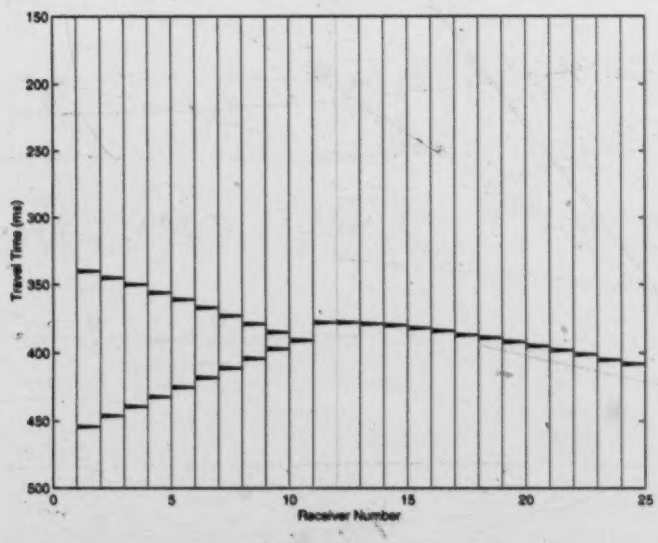

Figure 3.6: VSP plot for geometry in Figure 3.4. Increasing receiver number corresponds to increasing depth. Receivers from 800m to 320m at 20m depth increments.

Layer in a half space

The second example consists of a thick layer in a halfspace. This is illustrated for the two cases when the velocity of the layer is greater and then smaller than that of the surrounding halfspace. The model parameters are given by Tables 3.3 and 3.4 with the corresponding ray trace diagrams for a 300m offset given in Figures 3.7 and 3.8 respectively.

Layer No.	Depth	P Wave Velocity
	0	
1		2000
	500	
2		3500
	600	
3		2000
	1000	

Table 3.3: Illustrative model 2 - Thick fast layer in halfspace

Layer No.	Depth	P Wave Velocity
	0	
1		3500
	500	
2		2000
	600	
3		3500
	1000	

Table 3.4: Illustrative model 3 - Thick slow layer in halfspace

It can be seen that the reflected rays cover more of the model in Figure 3.7 than in Figure 3.8. This is due to the differences in refraction according to Snell's law at the interfaces.

Figures 3.9 and 3.10 show the VSP plots corresponding to Figures 3.7 and 3.8 respectively. Since the rays spend less time in a medium with higher velocity, the events in Figure 3.10 arrive earlier than those in Figure 3.9. Another interesting feature to note is the slopes of the events (change in transit time over a fixed number of receivers) is greater for lower velocities. As the layer is considerably thicker than the

wavelength, no interference occurs between the reflections from the top and bottom interfaces of the layer.

In contrast to the first illustrative example, amplitude variations are seen in Figures 3.9 and 3.10. Aside from the decrease in spike amplitude with increasing receiver number, discussed more thoroughly in the forthcoming section, one also notices a change in the polarity of the spike for the first or top reflector in Figure 3.10 and for the bottom reflector in Figure 3.9. Both these polarity reversals are due to reflection from an interface where the acoustic impedance of the second medium is smaller than the acoustic impedance of the incident medium. To see this, consider the case of zero offset where the rays are close to the vertical. Then i and j in Section 2.2.4 are close to zero such the coefficient of reflection R (ratio of reflected amplitude to incident amplitude) is given by:

$$R = \frac{\rho_2 v_2 - \rho_1 v_1}{\rho_2 v_2 + \rho_1 v_1}$$

and $R + T = 1$ where T is the transmission coefficient. Since density and speed are always positive quantities, it follows that $R < 0$ if and only if $\rho_2 v_2 < \rho_1 v_1$. On the other hand, T is always greater than zero for $\|R\|$ is always < 1.

Multilayer model

The final example defined in Table 3.5, is a more complex multilayer model which simplistically represents a typical geological environment with a series of thin layers such as coals (low velocity and impedance) or carbonates (typically high velocity and impedance). The ray trace diagram and the VSP plot are given in Figures 3.11 and 3.12 respectively. Once again we notice the amplitude decay with increasing depth and also the polarity reversal of the spikes corresponding to interfaces No. 3 and No. 7. The sharp jump in transit time on the primary energy at receiver No. 11 indicates a considerable jump in the acoustic properties across the top interface. This is also accompanied by a considerable amplitude loss as seen in Figure 3.12. Interface number eight is the reflector studied and in the following sections we will discuss its amplitude characteristics as well as the influence of the interbed layers above it.

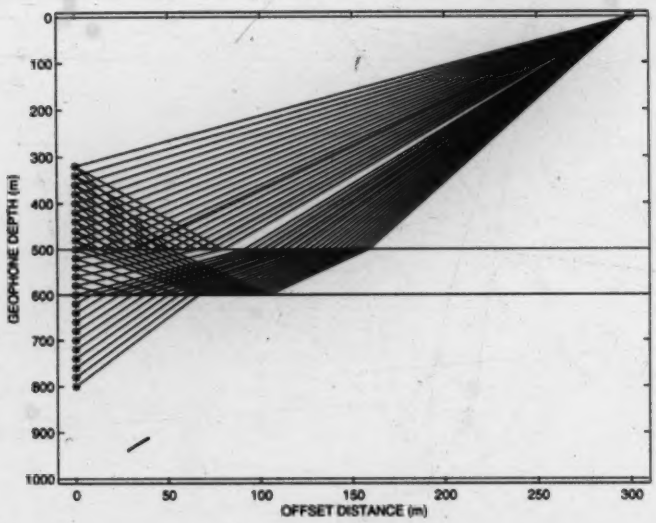

Figure 3.7: Ray diagram for slow model described in Table 3.3. Source offset 300m.

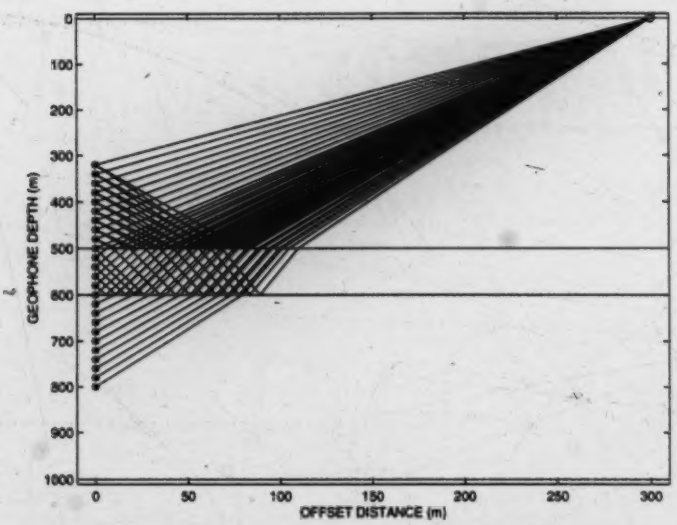

Figure 3.8: Ray diagram for fast model described in Table 3.4. Source offset 300m.

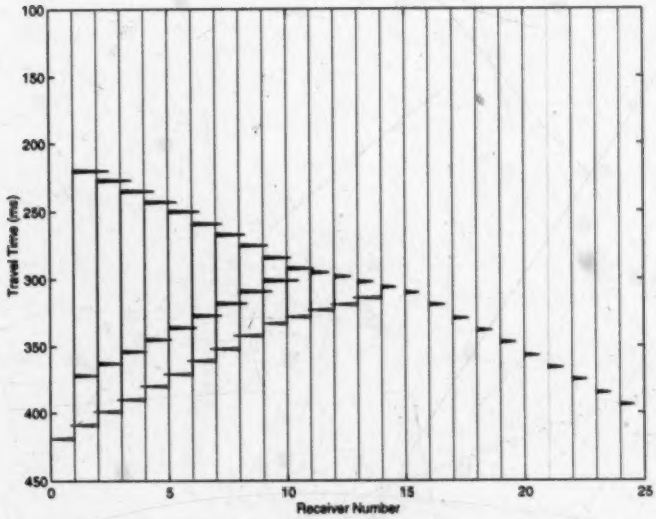

Figure 3.9: VSP plot for geometry in Figure 3.7

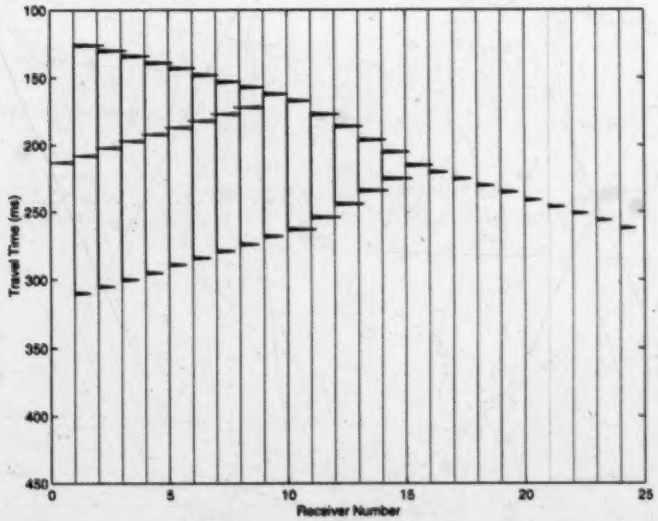

Figure 3.10: VSP plot for geometry in Figure 3.8

Layer No.	Depth m	P Wave Velocity ms^{-1}	S Wave Velocity ms^{-1}	Density kg/m^3
	0			
1		2900	2147	2400
	500			
2		3600	2235	2575
	1000			
3		3700	2176	2600
	1700			
4		3600	2118	2575
	2000			
5		4300	2529	2750
	2100			
6		4500	2647	2800
	2500			
7		5500	3235	3050
	2600			
8		5200	3118	3000
	3000			
9		6000	3529	3175
	4000			

Table 3.5: Illustrative model 4 - Multilayer model

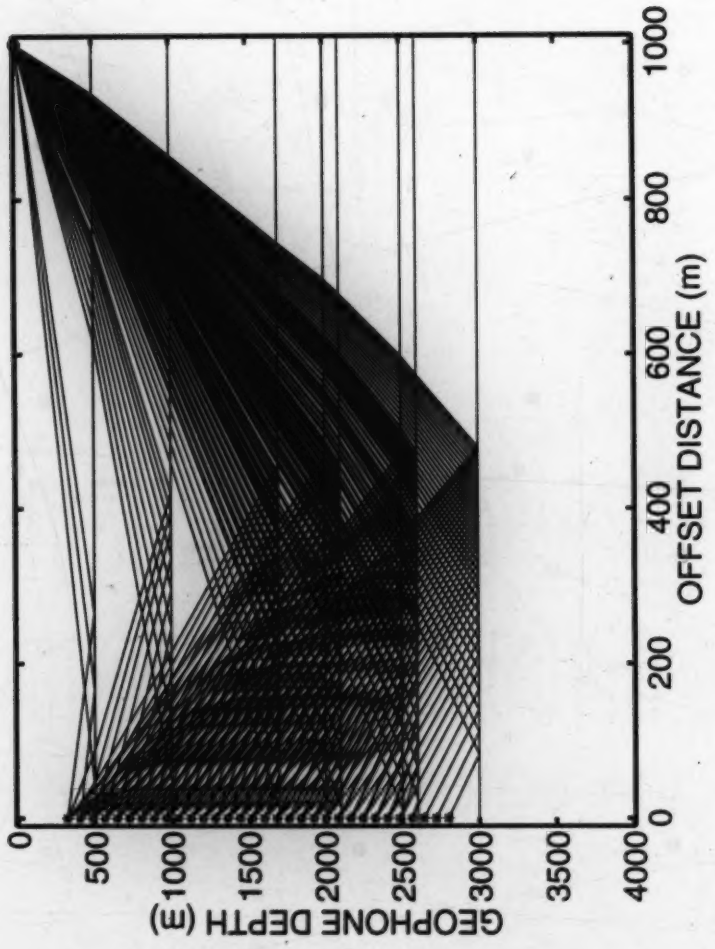

Figure 3.11: Ray diagram for model described in Table 3.5

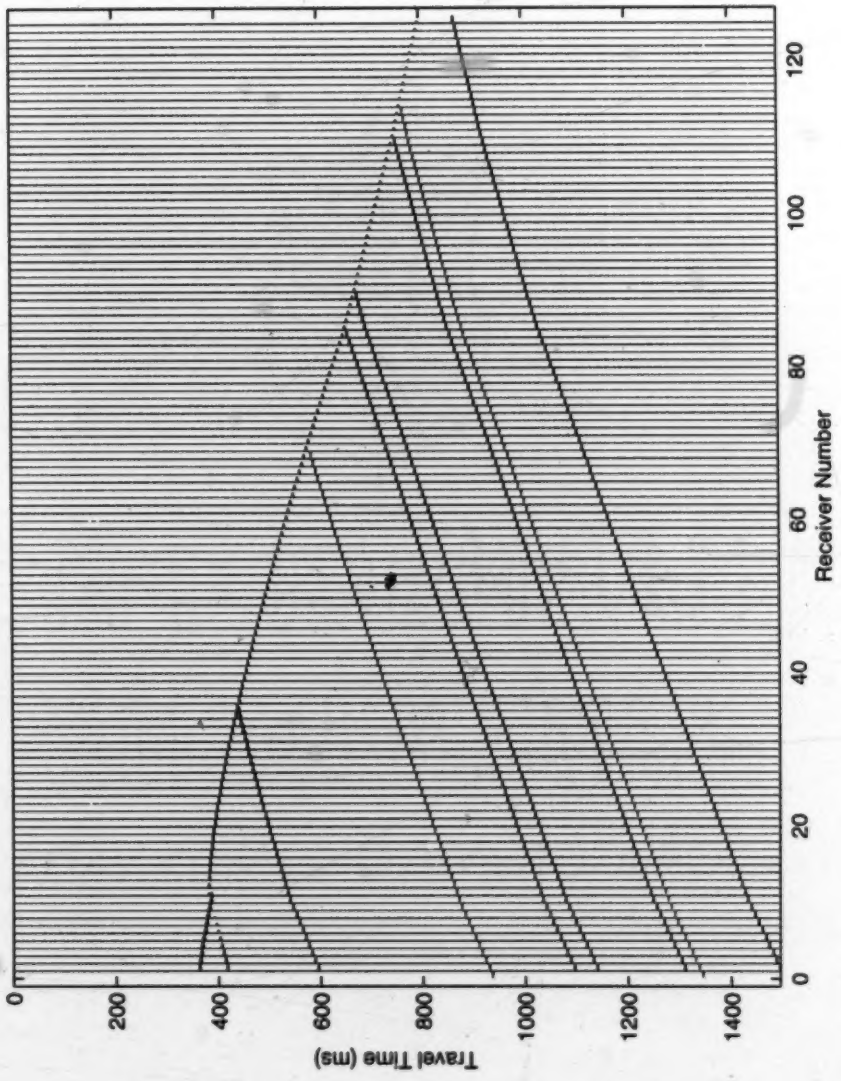

Figure 3.12: VSP plot for geometry in Figure 3.11

3.2 Amplitude restoration

3.2.1 VSP processing

In reality, an acquired VSP appears as Figure 3.13. Here the effects of multiples, converted energy, and noise are all superimposed. Similar to a surface seismic plot, a VSP contains both dynamic and kinematic information, ie. both the amplitudes and transit times can be used to yield information about the subsurface. As mentioned in section 2.2.4, the observation of the variation in reflection amplitude with incidence angle provides, in principle, sufficient information to infer the lithologic parameters of the two layers defining the interface. However in order to extract this critical infromation, all other superimposed effects need to be properly corrected for.

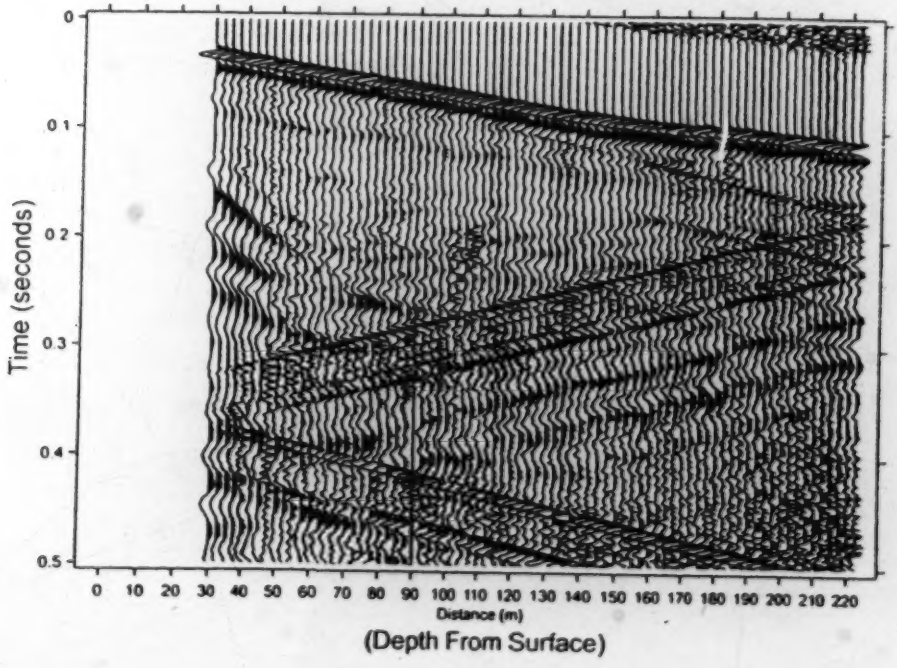

Figure 3.13: A real VSP plot including multiples, converted energy and noise.

In a VSP experiment the receivers are located below the source in a borehole and consequently record two different wavefields. We assume that these two wavefields, referred to as the upgoing and the downgoing, superimpose linearly. The primary (first) event recorded is the response of the propagating energy travelling directly

from the source to the receivers. This event together with all its associated multiples and converted wave energy comprises the downgoing wavefield. The upgoing wavefield constitutes all the energy which is reflected from interfaces and which approaches the receivers from below. Figure 3.2.1 shows the rays which give rise to the upgoing and downgoing wavefields whilst Figure 3.15 and Figure 3.16 show the downgoing and upgoing plots for the multilayer model described in Table 3.5. Since no multiples or converted rays were included in the ray tracing, these plots are very simple and show only the reflected and the direct arrivals respectively.

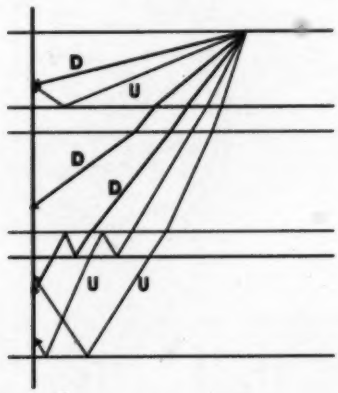

Figure 3.14: Cartoon showing rays constituting the upgoing and downgoing wavefields. Rays marked by a U form the upgoing wavefield and the rays marked by a D form the downgoing wavefield

A typical value for the portion of energy reflected from a geologic interface is on the order of 1 % of that incident. Further, this upgoing reflected energy must travel further than that in the downgoing energy. Consequently, amplitudes of the upgoing wavefield are in general substantially smaller than those of the downgoing wavefields. As a result, the combined observed wavefield (e.g. Figure 3.13) can be difficult to interpret and determination of amplitudes in the weak upgoing wavefield virtually impossible.

A routine VSP processing scheme includes the resolution of the wavefields into horizontal and vertical particle motions, wavefield separation into up-going and down-going wavefields, and multiple suppression. The common processing steps are not the

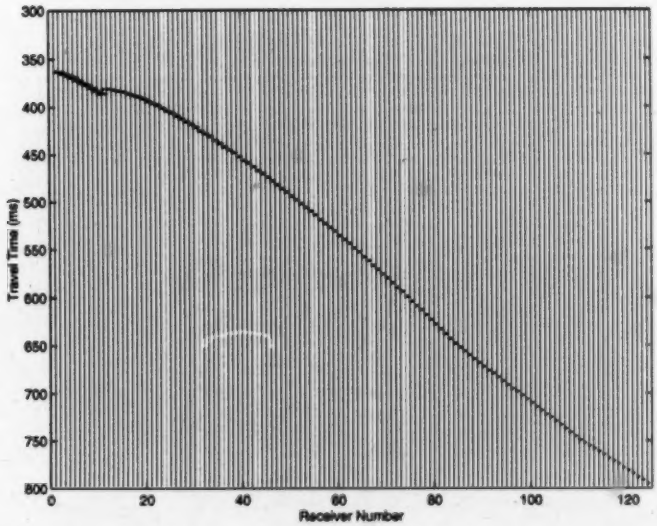

Figure 3.15: Downgoing wavefield for illustrative model 4 (Table 3.5).

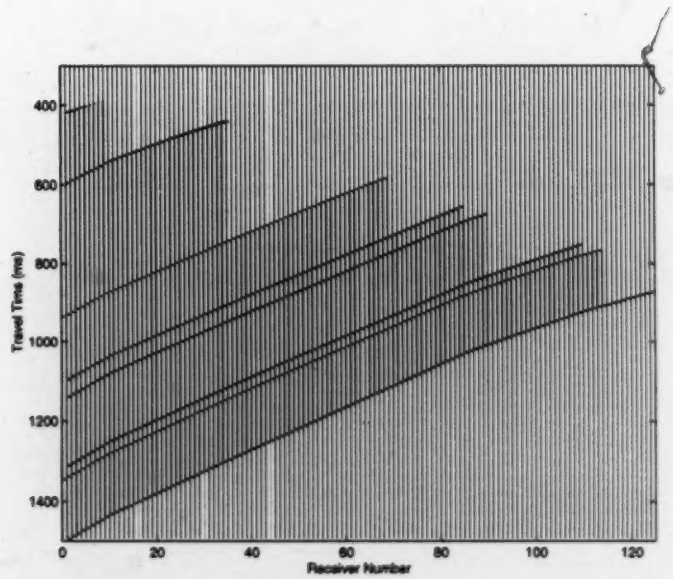

Figure 3.16: Upgoing wavefield for illustrative model 4 (Table 3.5).

purpose of this contribution but a short discussion is necessary for understanding in later chapters.

Nowadays it is common practice to employ a three component geophone when acquiring a VSP and this subject and its applications is well covered in the geophysical literature. Gal'perin and Frolova [45], [46] describe this methodology in their 1961 papers and an account of three component VSP applications is found in Gal'perin [47], 1977. A three component geophone measures the wavefield in the vertical and in two horizontal directions. However as the logging tool twists in the borehole, the horizontal components are randomly oriented from depth to depth. Hence orienting the horizontal components to a fixed reference frame becomes important for wave correlation from depth to depth (Di Siena [48], Esmersoy [49]).

Energy traveling from the source to the receivers can follow more complex raypaths than those shown in Figure 3.2.1. These complex raypaths involve multiple reflections off one or more interfaces and the returns are collectively known as multiples (as opposed to the raypaths in Figure 3.2.1 which are termed primaries). Of course the amplitude of this multiple energy is increasingly diminished with the number of reflections. However they can be strong enough to mask deeper events or converted energy which are weaker in magnitude. Furthermore they can cause other filtering effects such as the apparent attenuation effect described by Schoenberger and Levin [15] [52]. Of course multiples are also present in surface seismic and there is an extensive literature on their characterization and different approaches for their elimination.

In surface seismic work, multiple attenuation can be categorized into two groups. The first group of techniques make use of their differential normal moveout velocities. Since multiples tend to spend more time in shallower or lower velocity layers, they tend to have a greater moveout with offset then their corresponding primaries (Hatton et al. [40]) and thus can be attenuated using a stacking procedure or a velocity or FK filter. The second method for multiple attenuation makes use of their periodicity. Since multiples tend to have a constant time delay behind their corresponding primary, predictive deconvolution and its variances (e.g. Tsai [50]) can be used to suppress them.

The VSP contains both an upgoing as well as a downgoing wavefield which in-

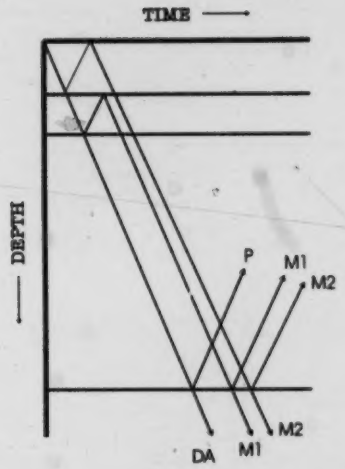

Figure 3.17: Cartoon showing multiples in the upgoing wavefield and their relationship with the downgoing multiples.

clude upgoing and downgoing multiples respectively. By separating the upgoing from the downgoing wavefields, attenuation techniques can be designed on the downgoing wavefield and then applied to both the downgoing and upgoing wavefields (Figure 3.17). Furthermore wavefield separation allows multiple identification as described by Molyneux at al. [51]. The attenuation techniques applied are similar to those in surface seismic.

The simplest method of wavefield separation is through the application of a median filter as described by Hardage [20]. This essentially involves a trace by trace subtraction of the estimated wave mode that is to be attenuated. A critical point in the application of this method is accurate time picking of events involved in the subtraction process.

Another frequently applied method of wavefield separation in the industry is that described by Seeman and Horowicz [42]. Wavefield separation is achieved by modeling the recorded seismic data in terms of the upgoing and downgoing wavefields and extracting them using a mathematically optimal least-squares technique. Aminzadeh [44] uses a recursive technique to approximate the Seeman - Horowicz nonlinear filter. He makes use of a linear filter with a simple time domain representation and which, except for very low frequencies, quickly converges to the Seeman-Horowicz filter.

Another method of wavefield separation is velocity filtering as described by Kanasewich [39], Yilmaz [43], Hardage [20] and Suprajitno and Greenhalgh [41]. Velocity filtering makes use of the property that upgoing and down going waves map into different quadrants in the F-K domain and hence can be separated. F-K filtering however requires correct amplitude balancing prior to operation as described by Hatton et al. [40], and the traces must be equally spaced. The optimal velocity filter as proposed by Seeman and Horowicz [42] on the other hand imposes no constraints on the trace separation but still requires true amplitude recovery prior to application.

Ideally, we hope to be left with VSP plots containing only the downgoing or the upgoing primary wavefield on which amplitude studies can be carried out. Furthermore, if multiples are present in a VSP section, then they require a different amplitude restoration than that applied to the primaries. In our work we assume that the current routines for seismic processing such as wavefield separation and deconvolution do a good job in providing us with a primary section of upgoing or downgoing energy. We will ignore the multiples and assume that they are sufficiently removed from the primary arrivals.

3.2.2 The multiplicative model of seismic amplitudes

Consider seismic energy recorded at a series of geophones in the borehole. VSP geophone receivers are typically sensitive to the particle velocity of the surrounding medium. For purposes of discussion it will be assumed that the three component VSP observations have been appropriately rotated such that the amplitudes are those observed in the direction along the ray path. Although beyond the scope of this thesis, it must be noted that this requires the medium be elastically isotropic as this condition is not necessarily true for anisotropic media. Following Clay [38], in such a situation the power density J (which is a measure of the wave's energy) is given by $J = \rho c v_r^2 = I v_r^2$ where v_r is the particle velocity, which hereafter is taken to be the amplitude, and I=ρc is the local acoustic impedance of the layer where the geophone sits. Then, from the discussions in Section 2.2, the amplitude of vibration recorded by the geophone can be written as:

$$A(G) = A(S) * DE * GE * TE * FE * IE * RE$$

where

A(G) = Amplitude of vibration recorded at the geophone

A(S) = Amplitude of vibration generated by the source

DE = Directivity effect as the source does not generate energy uniformly in all directions. Assumed constant here.

GE = Geometrical effect as the energy spreads out over a wavefront of increasing spread and as complicated by the geologic structure.

TE = Transmission effect due to loss of energy from the direct wavefield due to energy partitioning upon reflection and mode conversion.

FE = Frequency effect as the energy is selectively absorbed as it propagates in less than perfectly elastic media.

IE = Impedance effect as the geophones are in media with different acoustic impedances, they will respond differently to an equal amount of energy.

RE = Reflectivity effect which depends upon the reflector of interest. Finally obtaining the value of this parameter such that it might be employed in analyses of rock properties (AVO response) is the primary goal of this work.

In formulating the above expression for the amplitude recorded by a geophone we have assumed, and hence neglected, that the geophone coupling and response is constant from one recording position to another. If we further assume that the source amplitude is also constant and directivity effects negligible, and we derive compensating factors for the remaining four effects, then the remaining amplitude becomes a function solely of the reflectivity of the interface of interest.

3.2.3 Traditional amplitude restoration curves

In the day to day amplitude restoration as practiced in industry, the amplitude along a trace is restored by applying a gain function of the form $g(t) = t^n$ to each trace. This idea is based on the hypothesis that as the distance along the raypath and hence

the time of arrival increases, the amplitude decays proportionally due to geometrical spreading. The idea is approximately valid for surface reflection seismic profiling where the upgoing and downgoing paths of a ray are approximately equal. A rule of thumb applied in Alberta, for example, is that n=1.7 as this, subjectively, appears to equalize the gain of reflections with depth.

This 'rule of thumb' is applied to VSP data even when the objective is to study the variation of amplitude with offset. This is unfortunate as this idea is very simplistic and it does not take into account the refraction of rays at interfaces (which could cause a convergence effect if the second medium has a lower velocity) nor any of the other effects listed in the multiplicative model above. Despite these enormous limitations practitioners continue to carry out AVO studies after applying this simplistic correction.

To better illustrate the deleterious effects of this empirical correction, reconsider the model described in Table 3.5. For an offset of 30m, the uncorrected amplitude of the event from the interface at 3000m depth is given in Figure 3.19. Note that in this and all the other plots which follow, the data is normalized with respect to the maximum value (which in this case occurs at the deeper geophone). The decay in amplitude with decreasing geophone depth is due to geometrical and transmission effects as given by Figure 3.20 and Figure 3.21 respectively. These were calculated in MASTER.M (Section 3.1.3) using the Gel'chinsky method and the Zoeppritz equations for the geometrical effects and the transmission effects respectively. In our computation of the transmission effects we used displacement amplitudes such that the acoustic impedance effect becomes assimilated in our computation of the transmission effects. Hence multiplying the geometric effect and transmission effect curves takes care of our three major amplitude effect mechanisms. Furthermore the characteristic jumps seen in Figure 3.21 and hence Figure 3.19 are the sudden jumps in amplitude across each interface. The major contributor to these amplitude discontinuities is the acoustic impedance effect. On the other hand the geometric effects curve of Figure 3.20 is smooth even though refraction at interfaces changes the cross sectional area of the ray tube.

As the offset is small compared to the interface depth, all the rays hit the horizontal reflector at almost normal incidence. The variation of the reflected energy with

incidence angle is minimal (less than 0.002 %) and we expect to measure essentially a constant amplitude across the receivers at all depths (Figure 3.22). In contrast, if we take the synthetic traces generated and apply a $t^{1.7}$ gain function, the restored amplitude is as shown in Figure 3.23. The decay in amplitude with increasing geophone depth is due to the fact that the amplitudes at the shallower geophones are over compensated since the arrival time t and hence t^n is large. This can somewhat be minimized by choosing a smaller n value. Figure 3.24 shows the amplitude after applying a gain function with $n = 0.6$.

Figures 3.25 to 3.28 are a similar sequence of amplitude effects for the case of a source offset of 1500m from the well head. Here variation in amplitude with angle is expected to be more significant due to the larger range of incidence angles. This is seen in Figure 3.29 which gives the theoretical amplitude values as determined by the Zoeppritz equations (Section 2.2.4) and in Figure 3.27 which shows the transmission coefficients as a function of geophone depth. In contrast to Figure 3.21 for the zero offset case, the transmission coefficients in Figure 3.27 differ for geophones in the same layer decreasing with the geophone depth and the angle of incidence on the reflector.

3.2.4 The Acoustic Impedance Effect

One major and characteristic difference between VSPs and surface seismic experiments is that in VSP experiments receivers are located in a borehole. Hence, receivers at different depths are placed in rock whose acoustic impedance differs. This impedance effect can be substantial and cannot be ignored. Such extreme differences are generally not encountered in surface seismic experiments except in cases when there are rapid changes in the compressibility of the surface material from a road to a field.

From Section 2.1.1, power J is related to amplitude A through

$$J = IA^2$$

where I is the acoustic impedance of the medium. Hence the same energy yields different particle velocities depending on the acoustic impedance of the local medium. The greater the acoustic impedance of the medium the smaller the amplitude, and

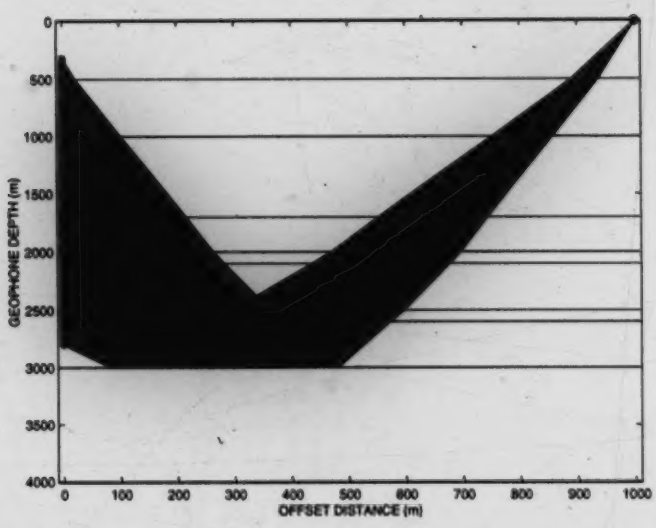

Figure 3.18: Ray diagram for zero offset reflections from interface No. 8 as defined in Table 3.5.

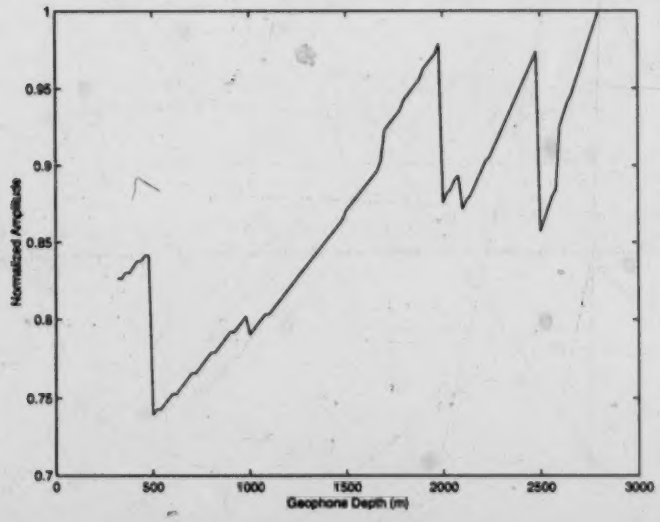

Figure 3.19: Observed particle velocity amplitudes for the upward traveling reflection from the 3000 m deep interface of Table 3.5. The source offset is 30 m.

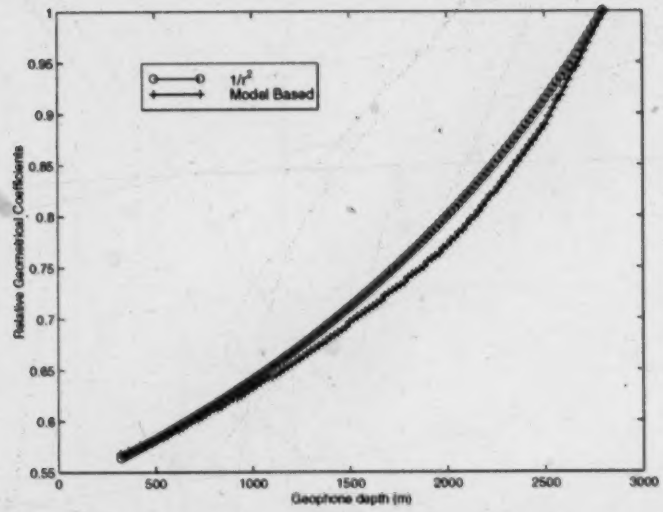

Figure 3.20: Geometrical spreading effects for the reflection from the interface at 3000 m as given in Table 3.5. The source offset is 30 m.

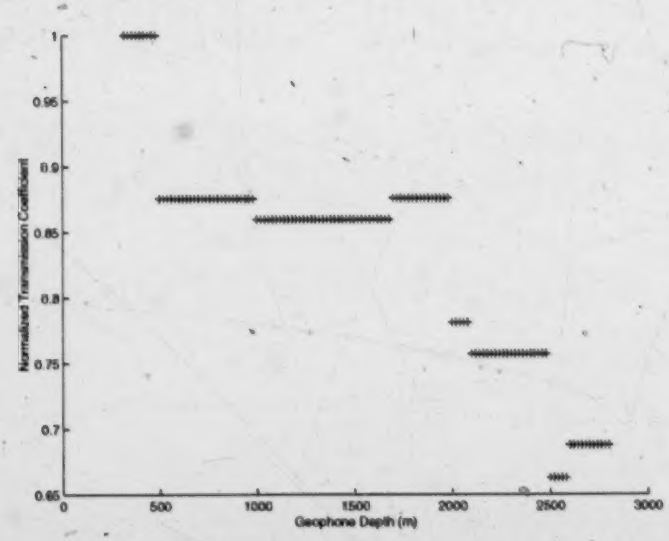

Figure 3.21: Cumulative transmission loss effects for a reflection from the interface at 3000 m as given in Table 3.5. This also retains the amplitude versus angle of incidence variations (AVA effect) and the acoustic impedance effect. The source offset is 30 m.

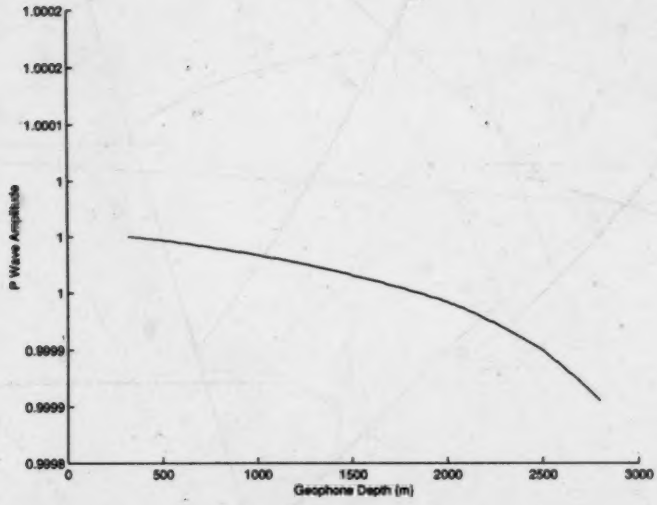

Figure 3.22: Expected amplitude due to angle of incidence variations only from the interface at 3000 m for an offset of 30 m.

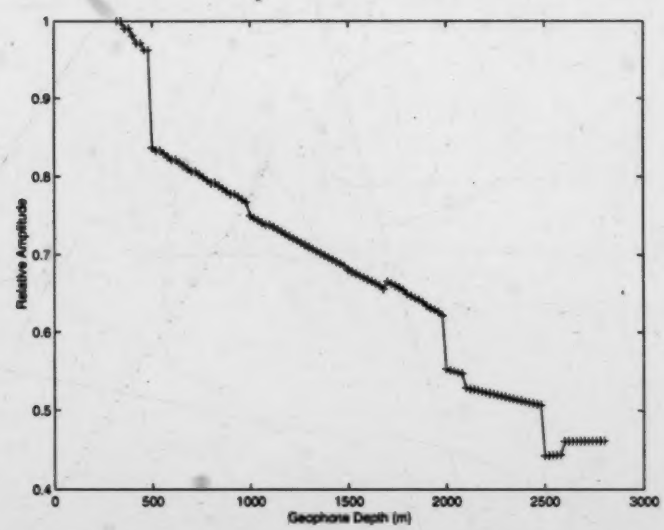

Figure 3.23: Observed particle velocity amplitudes from Figure 3.19 after application of the conventional 'empirical' t^n correction to each trace with n = 1.7

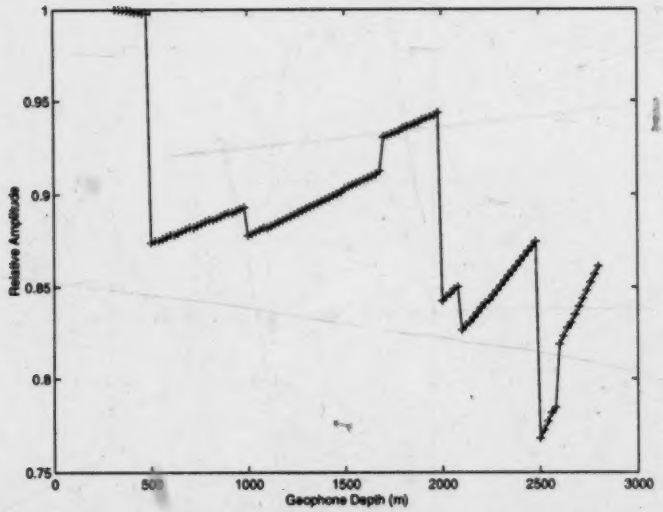

Figure 3.24: Observed particle velocity amplitudes from Figure 3.19 after application of a conventional t^n correction down each trace with n = 0.6.

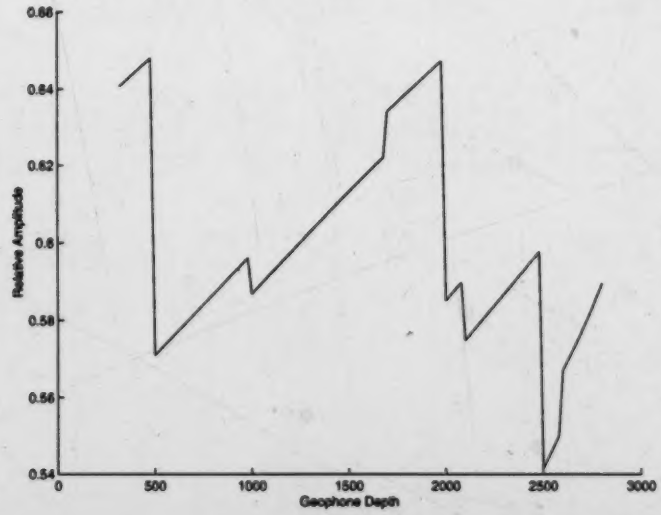

Figure 3.25: Observed particle velocity amplitudes for the upward traveling reflection from the 3000m deep interface of Table 3.5. The source offset is 1500m.

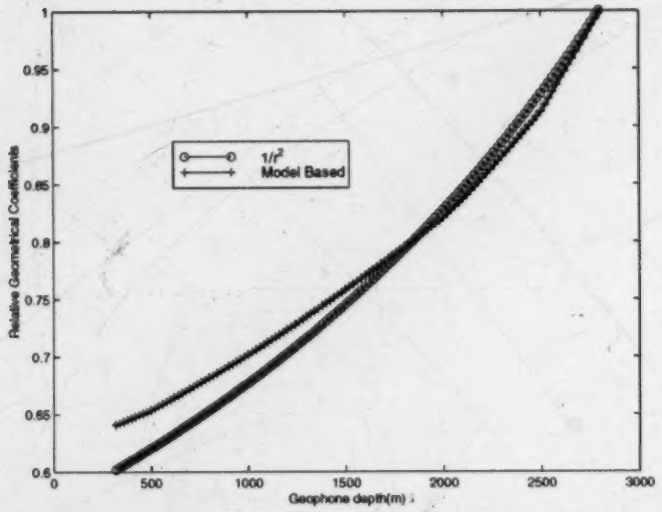

Figure 3.26: Geometrical spreading effects for the reflection from the interface at 3000m as given in Table 3.5. The source offset is 1500m.

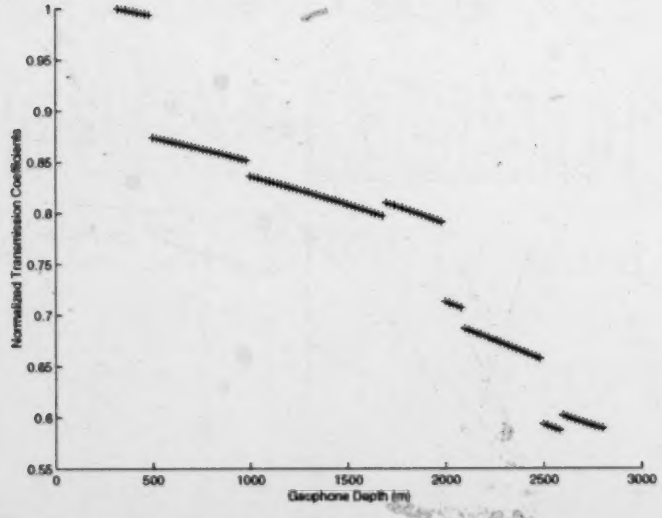

Figure 3.27: Cumulative transmission loss effects for a reflection from the interface at 3000m as given in Table 3.5. This also includes the AVA effect and the acoustic impedance effect. The source offset is 1500m.

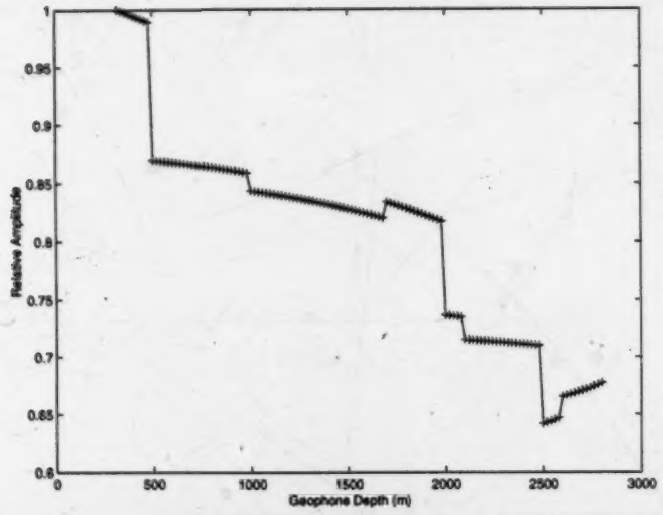

Figure 3.28: Observed particle velocity amplitudes from Figure 3.25 after application of a conventional t^n correction down each trace for n=0.6.

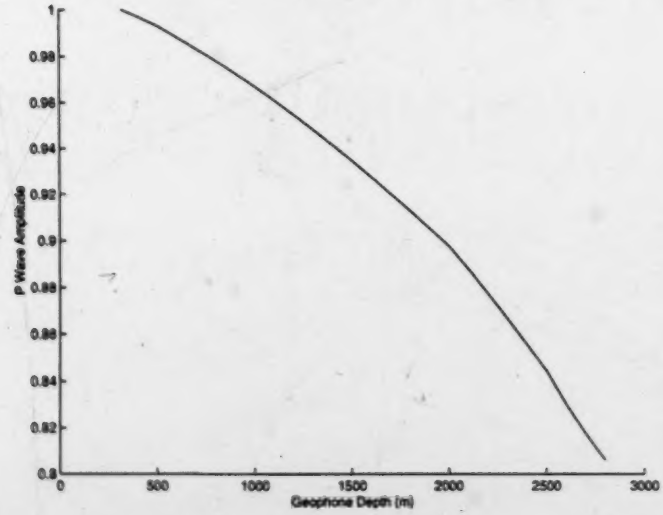

Figure 3.29: Expected amplitude of reflection from the interface at 3000m for a source offset of 1500m.

vice versa. Hence if we want to be able to extract lithologic information about the interface of interest we need also to correct for this acoustic impedance effect.

3.3 Summary

Since it's introduction in the 1960's the VSP has gained popularity and has been established as a complementary method to surface seismic in obtaining information about the subsurface. Similar to surface seismic, VSPs contain both dynamic and kinematic information. The kinematic properties of the VSP are well known , however the dynamic information is more complex and therefore harder to interpret.

To better understand amplitudes, we generate synthetic VSPs by ray tracing through various geophysical models. The model is composed of parallel homogeneous and isotropic layers and characterized by the interface depths, P and S wave velocities and densities. In future work this model could be made more sophisticated and realistic by the inclusion of dipping layers, absorption and anisotropy. Through various simple illustrative examples we have seen how a geological structure translates into a VSP plot. Ray path coverage can be inhomogeneous resulting in non linear and discontinuous transit times.

In formulating the amplitude of our events, we have assumed that there are three main amplitude influencing mechanisms. These are the geometrical effects, the transmission effects, and the acoustic impedance effect. Other effects such as frequency selective absorption and source directivity are assumed to be of second order and are here neglected. Furthermore we also assume that any processing steps such as wavefield separation properly preserve amplitudes. Amplitude behavior in a VSP is studied through the model described in Table 3.5. One striking feature in the amplitude of the reflected event at 3000m depth, is its discontinuous nature. This is due to a combination of the transmission and acoustic impedance effects. Application of a continuous t^n correction fails to restore the synthetically generated amplitudes to the theoretically expected amplitudes as predicted from the Zoeppritz equations.

Chapter 4

Amplitude correction of a real data set

4.1 Data Characteristics

4.1.1 Geological Background

In this Chapter we will be applying the model based amplitude correction technique to a real VSP data set. Our objective is to see how good a job we can do in correcting the amplitude under carefully controlled conditions.

The VSP to be corrected was acquired at the Underground Test Facility (UTF) in Northeastern Alberta (Figure 4.1) where viscous heavy oils are being produced from shallow bituminous Athabasca oil sands of the Lower Cretaceous McMurray Formation (Schmitt [54]). Figure 4.2 shows the stratigraphy at the UTF. The geology of the area is well documented by Wrightman et al. [55] [56], but for our purposes it is sufficient to follow the concise summary as found in Chalaturnyk [53]. The McMurray reservoir lies on top of the Devonian Waterways formation which consists of alternating layers of argillaceous, nodular and massive limestone units and which is occasionally weathered at the unconformity surface. The oil sands-limestone contact is generally very well defined with the main pay of reservoir reaching a thickness of around 23m. Several shaley zones are interbedded in the bottom few meters of the pay zone. Overlying the McMurray formation is 2m of water and gas saturated Wabiskaw sand, a member of the Clearwater formation. Clearwater Formation Shales constitute the next 75m of overburden, followed by 30m of sandy shales of the Grand Rapids formation and by 15 to 20m of till, sand and gravel, and glaciolacustrine clays.

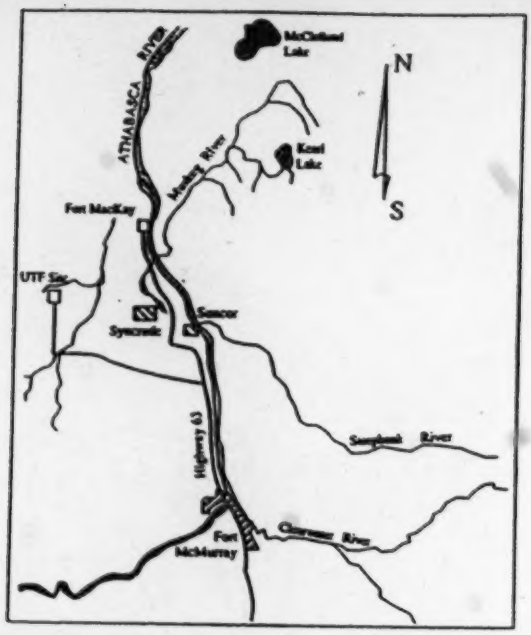

Figure 4.1: Location of the Underground Test Facility (From Chalturnyk [53]).

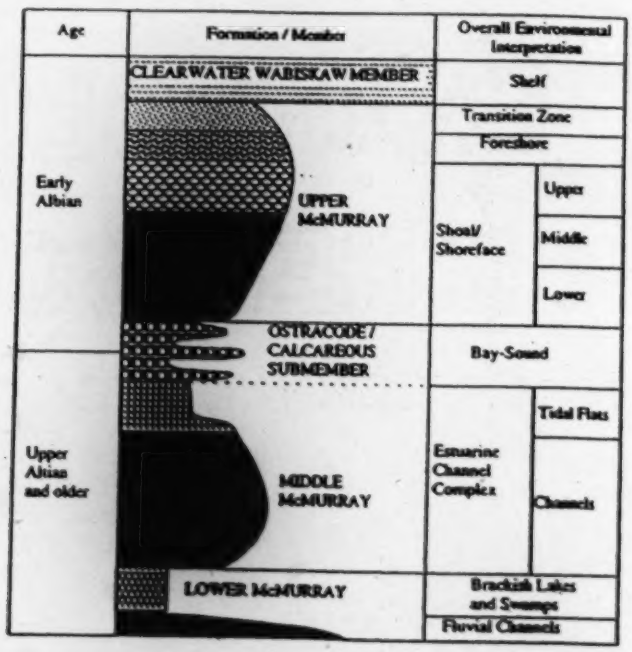

Figure 4.2: Stratigraphy at the UTF site (From Chalturnyk [53]).

4.1.2 Acquisition Parameters

Seismic energy was generated using a Betsy Gun at an offset of 10m from the well head. Data was recorded using an SIE 3 component wall locking geophone package from 30 m to 220 m depth in the UTF BC-6 observation well for a total of 77 traces. Each trace is 500 ms long at a sampling rate of 0.1 ms per sample. Several shots were recorded at each depth and then the traces stacked and scaled appropriately to give a single trace. A surface geophone close to the well head was used for quality control and to check consistency of the source. Together with the very good repeatability of the source, this resulted in high quality records (Schmitt and Sacchi, 1998, in preparation).

Together with the three component VSP, an open hole sonic log was also recorded at 10 cm depth intervals. Figure 4.3 shows the sonic velocity as a function of depth and Figure 4.4 shows the raw data before any processing. The largest amplitude events observed in Figure 4.4 are the direct arrival energy, the tube waves (Hardage [20]) which zig zag across the section and some surface wave energy at around 200 ms on the shallower geophones. Both the tube and the surface waves are considered to be noise which can be attenuated through processing. As a first step we will attempt to restore the amplitudes of the downgoing primaries. Since this event is the first to arrive, it is not as influenced by later energy noise and we are justified in using this raw data.

The sonic log in Figure 4.3 may be divided into three sections. The most obvious section is from a depth of 160 to 220 m and corresponds to the high velocity carbonates. Because of the sharp jump in velocity and density with respect to the overlying oil reservoir, the interface between these carbonates and the oil sands constitutes a strong reflector which partially explains the sudden decrease in amplitude of the direct arrival energy at receiver 53 in Figure 4.4. Some amplitude change is due to the acoustic impedance effect as described in Section 3.2.4. On top of the carbonates, at a lower velocity is the oil reservoir from a depth of 125 to 160m. Just above the oil reservoir from a depth of 120 to 122 m, is a thin layer of gas sands with an anomalously low velocity. Marine silts and shales with high velocity interbedding layers overlay the gas sand. Figure 4.5 shows a variable area wiggle plot of the raw

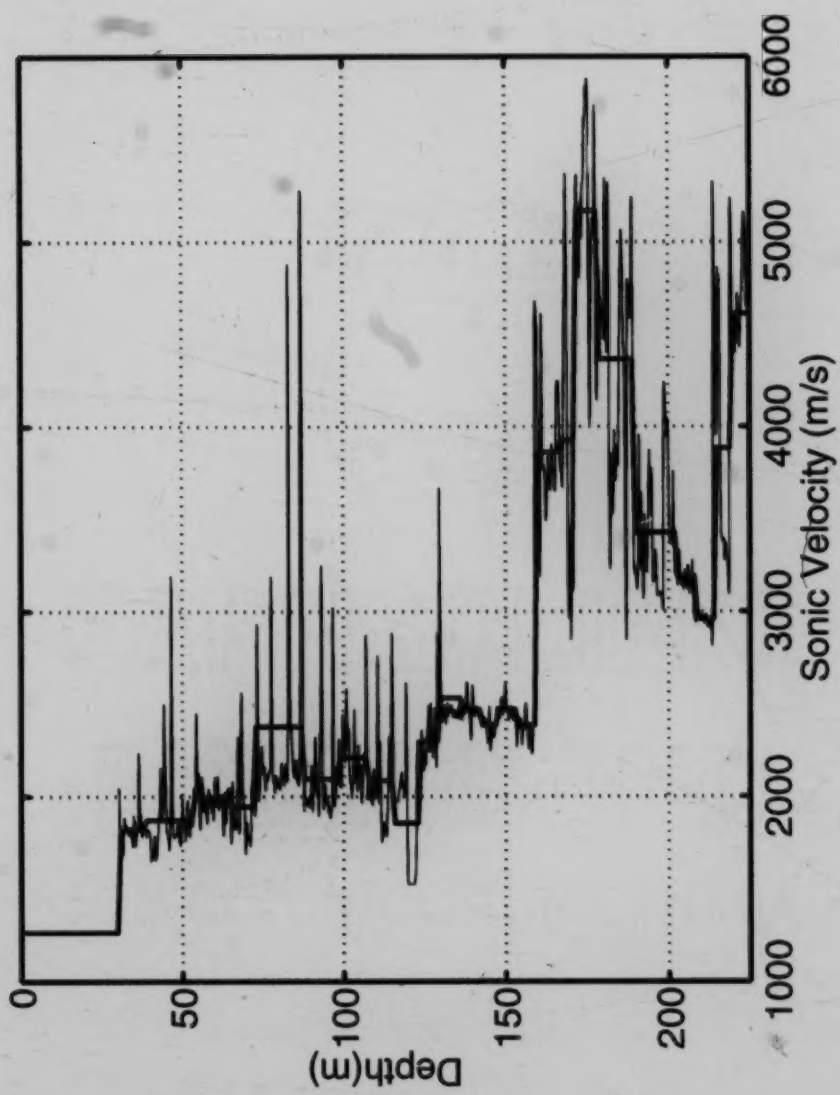

Figure 4.3: Sonic Log for the observation well. The thin line represents the complete log whereas the thick line is a blocked version of the complete log.

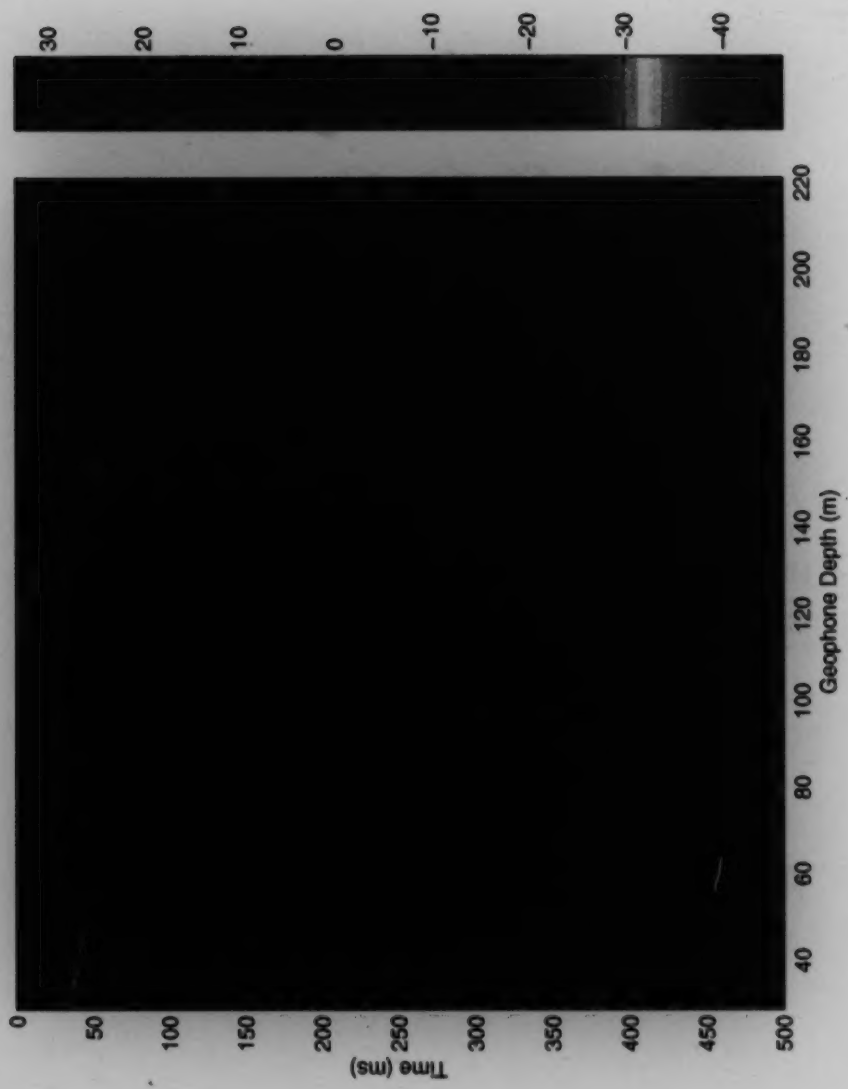

Figure 4.4: Raw data set. Colorbar denotes amplitude.

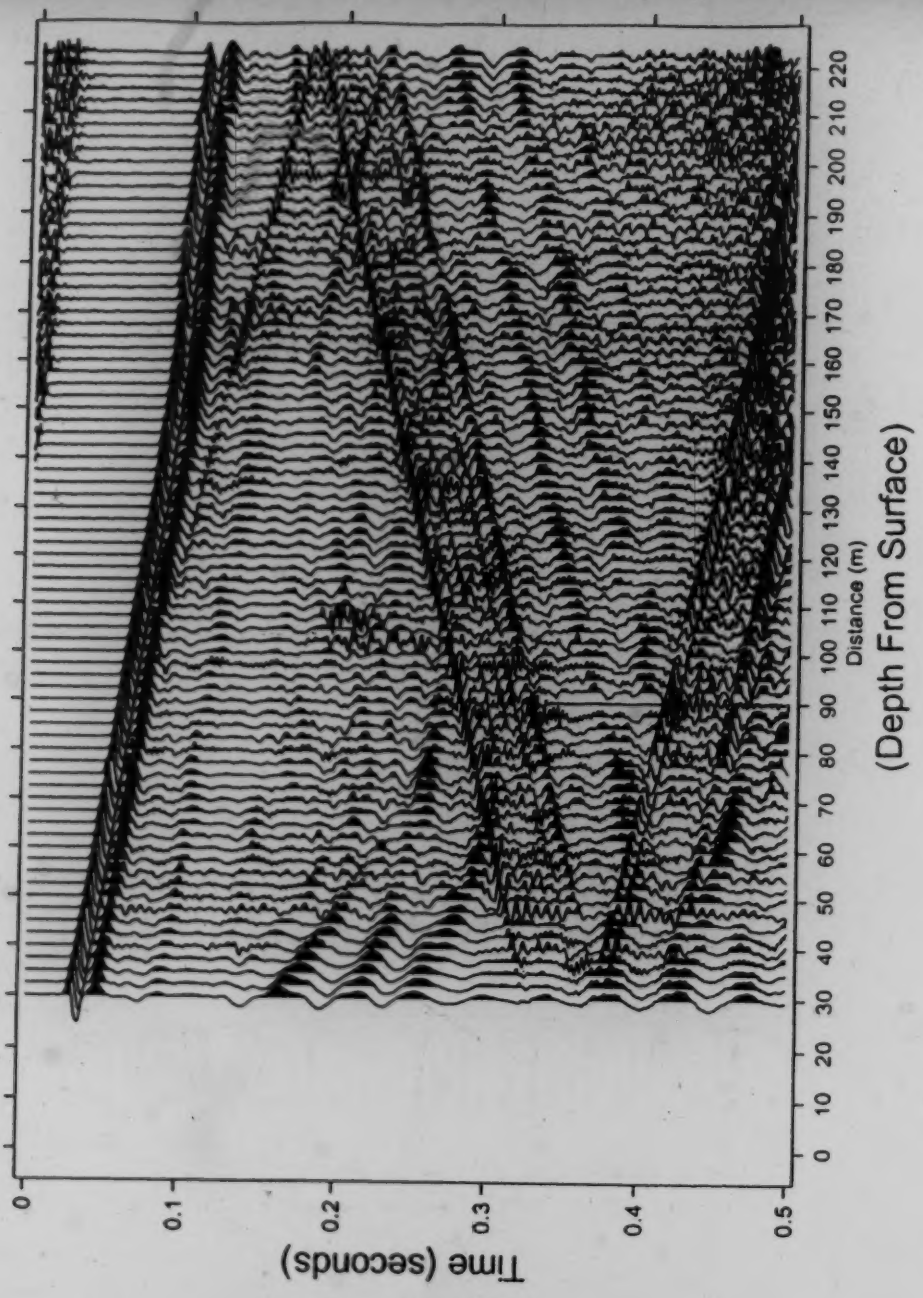

Figure 4.5: Wiggle plot or raw data set after the application of AGC (Automatic Gain Control) to boost later energy

data after the application of AGC or Automatic Gain Control. This involves the multiplication of a particular sample by a gaining factor derived from a window of data about the sample (Hatton et al. [40]) and is very useful in boosting up later events for display purposes.

4.2 Restoring the Primary Amplitude

4.2.1 Generating the model

The first step in applying our model based amplitude correction technique is to generate the model upon which the correction curves will be generated. This is usually accomplished using the sonic logs which provide a closely spaced measure of interval velocities along the well. As the sonic logs are very densely spaced (a sample every 10 cm), they are often decimated and blocked. Blocking can be done automatically, by using a technique such as the Markov-Gauss algorithm [58], or manually by visually selecting the features of interest. In this work blocking was done automatically using proprietary software. Through this process a finite number of interfaces was chosen which defines the model.

To be able to compute amplitudes as well as travel time, S wave velocity and density for each layer in the model are also required. In this particular well, only a sonic P velocity log was present. No S wave and density logs were recorded and hence needed to be generated otherwise for the model to be complete. The density log was computed using Gardner's relation [57]. This is an empirical relation which states that in general the compressional velocity of a medium is related to the bulk density by

$$\rho = 0.23V^{0.25}.$$

The shear speed was calculated (e.g. Castagna et al [59]) from the compressional sonic speed under an assumption that Poisson's ratio is 0.29 along the sedimentary column. The many shortcomings of this relationship are recognized; it is derived from a simple curve fitting of a large data base and is subject to substantial discrepancy. However, as no other information were available, this relationship was employed. Since we are dealing with a zero offset or vertical VSP, the rays travel close to the normal to the interfaces; consequently the S wave speed plays a minor

role in determining transmission effects. Density information however, is still crucial in determining amplitude information. The resulting model is comprised of 27 layers and is listed in Table A.1. Figure 4.6 shows the blocked compressional velocity, shear velocity and density logs. As no sonic log data was available above the 30m depth mark, the compressional velocity was estimated from the direct arrival time of the first peak of the shallowest trace. This was found to be near $1265ms^{-1}$.

In order to obtain a better understanding of the modeling process, synthetics will be generated from two models. One is based on the complete log ie. every interface in the log was taken as a layer in the model; generating a model with 1972 layers, and the other is generated on a blocked version of the log for a total of 27 layers.

4.2.2 Calculating the correction curves

Once the models were generated, the synthetic VSPs and corresponding amplitudes were calculated using the ray tracing algorithms in MASTER.M. The first thing to compare between the synthetic and real data is the transit time of the events. Transit times for the real data were determined by picking the transit time of the first peak in the first arrival energy and then normalizing by the maximum value. These values were then compared to the computed transit time (Figure 4.7) to assess our confidence in the velocity model. Note that the transit time curves are very close for both the complete and blocked log models with a mean difference of 1%. Since transit time is solely dependent on velocity and geometry of the acquisition and model, obtaining a good fit of the transit time checks the validity of the kinematic properties of our model.

As seen in Figure 4.7, the transit times from the synthetic primaries match the ones picked from the real data well. An attempt to minimize the slight difference seen especially at the shallower geophones by iteratively changing the velocity of the first layer and recomputing the ray tracing. One must also keep in mind that the synthetic transit times are obtained from the sonic velocities which are at a much higher frequency than the seismic velocities. Hence dispersion or the variation of velocity with frequency is also be a source of error. The next step, and the goal of our work, is to determine the dynamic, or amplitude, properties.

Figures 4.8 and 4.9 show the amplitude decay due to geometric and trans-

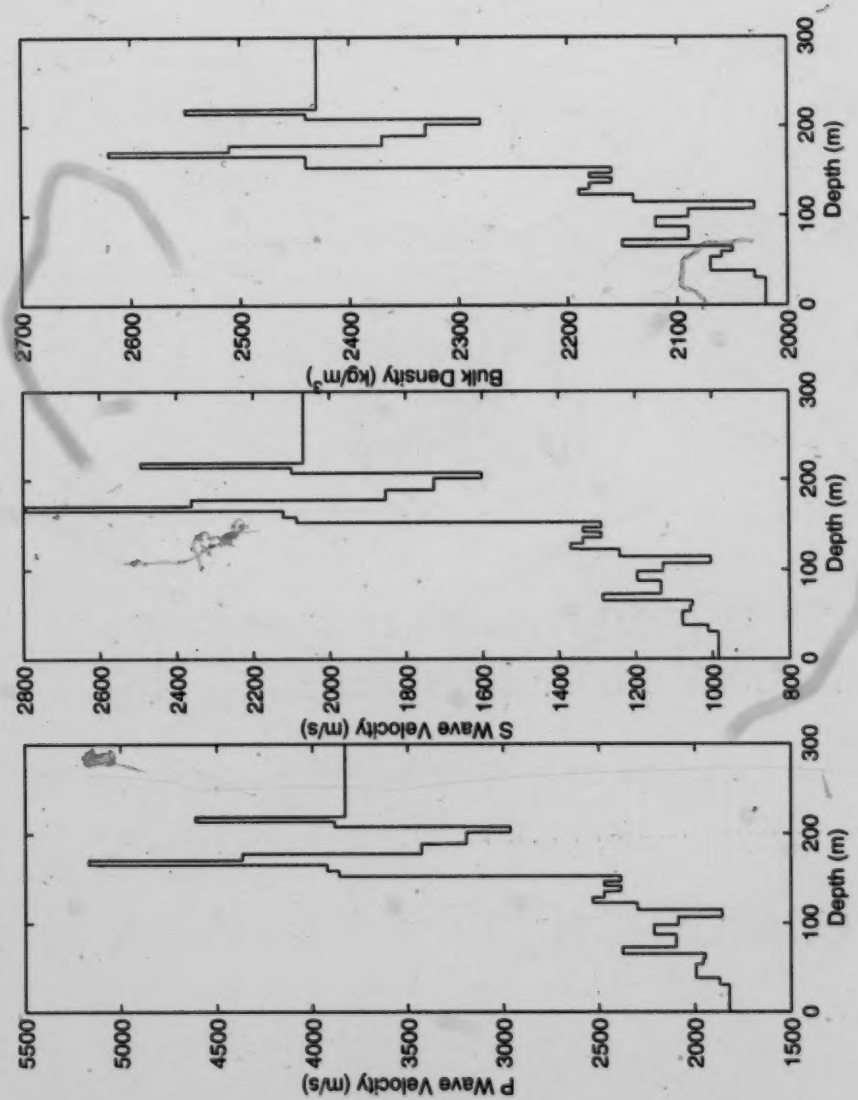

Figure 4.6: Blocked compressional, shear and density logs corresponding to the model in Table A.1

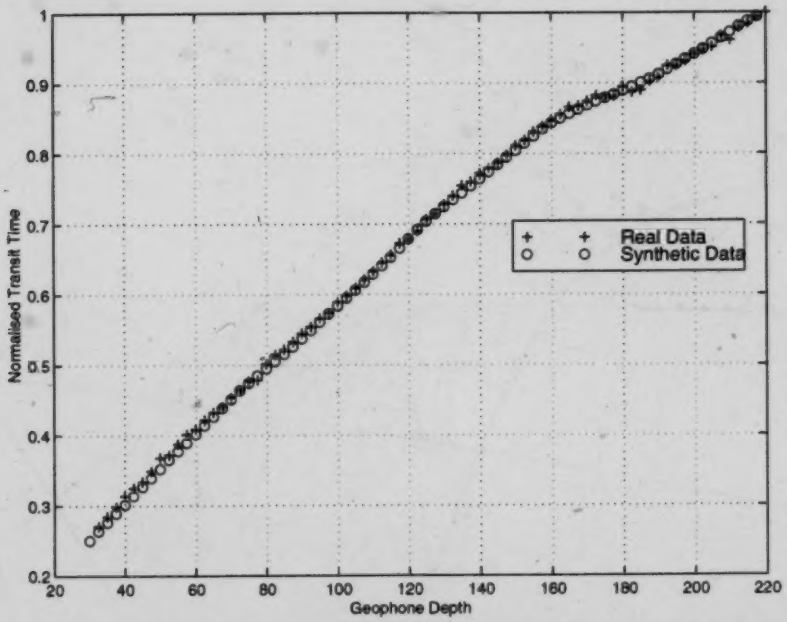

Figure 4.7: Transit times from the surfaec for the downgoing primary energy as determined for the synthetics as they compared to the picked times from the real data. Note that the transit time curves are nearly identical for both the complete and blocked log models.

mission effects, respectively. Both these figures include graphs for the amplitudes corresponding to the synthetics as derived from the complete and the blocked log models, respectively. Figure 4.8 shows that the geometric decay is nearly identical for both. This is expected as the geometrical coefficients depend on velocity and the transit time curves for the complete and blocked log models are identical (Figure 4.7). Figure 4.9 indicates that the general features such as the sudden jump at 160 m corresponding to the transition from the oil sands to the high velocity carbonates and to a lesser extent the jump at 80m corresponding to the transition from the marine silts and shales to the sand reservoir, are common for both models. However, the transmission effects for the complete log model are more substantial than that for the blocked log model. This is expected as the transmission effect is cumulative, the greater the number of interfaces and the stronger the acoustic impedance contrast across these interfaces, the more substantial the transmission effects. This will turn

out to be an important point later.

Once the geometrical effect and transmission effect curves have been computed the total amplitude effects are calculated by multiplying these two effects together. This was done and is illustrated in Figure 4.10 which shows the amplitude behavior as predicted from ray tracing through the two models. Figure 4.10 gives also the amplitude of the first maximum as picked from the real data (see next section for details). All three amplitude curves have been normalized by the value at the same depth level in order for the comparisons to make physical significance. Comparing the amplitudes as determined by the ray tracing we see that the amplitudes determined from the complete log fit the real data amplitudes better than those determined from the blocked log. The blocked log amplitudes as given by the green curve in Figure 4.10 show less decay than the real data. This discrepancy is attributed to not properly accounting for the transmission losses (Figure 4.9) when many of the interfaces are ignored. The synthetic amplitudes also replicate the sharp drop in amplitude seen on the real data at 150 m corresponding to the interface between the oil sands and the carbonates and at around 78 m corresponding to the transition from the marine silts and shales to the sand reservoir.

In looking at these amplitudes one must bear in mind the assumptions made throughout the course of this work. The most important is that we are assuming that the major amplitude effecting mechanisms are the geometrical, transmission and acoustic impedance effects. We are neglecting other effects such as frequency selective absorption and incoherent and coherent noise on the assumption that they are of second order for this shallow data. Furthermore, as we did in Section 3.2.3 in our computation of the transmission effects we used displacement amplitudes such that the acoustic impedance effect becomes assimilated in our computation of the transmission effects. Hence multiplying the geometric and transmission effect curves takes care of our three major amplitude effect mechanisms.

4.2.3 The direct arrival amplitude

As described in Section 2.1.1, theoretically the wave amplitude corresponds to the particle velocity of a harmonic wave oscillating at a single frequency. In practice however, the multi-frequency wave is contaminated by the effects of scattering and

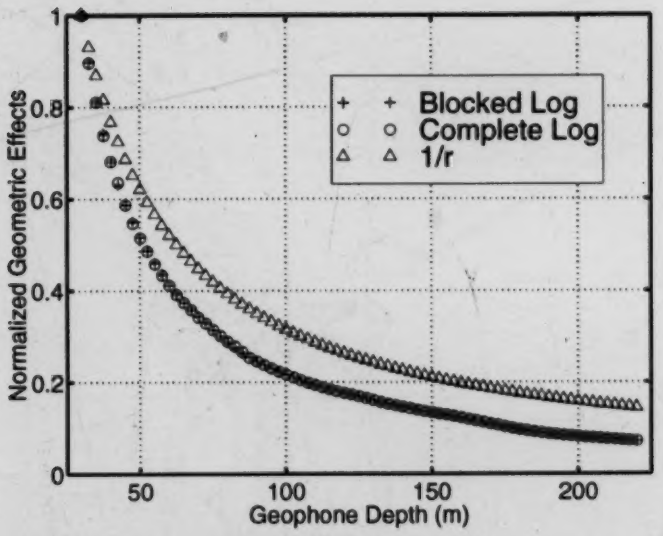

Figure 4.8: Geometrical effect amplitude decay relative to amplitude at 30m as obtained by ray tracing through the models. Green curve corresponds to blocked log, blue curve corresponds to complete sonic log (10 cm).

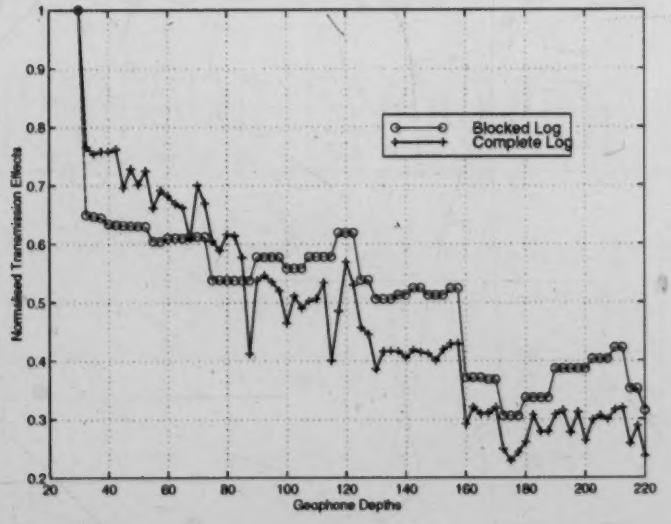

Figure 4.9: Transmission effect coefficients as obtained by ray tracing through the model. Green curve corresponds to blocked log, blue curve corresponds to complete log.

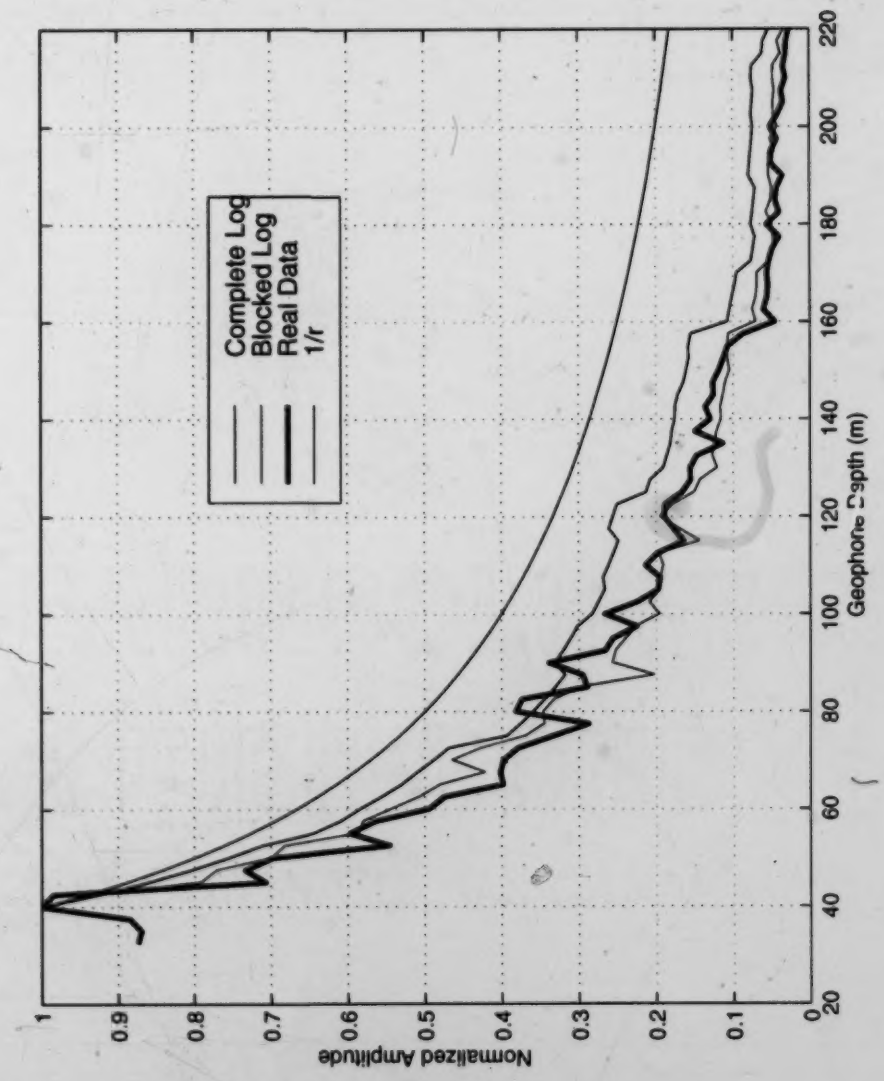

Figure 4.10: Amplitude for the downgoing primary energy as determined by ray-tracing through the models. Red curve shows the amplitude as picked from the real data.

modified by attenuation and dispersion. Thus, it is not necessarily trivial to decide what feature of the seismogram corresponds to our theoretical amplitude. Hence several measures, or attributes, are made in the hope of relating them to the wave intensity. By assuming that the waveform is stationary and isolated, we expect these attributes to be linearly related to the square root of the wave intensity. The attributes used in this study are the values of :

a) the amplitude of the first maxima

b) the amplitude of the later and larger first minima

c) the amplitude of the first peak of the amplitude envelope

d) the mean absolute amplitude over a window

e) the root-mean-square amplitude over a window

f) the square root of the sum of the squared amplitude over a window

The amplitude of the first maxima and first minima was picked semi automatically in Matlab as the value of the first peak and following trough. The amplitude envelope (Taner et al. [60]) was also derived semi automatically in Matlab using the Hilbert transform. Boundaries for the window for the last three attributes was defined as the first break and the third zero crossing respectively. The first break was picked automatically using a cross correlation based picking procedure (Molyneux and Schmitt [61]).

All six attributes are plotted in Figure 4.11. Figure 4.12 shows the same attributes but using a semi log plot. As expected the amplitudes decays rapidly with increasing geophone depth mostly from geometrical spreading. Another interesting feature to note is the discontinuities in the amplitude corresponding to sudden acoustic impedance changes of the lithology. In particular , notice the jump immediately below 160 m corresponding to the interface between the oil sands and the carbonates. This drastic change is also seen on the sonic and the blocked logs corresponding to the model in Table A.1 (Figure 4.3).

4.2.4 Applying the correction curves

Before we apply the correction curves derived in Section 4.2.2 we need to correct the data amplitudes for the fact that the source is offset 10m from the well bore. The exact directivity pattern of the source is unknown, but given that the source consists

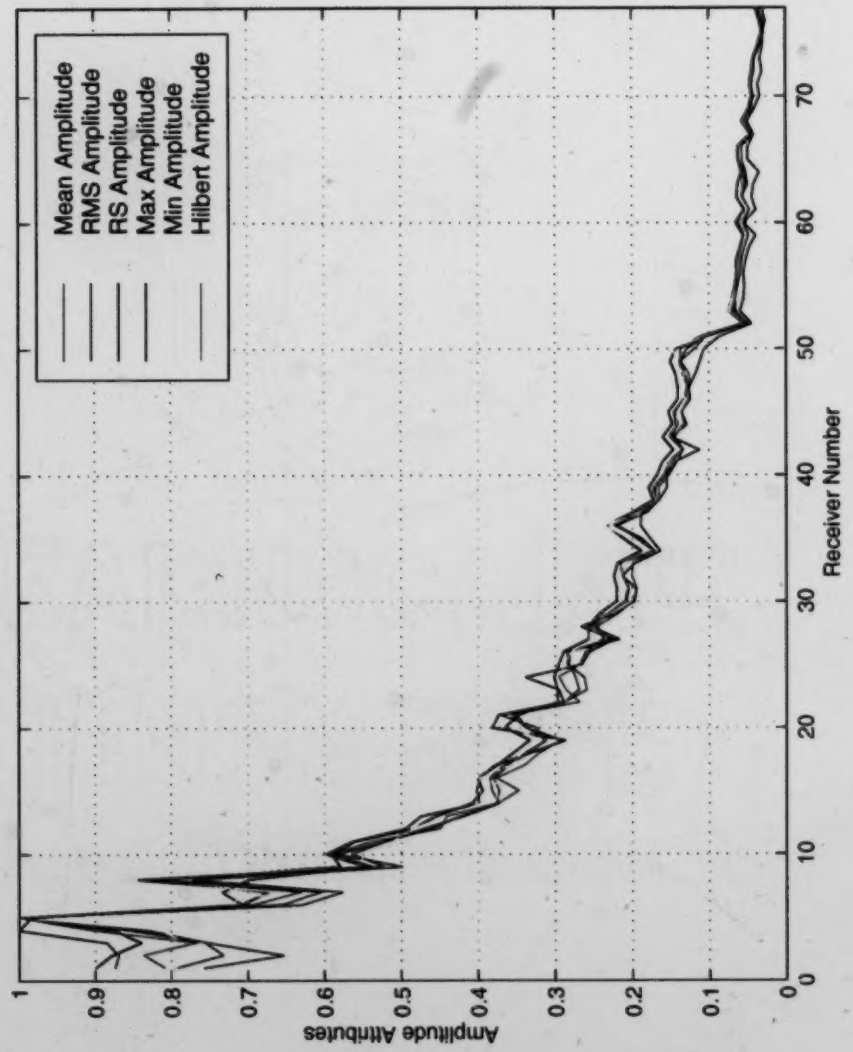

Figure 4.11: Amplitude attributes against receiver number.

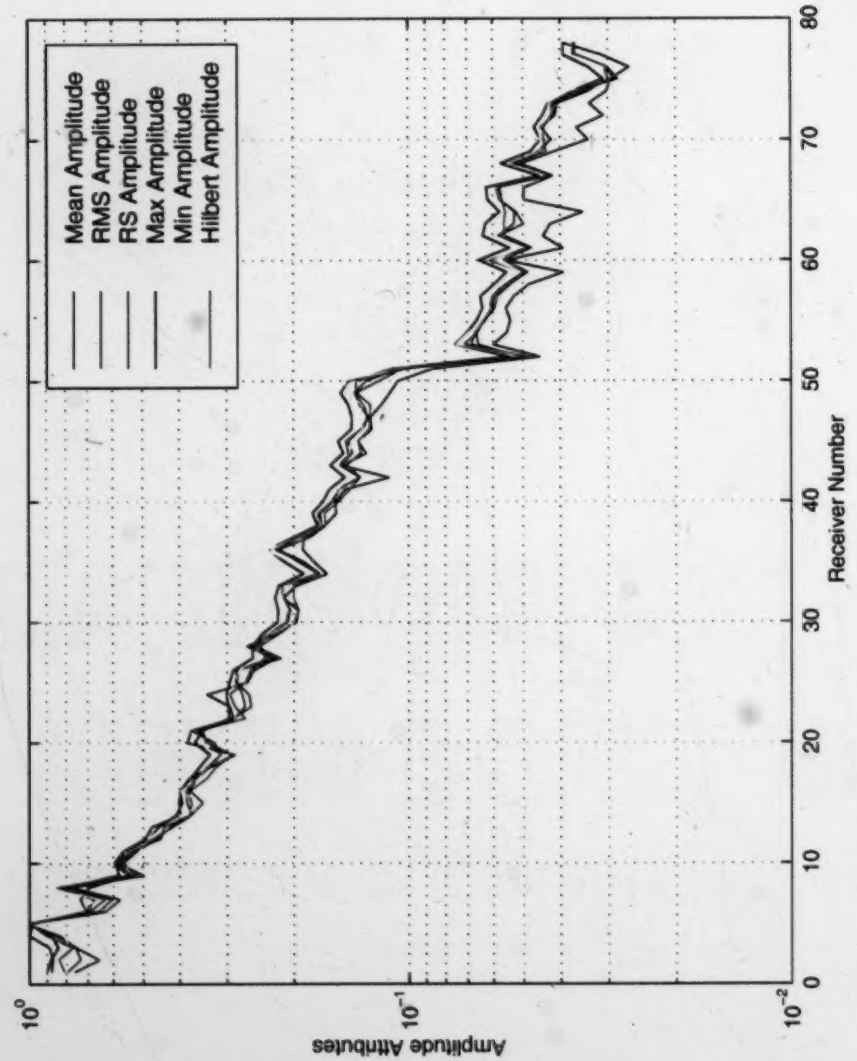

Figure 4.12: Amplitude attributes against receiver number on a semilog graph.

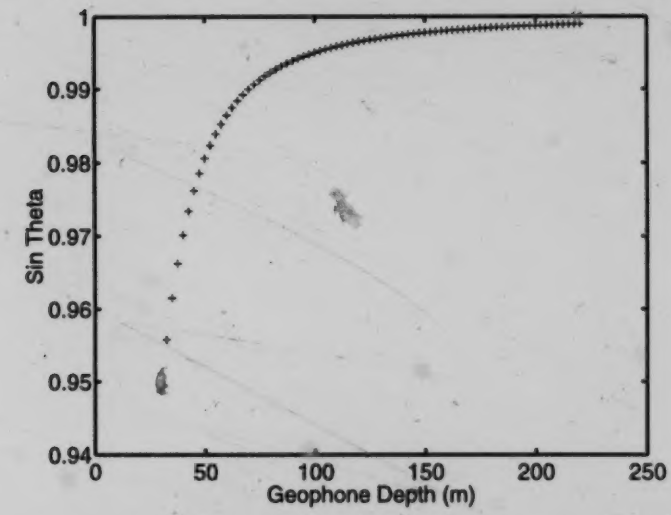

Figure 4.13: First order amplitude change on the vertical component due to variation in the geometry between the source and receivers on increasing depth.

of a water filled hole immediately at the surface and that the impact of the slug mimics an explosion within the water, we shall assume the source is undisturbed. However, the three component geophones are not aligned with the incoming ray paths. To a first approximation, for a vertically sensitive geophone, we can assume a simple correction for this misalignment of the form :

$$\frac{depth}{\sqrt{10^2 + depth^2}}$$

where depth is the geophone depth. It was felt that this correction would introduce less error than a complete polarization analysis of the three components.

Figure 4.13 shows the variance in Sinθ with geophone depth, where θ is the angle made with the horizontal by a straight line from the source to the receiver. The attributes derived in the previous section are divided by the above ratio to correct for this detector misalignment. The difference is hardly noticeable as seen in Figure 4.14.

Once the synthetic amplitudes have been computed and the amplitude attributes corrected for source directivity effects, the next step is to attempt to restore the amplitudes of the real data by dividing them with the synthetically derived amplitudes.

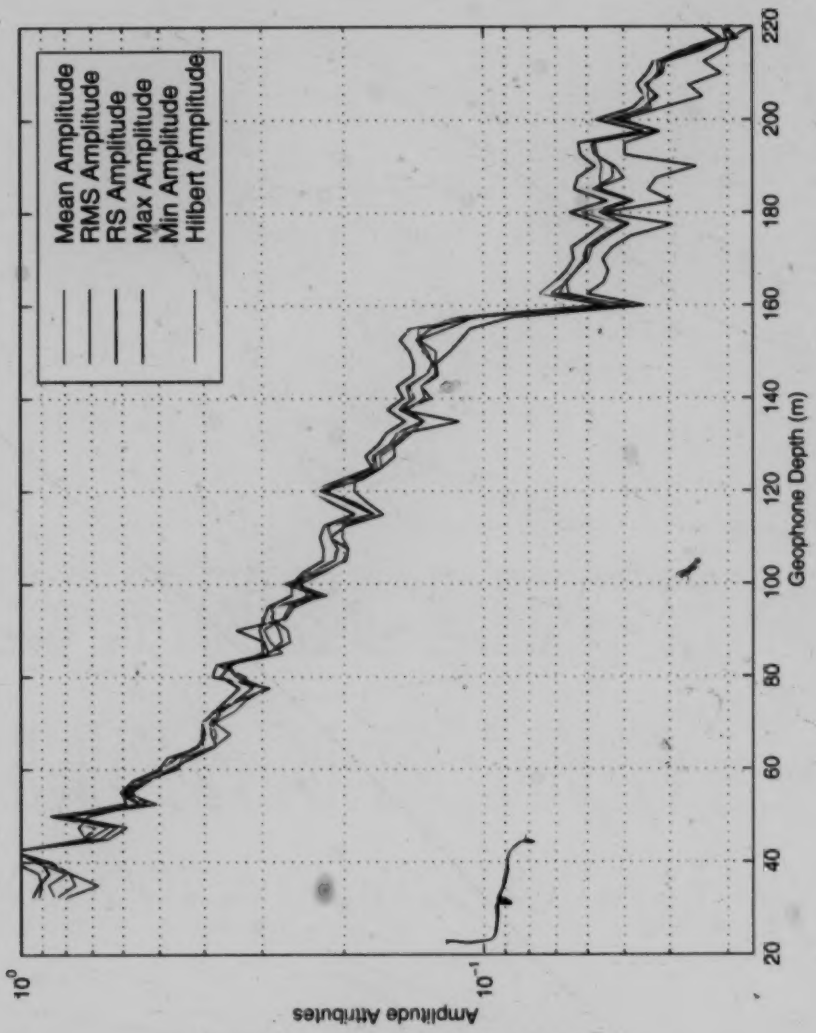

Figure 4.14: Amplitude attributes against geophone depth on a semilog graph after correcting for source directivity. Hardly any difference can be observed from Figure 4.12.

As these amplitudes are from a zero offset or vertical VSP, we expect that after correcting for the major amplitude influencing mechanisms, we will obtain an ideally constant corrected amplitude with receiver depth. Figure 4.15 shows the result of attempting to restore the direct arrival amplitude attributes using the correction curve as derived from the complete log. Of course, this curve was chosen since as shown in Figure 4.10 it better fits the real amplitudes. In order to have a better feel for the general trend in Figure 4.15, a moving average of five data points in length was taken. The resulting smoothed curves are shown in Figure 4.16.

Looking beyond the high frequency scatter in Figure 4.16 one can see that the corrected amplitude is more constant than in Figure 4.11 where it decays by a factor of about 95%. However the curve in Figure 4.16 seems to be divided into three major distinctive regions : 20 to 80m, 80 to 160m and 160 to 220m. Moreover these regions are strikingly similar in depth to the three main geological sections as outlined from the sonic log in Figure 4.3. Of course, this feature in the restored amplitude curve arises from the fact that the amplitude above 160m and below 80m of the synthetic amplitude curve is greater in magnitude than the real data amplitude. Hence when the real data amplitude is divided by the model based amplitude, the restored curve exhibits the behavior seen in Figure 4.15.

Possible justifications for this effect may be found in the assumptions that we made in computing our correction curves. For instance, we have neglected any amplitude loss due to frequency selective absorption. Even though this effect might not be as insignificant as we have assumed, we would expect it to contribute to a monotonic decrease in amplitude with geophone depth (Figure 4.17). However, this does not explain the zoning effect seen in Figure 4.15.

A more plausible explanation can lie in the density values we put in our model. As no density log is available the density values of our model were determined from Gardner's relation [57]. This approach can introduce some uncertainty as Gardner's relationship is only a general empirical relationship which can only approximate the real density properties of our rocks. Moreover the density values obtained from Gardner's relationship are directly dependent on the sonic velocities which in turn might be different from the seismic velocities due to dispersion.

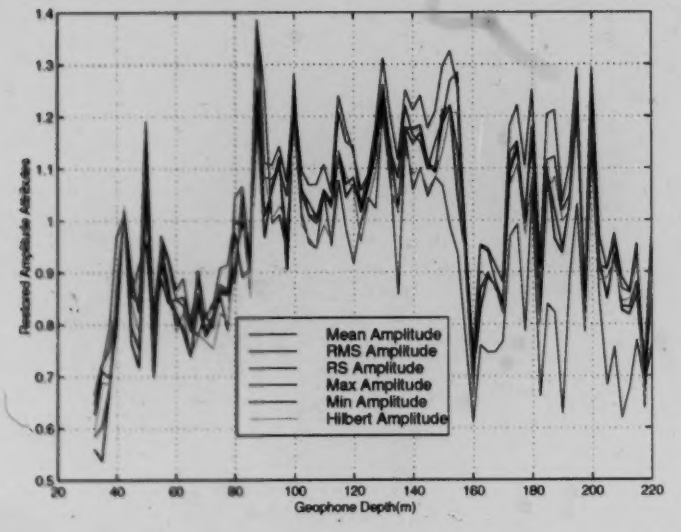

Figure 4.15: Amplitude attributes after applying model based amplitude correction.

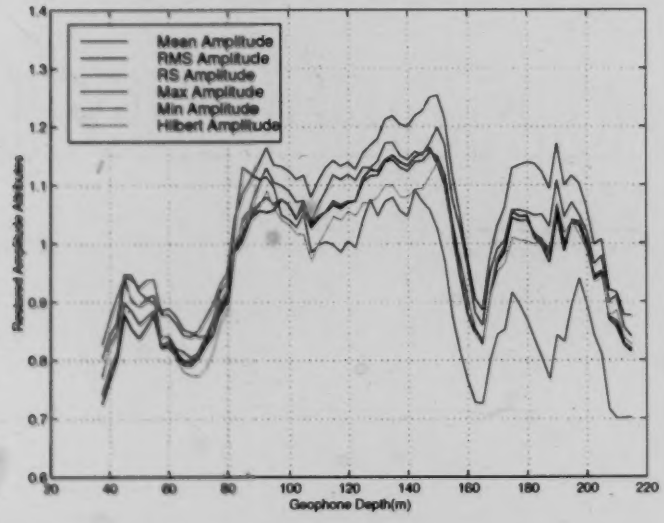

Figure 4.16: Amplitude attributes from Figure 4.15 after appyling a moving average filter.

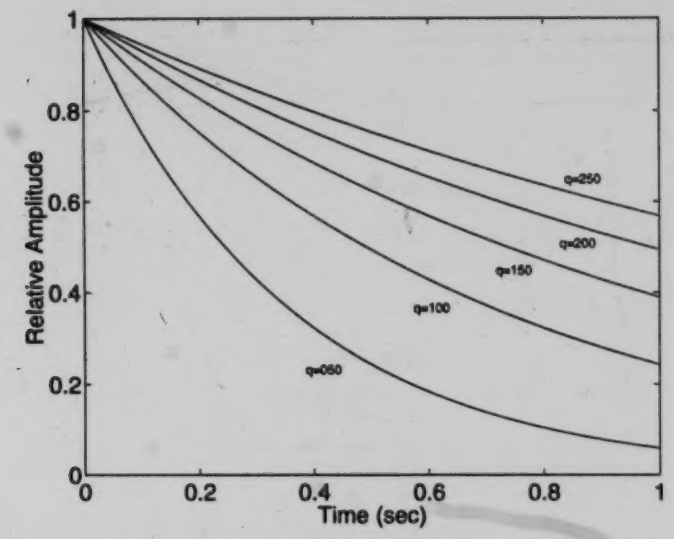

Figure 4.17: Relative amplitude loss for different values of Q for a frequency of 45Hz.

4.3 Summary

In this chapter we have a closer look at the amplitudes of the direct arrival energy of a shallow, closely spaced, zero offset VSP. This VSP was acquired under well controlled conditions so we expect consistency in source strength and receiver coupling resulting in truer optimal amplitudes. The major feature in this VSP is the sharp transition from the oil sands to the high velocity carbonates at a depth of 160m. This interface acts as a strong reflector resulting in an abrupt decrease in the direct arrival amplitude as seen in Figure 4.4.

Two models were generated both based on the sonic log that was acquired in the same well. The first model of 27 layers was generated from a blocked version of the log and the second model included all the layers described in the log. As no density log was available, density estimates were obtained from Gardner's relationship. The shear speed was also estimated from the sonic by assuming a Poisson's ratio of 0.29 along the sedimentary column. Direct arrival amplitudes were then calculated by ray tracing through the models taking into account the effects of geometrical spreading, acoustic impedance and transmission. For both models, the transit times obtained

from the synthetics agreed very well with the real data thus increasing our confidence in the velocity model. The agreement in both velocity models is also confirmed by the geometrical decay curves which are practically identical. Both these curves show substantially more decay due to geometrical effects than a simplistic $1/r$ curve. On the other hand, whilst the transmission curves obtained from the two models are similar in some of their major characteristics, taking more layers into the model contributes to more amplitude loss.

As it is not simple to decide what feature of a seismic wavelet or trace corresponds to the amplitude as defined in Chapter 2, six different amplitude attributes of the direct arrival wavelet were taken. These amplitude attributes give similar relative values indicating consistency in our measurements. A comparison of the amplitude of the first peak with the amplitude as determined from the synthetics shows good agreement especially with the curve obtained from the model comprising all the layers in the log. The blocked log model amplitudes experience less decay than the real data.

After correcting the real data amplitude attributes for source directivity effects, an attempt is made to restore these amplitudes to the theoretically expected value by diving with the amplitude curve as obtained from the synthetic. Since our amplitudes are from a nearly zero offset VSP we expect that after applying our corrections, we would have a constant amplitude across all geophones. The resulting curves show a much flatter trend than their uncorrected parent curves albeit also showing a 'zoning effect'. This 'zoning effect' arises form the variance between the synthetic amplitude and the real data attributes. The most important reason for this discrepancy is that in generating our synthetics we have derived our density values from the sonic log using a general empirical relationship which might not accurately match the densities in our sedimentary column.

Chapter 5

Conclusions

Vertical Seismic Profiles or VSPs are a standard operation in the exploration and extraction of hydrocarbons. Such records contain both the downgoing and upgoing wavefields and they complement surface seismic experiments in providing information about the subsurface. Aside from the kinematic information in the form of velocities and transit times which delineate structure, the amplitudes of the events in seismic experiments can be used to provide information on the contrasts in physical properties. These amplitudes are theoretically related to the lithological properties of the subsurface. For instance, in a surface seismic experiment amplitude variation with offset studies are carried. In such studies interfaces are distinguished by the variance in the reflection amplitude with angle of incidence. Such properties can directly indicate the presence of gaseous or liquid hydrocarbons.

In the case of an offset VSP, changes in the angle of incidence behavior is produced as the receiver is moved up the bore hole. However, to be able to extract useful information out of VSP amplitudes, the various factors contributing to the amplitude of a seismic wavelet need to be known, identified, and isolated. Inverting seismic amplitudes for lithological information is a more complex process than inverting transit times as there are several mechanisms which effect amplitude.

In the day to day commercial processing of VSPs and surface seismic profiles, workers apply an empirical t^n gain function to the traces in order to restore amplitude loss with time. This approach aims at compensating for geometrical spreading of the wavefront (which usually is the major amplitude loss mechanism) in order to form a good image of the deeper subsurface strata. This method of amplitude restoration

is very crude and does not take into account a number of effects which include : the effect of transmission across interfaces, acoustic impedance of the layers in which the geophones are sitting, frequency selective absorption of the propagating wavelet or source directivity and repeatability. With these and other factors affecting the amplitude of the recorded seismic trace, use of an empirical t^n curve is over simplistic. For example, a continuous t^n curve cannot restore the discontinuities seen in the amplitudes due to the transmission and acoustic impedance effects.

As an alternative and more physically sound approach, we propose a model based amplitude correction scheme. An earth model is generated from the well logs which are usually acquired simultaneously with the VSP. For completeness both the compressional and shear speed and the density logs are required. By ray tracing through this model, synthetic traces can then be generated and the amplitudes of expected events calculated. Correction curves can then be derived and applied to the real data. This method has the advantage of being based on well established theoretical concepts and one can thus include as many complexities in the modeling or ray tracing as desired. For instance, the model can be a set of inhomogeneous anisotropic layers separated by curved interfaces. The effects of frequency absorption and source directivity can easily be included. Of course the accuracy of our corrections depends on how truly our model resembles the real earth. The uncertainty increases as we move away from the bore hole and the information contained in the wireline logs and geological sections.

Before attempting to restore VSP amplitudes, the relationship between geology and VSP plots was studied. This was accomplished through a series of illustrative examples of increasing complexity whereby the characteristic features of VSP plots can be examined. Even though all models were composed of parallel homogeneous isotropic flat layers, it was seen how ray path coverage can be inhomogeneous resulting in non linear and discontinuous transit times. Assuming that the geometric, transmission and acoustic impedance effects constitute the three main amplitude influencing mechanisms, amplitude behavior of events was also examined. Aside from the general amplitude decay across the receivers, these examples also illustrate the change in amplitude polarity due to a decrease in acoustic impedance across an interface and the discontinuous behavior of amplitudes across interfaces which define a sharp acoustic

impedance transition. Application of a continuous t^n correction fails to restore the synthetically generated amplitudes to the theoretically expected amplitudes as predicted from the Zoeppritz equations. Future work includes the sophistication of these models as described above.

The next step was to apply our ideas for amplitude restoration to a shallow zero offset VSP acquired in northern Alberta. Since no shear speed or density logs were available, they were estimated from the sonic log using a fixed value of Poisson's ratio and Gardner's relationship respectively. Two models were then generated, one constituting all the layers described by the sonic log and the other made up from an automatically blocked version of the logs. Amplitude correction curves were generated assuming that the major amplitude influences are due to geometrical, transmission and acoustic impedance effects. Transit time curves were also calculated and the good fit with the picked direct arrival time from the real data increases our confidence in the velocity model. Both the complete and blocked log models agree in their velocity characteristics as seen from the transit time and geometrical effect curves. However, the exclusion of many layers in the blocked log model leads to less decay in the transmission effects curve and this discrepancy is substantial. On the other hand it is not clear why the arbitrary 10cm spaced sonic log layers should provide the more appropriate decay curve and this remains for future research.

Since it is not straightforward as to which feature of the seismic wavelet corresponds to the theoretical amplitude, six different attribute measures of the downgoing direct arrival were taken and compared to the synthetic amplitudes. The synthetic derived from the complete log model matches very well the amplitude attributes both in the characteristic features and in the overall trend and decay. One such characteristic feature is the sudden amplitude loss at 160m corresponding to the interface between the oil sands and the high velocity carbonates. Even though the fit is a good one, the restored attribute curves show a "zoning" effect. Most probably this is due to errors in our density values which were estimated from a general empirical relationship and thus might be different from those in our geological strata.

Some future applications and work might include:

1) Generation of synthetics from more complex models to investigate how and to what extent are VSP amplitudes affected by different geological and physical changes.

Application of this method to other data sets and examination of the restored curves. Ideally we would also like to apply correction curves to offset VSPs which contain more lithological information.

2) Application of a similar approach to surface seismic. In today's world where better exploitation of resources is becoming more and more important, correct amplitude processing is finding its place in seismic processing houses. A modeling based correction for surface seismic was presented by Jon Dowton [62] at this years' CSEG convention.

The amplitude restoration scheme developed in this work was based on ray theory. This theory only holds for high enough frequencies such that the wavelengths are smaller than the thickness of the layers used in the model. If this assumption is violated, then our amplitude and velocity estimates will be erroneous. As an example, consider a couple of thinner elastic interbedding layers (of the order of 10m) within a thicker elastic layer. For seismic wavelengths, the composite layer will behave inelastically. When the earth is composed of layers smaller or comparable to seismic wavelengths, effective media theory must be used for proper modeling. However these issues are still the subject of current research.

Bibliography

[1] Ostrander W.J. *Plane-wave reflection coefficients for gas sands at nonnormal angles of incidence.* Geophysics, Vol. 49, No. 10, p1637-1648, 1984.

[2] Cstrander W.J. *Plane Wave reflection coefficients for gas sands at nonnormal angles of incidence.* SEG Expanded Abstracts, 1982

[3] Chiburis E.F. *Analysis of amplitude versus offset to detect gas/oil contacts in the Arabian Gulf.* SEG Expanded Abstracts, p669-670, 1984.

[4] Gassaway G.S. *SAMPLE: Seismic amplitude measurement for primary lithology estimation.* SEG Expanded Abstracts, p610-613, 1983.

[5] Coulombe C.A. *AVO analysis using the VSP* SEG Expanded Abstracts, p1080-1083, 1991.

[6] O' Doherty R.F. and Anstey N.A. *Reflections on amplitudes.* Geophysical Prospecting, Vol. 19, p430-458, 1971.

[7] Allen J.L. and Peddy C.P. *Amplitude Variation with Offset: Gulf Coast Case Studies.* SEG Geophysical Developments Series, Vol. 4, 1993.

[8] Yu G. *Offset amplitude variation and controlled-amplitude processing.* Geophysics, Vol. 50, No. 12, p2697-2708, 1985.

[9] Dey-Sarkar S.K., Svatek S.A. and Crewe O.W. *Prestack Analysis: Data Processing.* SEG Expanded Abstracts, p339-341, 1986.

[10] Shu-Schung Lee M., Ho S. and Purnell G.W. *Preprocessing for Amplitude-Vs-Angle (AVA) analysis of land seismic data.* SEG Expanded Abstracts, p1070-1071, 1991.

[11] Newman P. *Divergence effects in a layered earth.* Geophysics, Vol. 38, No. 3, p481-488, 1973.

[12] Fazzari F. *Dip-dependent divergence corection.* SEG Expanded Abstracts, p1275-1278, 1992.

[13] Arntsen B. and Sollid A. *Dip-dependent spreading correction through prestack migration/inversion.* SEG Expanded Abstracts, p688-691, 1994.

[14] Wang D.Y. and McCowan D.W. *Spherical divergence correction for seismic reflection data using slant stacks.* Geophysics, Vol. 54, No 5, p563-569, 1989.

[15] Schleicher J., Hubral P. and Tygel M. *Geometrical - Spreading correction by a dual diffraction stack.* Geophysics, Vol. 59, No 12, p1870-1873, 1993.

[16] Tooley R.D., Spencer T.W. and Sagoci H.F. *Reflection and transmission of plane compressional waves.* Geophysics, Vol. 30, No. 4, 1965.

[17] V. de la Cruz and T.J.T. Spanos. *Thermomechanical coupling during seismic wave propagation in a porous medium.* J. Geophys. Research, Vol. 94, p637-642, 1989a.

[18] de la Cruz V. and Spanos T.J.T. *Seismic boundary conditions for porous media.* J. Geophys. Research. 94, 3025-3029, 1989b.

[19] de la Cruz V., Hube J. and Spanos T.J.T. *Reflection and transmission of seismic waves at the boundaries of porous media.* Wave Motion, Vol. 16, p323-338, 1992.

[20] Harlan W.S. *Tomographic correction of transmission distortions in reflected seismic amplitudes.* EAEG Expanded Abstracts, 1994.

[21] Gonzales A. and Chambers R. *Compensating seismic amplitude for transmission losses in the overburden.* SEG Expanded Abstracts, 1994.

[22] Shapiro S.A. and Zien H. *Transmission of wavefields through finely layered media : Attenuation, Velocity, Fluctuations.* EAEG, 53rd Meeting, p820-823, 1991.

[23] Schoenberger M. and Levin F.K. *Apparent attenuation due to intrabed multiples.* Geophysics, Vol. 39, No. 3, June 1974.

[24] De Souza J. M. *Transmission of seismic energy through the Brazilian parana basin layered basalt stack.* SEG Expanded Abstracts, 1982.

[25] Fowler C.M.R. *The Solid Earth. An introduction to global geophysics.* 1990.

[26] Coulombe C.A. and Bird D.N. *Transmission filtering by high amplitude reflection coefficients: theory, practice, and processing considerations.* The Leading Edge, p1037-1042, 1996.

[27] Mendel J.M. *Simultaneous correction for divergence and deconvolution without changing industrial practice.* Geophysics, Vol. 49, No 5 p584-585, 1984.

[28] Lamb H. *The mathematical theory of elasticity.* Cambridge University Press, Cambridge, 1934.

[29] Hron F.*Lecture Notes.* 1996.

[30] Aki K. and Richards P.G. *Quantiative seismology - theory and methods I.* 1980.

[31] Johnston D.H. and Toksoz M.N. *Seismic Wave Attenuation.* SEG, 1981.

[32] Waters K.H. *Reflection Seismology - A Tool for Energy Resource Exploration.* John Wiley and Sons Inc., 1978.

[33] Miller G.F. and Pursey H. *The field and radiation impedance of mechanical radiators on the free surface of a semi-infinite isotropic solid.* Proceedings of the Royal Society, A, Vol. 223, p521.

[34] Clay C.S. *Elementary Exploration Seismology.* Prentice Hall, 1990

[35] Gel'chinsky B.Y. *Expression for the spreading function. In: Problems in the dynamic theory of seismic wave propagation.(G.I. Petrashen Editor.)* Leningrad Univ. Press., Vol.5, p47-53, 1961.

[36] Gal'perin E.I. *Vertical Seismic Profiling.* Society of Exploration Geophysicists, 1994.

[37] Hardage B.A. *Vertical Seismic Profiling - Part A Principles.* Geophysical Press, 1983.

[38] Clay C.S. *Elementary exploration seismology.* Prentice-Hall Inc., 1989.

[39] Kanasewich E.R. *Time sequence analyis in geophysics.* The University of Alberta Press, 1975.

[40] Hatton L., Worthington M.H., Makin J. *Seismic Data Processing - Theory and Practice.* Blackwell Scientific Publications, 1986.

[41] Suprajitno, M. and Greenhalgh, S.A. *Separation of upgoing and downgoing wave in vertical-seismic-profiling by contour slice filtering.* Geophysics, 50, No. 6, 950-962, 1985.

[42] Seeman, B. and Horowicz, L. *Vertical-seismic-profiling - Separation of upgoing and downgoing waves in a stratified medium.* Geophysics, Vol. 48, No. 5, p555-568, 1983.

[43] Yilmaz, O. *Seismic Data Processing.* Society of Exploration Geophysicists, 1988.

[44] Aminzadeh F. *A recursive method for the separation of upgoing and downgoing waves of vertical seismic profiling data.* Geophysics, Vol. 51, No. 12, p2206-2218, 1986.

[45] Gal'perin, E.I. and Frolova, A.V. *Three component seismic observations in boreholes. Parts 1 and 2.* Bull. Acad. Sci. USSR, Geophys. Ser., English Translation, p.519-528, and p.644-653.

[46] Gal'perin, E.I and Frolova, A.V. *Three component seismic observations in boreholes. 1, Vertical Seismic Profiling.* Izv. Geophys. Ser., p793-809.

[47] Gal'perin, E.I. *Polarization method of seismic prospecting.* Moscow, Nedra, Translated by the Ralph McElroy Co.

[48] DiSiena J.P., Gaiser J.E. and Corrigan D.D. *Three component vertical seismic profiles: Orientation of horizontal components for shear wave analysis.* 51st Annual SEG Meeting, 1981.

[49] Esmersoy, C. *Polarization analysis, rotation and velocity estimation in three component VSP in Vertical Seismic Profiling, Part B:Advanced Concepts; Toksoz M.N. and Stewart R.R eds.* Geophysical Press, London, 1984.

[50] Tsai C.J. *Use of autoconvolution to suppress first-order, long-period multiples.* Geophysics, Vol. 50, No. 9, p1410-1425.

[51] Molyneux J.B., Jones M.J., Schmitt D.R. *Identification of multiples contaminating surface seismic data using a VSP analysis technique.* Presented at the SEG Annual Meeting, 1996.

[52] Schoenberger M. and Levin F.K. *Apparent attenuation due to intrabed multiples II.* Geophysics, Vol. 43, No. 4, p730-737, 1978.

[53] Chalaturnyk R.J. *Geomechanics of the Steam Assisted Gravity Drainage Process in Heavy Oil Reservoirs.* Ph.D Thesis, University Of Alberta, 1996.

[54] Schmitt D.R. *Attribute Seismics for Monitoring of a Shallow Heated Heavy Oil Reservoir : A Case Study.* Geophysics, August 1997.

[55] Wrightman D., Rottenfusser B., Kramers J., and Harrison R. *Geology of the Alberta oil sands deposits.* in Hepler L.G. and Hsi C. Eds., AOSTRA Technical Handbook on Oil Sands, Bitumens and Heavy Oils, AOSTRA Technical Publication Ser. 6, 3-9.

[56] Wrightman D.M., Attalla M.N., Wynne D.A., Strobl R.S., Berhane H., Cotterill D.K. and Berezniuk T. *Resource characterization of the McMurray/gas sand deposit in the Athabasca oil sands area.* A synthesis, AOSTRA technical publication Series 10, Alberta Energy, 1995.

[57] Gardner G.H.F., Gardner L.W. and Gregory A.R. *Formation velocity and density - the diagnostic basics for stratigraphic traps.* Geophysics, Vol. 39, No. 6, December 1974.

[58] Chouinard P.N. and Paulson K.V. *A Markov-Gauss Algorithm for blocking well logs.* Geophysics, Vol.53, No. 8, p1118-1121, 1988.

[59] Castagna J.P, Batzle M.L. and Eastwood R.L. *Relationship between compressional wave and shear wave velocities in clastic silicate rocks.* Geophysics, Vol. 50, No. 4, p571-581, 1985.

[60] Taner M.T., Koehler F. and Sheriff R.E. *Applied Geophysics.* Cambridge University Press, Cambridge, 1976.

[61] Molyneux J.B. and Schmitt D.R. *First break timing : arrival onset times by direct correlation.* Submitted to Geophysics, March 1988.

[62] Dowton J. *Getting the benefits of AVO inversion.* CSEG expanded abstracts, 1998.

Appendix A

Model for the UTF site

Layer No.	Depth m	P Wave Velocity ms^{-1}	S Wave Velocity ms^{-1}	Density kg/m^3
	0			
1		1265	683	1372
	30.5			
2		1822	985	2020
	38.1			
3		1871	1012	2030
	53.5			
4		1994	1078	2070
	59.9			
5		1957	1058	2060
	65.5			
6		1946	1052	2050
	72.9			
7		2377	1285	2150
	87.6			
8		2096	1133	2090
	98			
9		2211	1195	2120
	107			
10		2086	1128	2090
	115			

Layer No.	Depth m	P Wave Velocity ms^{-1}	S Wave Velocity ms^{-1}	Density kg/m^3
11		1857	1004	2030
	123			
12		2297	1241	2140
	129			
13		2532	1369	2190
	136			
14		2471	1336	2180
	142			
15		2384	1289	2160
	147			
16		2472	1336	2180
	153			
17		2384	1289	2160
	159			
18		3861	2087	2440
	166			
19		3924	2121	2440
	171			
20		5168	2794	2620
	178			
21		4367	2361	2510
	189			
22		3428	1853	2370
	202			
23		3192	1726	2330
	208			
24		2962	1601	2280
	214			
25		3884	2099	2440
	219			
26		4611	2492	2550
	227			
27		3828	2069	2430
	300			

Table A.1: Geological Model for UTF site

Appendix B

The Ray Tracing Program

B.1 MASTER.M

```
%  This is a ray tracing program for a set of parallel homogeneous
%  interfaces.
%
%  Both Primaries and Reflections seem to be O.K when compared to
%  hand drawn models that are to scale.
%
%  THIS PROGRAM CALLS THE FOLLOWING PROGRAMS :
%  PRIM.M - CALCULATES THE TRANSIT TIMES AND THE GEOMETRICAL EFFECT
%           COEFFICIENTS FOR THE DIRECT ARRIVAL
% REFLECT.M - CALCULATES THE TRANSIT TIMES FOR THE REFLECTED EVENTS
%             FOR THE SPECIFIED HORIZONS
% DGRM.M - PLOTS THE MODEL, SOURCE AND RECEIVERS
%
%
clear;
close all;
%
so = 10;              % SOURCE OFFSET
nr = 77;              % NUMBER OF RECEIVERS
rs = -2.5;            % RECEIVER SEPARATION
fr = 220;             % FIRST RECEIVER
nl = 1972;              % NUMBER OF LAYERS
%lay =  [ ];     % LAYER PARAMETERS ( P VEL, S VEL, DEN )
layer
%dep = [ ];      % INTERFACE DEPTHS
trant = zeros(nr,1);
teta = zeros(1,nl);
tetpr= zeros(1,nl);
patu = zeros(nr,1);
nrf = 8;
refl = 8;               % LAYER NUMBER WHERE HORIZON OF INTEREST
%                         IS THE LOWER BOUNDARY
geft = zeros(nrf+1,nr);
patl = zeros(nr,refl);
pcor = zeros(refl*2,2);
ptrs = zeros(1,nr);
```

```
tran = zeros(nrf+1,nr);
avom = zeros(nrf,nr);
decay = ones(nrf+1,nr);
%
% CALCULATING RECEIVER POSITIONS AND LAYER THICKNESS
%
rec(nr) = fr;
for i=1:nr-1
 rec(nr-i) = rec(nr-i+1) + rs;
end
for i=1:nl
 thik(i) = (dep(i+1) - dep(i));
end
%
% OPENING THE GRAPHICS WINDOW
%
dgrm
pause
%
% FINDING TRANSIT TIMES FOR THE PRIMARY EVENT
%
prim
%
 figure
 plot(rec,trant)
 title('Direct Arrival Transit Time')
 xlabel('Geophone Depth (m)','Fontsize',[18])
 ylabel('Transit time','Fontsize',[18])
 set(gca,'linewidth',[2],'Fontsize',[18])
 figure
 plot(rec,geft(1,:),'+','markersize',[10])
 title('Geometrical Effect Coefficients')
 xlabel('Geophone Depth (m)','Fontsize',[18])
 ylabel('Normalized Geometrical Coefficients','Fontsize',[18])
 set(gca,'linewidth',[2],'Fontsize',[18])
 for idc=1:nr
  decay(1,idc)=decay(1,idc)*geft(1,idc);
 end
 figure
 plot(rec,tran(1,:),'+','markersize',[10])
 title('Transmission Coefficients')
 xlabel('Geophone Depth (m)','Fontsize',[18])
 ylabel('Normalized Transmission Coefficient','Fontsize',[18])
 set(gca,'linewidth',[2],'Fontsize',[18])
 for idc=1:nr
  decay(1,idc)=decay(1,idc)*tran(1,idc);
 end
 figure
 plot(rec(1:nr),decay(1,1:nr),'c')
 title('GS and Transmission effects combined')
 xlabel('Geophone Depth (m)','Fontsize',[18])
 ylabel('Normalized Amplitude','Fontsize',[18])
 set(gca,'linewidth',[2],'Fontsize',[18])
%
% GENERATING A SYNTHETIC VSP FROM THE CALCULATED TRANSIT TIMES
```

```
%
 nsam = 500;
 samp = 0.001;
 data = zeros(nsam,nr);
 for i=1:nr
  j = 0;
  indx=0;
  while j < trant(i)
   indx = indx + 1;
   j = j + samp;
  end
  data(indx,i) = decay(1,i);
 end
pause
%
% FINDING TRANSIT TIMES FOR THE REFLECTED EVENTS
%
for imk=1:nrf
 figure(1);
 reflect
%
 figure(2)
 hold on
 plot(rec(1:nmrc),trant(1:nmrc))
 hold off
%
 figure(3)
 hold on
 plot(rec(1:nmrc),geft(nrf-imk+2,1:nmrc),'+')
 hold off
 for idc=1:nmrc
  decay(nrf-imk+2,idc)=decay(nrf-imk+2,idc)*geft(nrf-imk+2,idc);
 end
%
 figure(6)
 hold on
 plot(rec(1:nmrc),tran(nrf-imk+2,1:nmrc),'+','markersize',[8])
 title('Transmission Coefficients for reflected events')
 xlabel('Geophone Depth (m)','Fontsize',[18])
 ylabel('Normalized Transmission Coefficients','Fontsize',[18])
 set(gca,'linewidth',[2],'Fontsize',[18])
 hold off
 for idc=1:nmrc
  decay(nrf-imk+2,idc)=decay(nrf-imk+2,idc)*tran(nrf-imk+2,idc);
 end
%
 figure(5);
 hold on
 nfac = max(abs(decay(nrf-imk+2,:)));
 decay(nrf-imk+2,:) = decay(nrf-imk+2,:)./nfac;
 plot(rec(1:nmrc),decay(nrf-imk+2,1:nmrc),'c')
 hold off
%
 figure(7);
 hold on
```

```
 plot(rec(1:nmrc),avom(nrf-imk+1,1:nmrc),'+r','markersize',[8])
 title('Amplitude Coefficient')
 xlabel('Geophone Depth (m)','Fontsize',[18])
 ylabel('P Wave Amplitude','Fontsize',[18])
 set(gca,'linewidth',[2],'Fontsize',[18])
 hold off
%
% ADDING THE REFLECTED EVENT TO THE SYNTHETIC VSP
%
 for i=1:nmrc
  j = 0;
  indx=0;
  while j < trant(i)
   indx = indx + 1;
   j = j + samp;
  end
  data(indx,i) = decay(nrf-imk+2,i);
 end
 refl=refl-1;
end
 figure;
 wigb(data)
```

B.2 DGRM.M

```
%
% Plotting a diagram of the ray tracing
%
rear = zeros(nr,2);
xmin = -10;
xmax = so+10;
ymin = dep(1) -10;
ymax = dep(nl+1)+10;
xln = xmin:10:xmax;
pts = size(xln);
% Generating the layers
for i=1:nl+1
 y(i,1:pts(2)) = dep(i) * ones(pts);
end
figure;
plot(xln,y,'k-','markersize',[2])
axis([xmin,xmax,ymin,ymax]);
axis ij;
%title('RAY TRACING THROUGH MODEL')
xlabel('OFFSET DISTANCE (m)','Fontsize',[18])
ylabel('GEOPHONE DEPTH (m)','Fontsize',[18])
set(gca,'linewidth',[2],'Fontsize',[18])
hold on;
plot(so,0,'ok')
rear(:,[2]) = rec';
plot(rear(:,1),rear(:,2),'r*')
```

B.3 PRIM.M

```
%
% THIS PROGRAM IS CALLED BY MASTER.M AND FINDS THE TRANSIT TIMES
% FOR THE PRIMARY EVENT. IT ALSO PLOTS THE RAYPATHS AND CALCULATES
% THE GEOMETRICAL EFFECT COEFFICIENTS FOR EACH RECEIVER.
%
 teta(1)=pi/180;
 idir = 1;
 incf=1800;
 msum = 0;
 while so > msum                    %SETTING CONVERGENCE CRITERION
  teta(1) = teta(1) + idir*(pi/incf);
  xpos(1)= thik(1)*tan(teta(1));
  msum = xpos(1);
  for ii=2:nl
   teta(ii)=asin((lay(ii,1)/lay(ii-1,1))*sin(teta(ii-1)));
   xpos(ii)=thik(ii)*tan(teta(ii));
   msum = msum + xpos(ii);
  end
 end
 teta(1) = teta(1) - idir*(pi/incf);
 incf = incf*10;
 fail = 0;
% INITIATING ITERATION FOR EACH RECEIVER
 for i=1:nr
  ibn=0;
  curr = rec(nr-i+1);               % CURRENT RECEIVER POSITION
  for j=nl:-1:1                     % CURRENT LAYER
   if curr < dep(j+1)
    curl = j;
   elseif curr == dep(j+1)
    curl = j;
    ibn = 1;
   end
  end
  conv = abs(rs);
  if fail == 1                      % SETTING SAFETY FACTORS
   idir = idir * -1;
   incf = incf/10;
   fail = 0;
  end
  while conv > abs(rs)/1000     %SETTING CONVERGENCE CRITERION
   teta(1) = teta(1) + idir*(pi/incf);
   xpos(1)= thik(1)*tan(teta(1));
   msum = xpos(1);
   for ii=2:curl
    teta(ii)=asin((lay(ii,1)/lay(ii-1,1))*sin(teta(ii-1)));
    xpos(ii)=thik(ii)*tan(teta(ii));
    msum = msum + xpos(ii);
   end
   if (so < msum) | (ibn == 1)
    dif = msum - so;
    hgt = dif/tan(teta(curl));
    yloc = dep(curl+1)-hgt;
```

```
    temp = yloc-curr;
    if (temp < 0) & (fail == 0)
     incf = incf*10;
     idir = idir*(-1);
     fail=1;
    end
    conv = abs(temp);
    if (fail == 1) & (temp < 0)
     tcvf=teta;
    elseif (fail == 1) & (temp > 0)
     teta=tcvf;
     conv=0;
     for ii =1:curl
      xpos(ii)=thik(ii)*tan(teta(ii));
     end
    end
   end
  end
  for k=1:curl-1
   patl(nr-i+1,k) = sqrt(xpos(k)*xpos(k) + thik(k)*thik(k));
  end
  patl(nr-i+1,curl) = (thik(curl)-hgt)/cos(teta(curl));
%
% CALCULATING THE AMPLITUDE LOSS ON TRANSMISSION
%
  sec = 1;
  irep=curl-1;
  refla(:,:)=1;
  for ilo=1:irep
   amps;
  end
  tran(1,nr-i+1) = 1;
  for ivl=1:irep
   tran(1,nr-i+1) = tran(1,nr-i+1)*refla(3,ivl);
  end
%
% CALCULATING AND PLOTTING THE RAYS
%
  pcor(1,:)=[so,0];
  for im=2:curl
   pcor(im,1)=pcor(im-1,1)-xpos(im-1);
   pcor(im,2)=dep(im);
  end
  pcor(curl+1,:)=[0,yloc];
%  plot(pcor(1:curl+1,1),pcor(1:curl+1,2),'-g')
  clear xpos
%
% CONVERTING PATH LENGTHS TO TRANSIT TIME
%
  trant(nr-i+1)=0;
  for j=1:curl
   trant(nr-i+1) = trant(nr-i+1) + (patl(nr-i+1,j)/lay(j,1));
  end
%
% CALCULATING THE GEOMETRICAL EFFECTS COEFFICIENTS FOR
```

```
% THE CURRENT RECEIVER.
%
  gpll=0;
  gpcr=0;
  for jk=2:curl
   cterm = cos(teta(1))*cos(teta(1))/(cos(teta(jk))*cos(teta(jk)));
   gpcr = gpcr +  patl(nr-i+1,jk) * (lay(jk,1)/lay(1,1));
   gpll = gpll + cterm * patl(nr-i+1,jk) * (lay(jk,1)/lay(1,1));
  end
  gpcr=gpcr + patl(nr-i+1,1);
  gpll=gpll + patl(nr-i+1,1);
  geft(1,nr-i+1) = 1/sqrt(gpll*gpcr);
 end
% Normalizing the geometrical coefficients
nfac=max(geft(1,:));
geft(1,:)=geft(1,:)./nfac;
```

B.4 REFLECT.M

```
%
% THIS PROGRAM IS CALLED BY MASTER.M AND CALCULATES THE
% TRANSIT TIMES FOR A SERIES OF REFLECTORS.
%
pcor(1,:)=[so,0];
teta(1)=pi/180;
idir = 1;
incf=1800;
msum = 0;
while so > msum                    %SETTING CONVERGENCE CRITERION
 teta(1) = teta(1) + idir*(pi/incf);
 xpos(1)= thik(1)*tan(teta(1));
 msum = xpos(1);
 for ii=2:refl
  teta(ii)=asin((lay(ii,1)/lay(ii-1,1))*sin(teta(ii-1)));
  xpos(ii)=thik(ii)*tan(teta(ii));
  msum = msum + xpos(ii);
 end
end
incf = incf*10;
idir = idir*(-1);
fail = 0;
nmrc = 0;
for i=1:nr
 curr = rec(nr-i+1);               % CURRENT RECEIVER POSITION
 for j=nl:-1:1                     % CURRENT LAYER
  if curr < dep(j+1)
   curl = j;
  end
 end
 if curr < dep(refl+1)
  nmrc=nmrc+1;
  conv = abs(rs);
  if fail == 1                      % SETTING SAFETY FACTORS
   idir = idir * -1;
   incf = incf/10;
   fail = 0;
  end
  while (conv > abs(rs)/1000)      %SETTING CONVERGENCE CRITERION
   teta(1) = teta(1) + idir*(pi/incf);
   xpos(1)= thik(1)*tan(teta(1));
   msum = xpos(1);
   for ii=2:refl
    teta(ii)=asin((lay(ii,1)/lay(ii-1,1))*sin(teta(ii-1)));
    xpos(ii)=thik(ii)*tan(teta(ii));
    msum = msum + xpos(ii);
   end
   if so > msum
    dif = so - msum;
    hgt = dif/tan(teta(refl));
    if curl < refl
     xcr = 0;
     for ij = 1:(refl-curl)
```

```
      xcr = xcr + thik(refl-ij+1)*tan(teta(refl-ij+1));
     end
     dif = dif - xcr;
     hgt = dif/tan(teta(curl));
    end
    yloc = dep(curl+1) - hgt;
    temp = yloc - curr;
    if (temp < 0) & (fail == 0)
     idir = idir *(-1);
     incf = incf *10;
     fail = 1;
    end
    conv = abs(temp);
    if (fail == 1) & (temp < 0)
     tcvf=teta;
    elseif (fail == 1) & (temp > 0)
     teta=tcvf;
     conv=0;
     for ii = 1:refl
      xpos(ii)=thik(ii)*tan(teta(ii));
     end
    end
   end
  end
%
% CALCULATING THE PATH LENGTHS OF THE RAYS AND PLOTTING THE RAYS
%
  for k = 1:refl
   patl(nr-i+1,k) = sqrt(xpos(k)*xpos(k) + thik(k)*thik(k));
   pcor(k+1,:)=[pcor(k,1)-xpos(k),dep(k+1)];
  end
  if curl < refl
  for ik = 1:(refl-curl)
    patl(nr-i+1,refl-ik+1) = patl(nr-i+1,refl-ik+1)*2;
    pcor(refl+1+ik,:)=[pcor(refl+ik,1)-xpos(refl+1-ik),
                                          dep(refl+1-ik)];
   end
  end
  patu(nr-i+1) = sqrt(hgt*hgt + dif*dif);
  ise=abs(refl-curl);
  pcor(refl+ise+2,:)=[0,yloc];
  plot(pcor(1:refl+ise+2,1),pcor(1:refl+ise+2,2),'-g')
  ptrs(1,nr-i+1)=teta(refl);
  clear xpos
% CONVERTING PATH LENGTHS TO TRANSIT TIME
  trant(nr-i+1) = 0;
  for j=1:refl
   trant(nr-i+1) = trant(nr-i+1) + (patl(nr-i+1,j)/lay(j,1));
  end
  trant(nr-i+1) = trant(nr-i+1) +  patu(nr-i+1)/lay(curl,1);
%
% CALCULATING THE AMPLITUDE LOSS ON TRANSMISSION AND REFLECTION
% TO THE CURRENT RECEIVER
%
  sec = 1;
```

```
   irep=refl-1;
   refla(:,:)=1;
   tran(nrf-imk+2,nr-i+1) = 1;
   for ilo=1:irep
    amps
    tran(nrf-imk+2,nr-i+1) = tran(nrf-imk+2,nr-i+1)*refla(3,ilo);
   end
   ilo=refl;
   amps
   tran(nrf-imk+2,nr-i+1) = tran(nrf-imk+2,nr-i+1) * refla(1,ilo);
   avom(nrf-imk+1,nr-i+1) = refla(1,ilo);
   if curl < refl
    sec = -1;
    for ilo=refl:-1:curl+1
     amps
     tran(nrf-imk+2,nr-i+1) = tran(nrf-imk+2,nr-i+1)*refla(3,ilo);
    end
   end
%
% CALCULATING THE GEOMETRICAL EFFECT COEFFICIENTS FOR THE CURRENT
% RECEIVER.
%
  gpll=0;
  gpcr=0;
  for jk=2:refl
   cterm = cos(teta(1))*cos(teta(1))/(cos(teta(jk))*cos(teta(jk)));
   gpcr = gpcr +  patl(nr-i+1,jk) * (lay(jk,1)/lay(1,1));
   gpll = gpll + cterm * patl(nr-i+1,jk) * (lay(jk,1)/lay(1,1));
  end
  cterm = cos(teta(1))*cos(teta(1))/(cos(teta(curl))*cos(teta(curl)));
  gpcr=gpcr + patu(nr-i+1) * lay(curl,1)/lay(1,1) + patl(nr-i+1,1);
  gpll=gpll + cterm * patu(nr-i+1)*lay(curl,1)/lay(1,1)
                                                + patl(nr-i+1,1);
  geft(nrf-imk+2,nr-i+1) = 1/sqrt(gpll*gpcr);
 end
end
%
% Normalizing the transmission effect coefficients
 nfac=max(abs(tran(nrf-imk+2,:)));
 tran(nrf-imk+2,:)=tran(nrf-imk+2,:)./nfac;
% Normalizing the geometrical effect coefficients
 nfac=max(abs(geft(nrf-imk+2,:)));
 geft(nrf-imk+2,:)=geft(nrf-imk+2,:)./nfac;
% Normalizing the AVO coefficients
 nfac=max(abs(avom(nrf-imk+1,:)));
 avom(nrf-imk+1,:)=avom(nrf-imk+1,:)./nfac;
```